TWO COUPLED OSCILLATOR MODELS:

THE MILLENNIUM BRIDGE AND THE CHIMERA STATE

A Dissertation

Presented to the Faculty of the Graduate School

of Cornell University

in Partial Fulfillment of the Requirements for the Degree of

Doctor of Philosophy

by

Daniel Michael Abrams

August 2006

TWO COUPLED OSCILLATOR MODELS:

THE MILLENNIUM BRIDGE AND THE CHIMERA STATE

Daniel Michael Abrams, Ph.D.

Cornell University 2006

Ensembles of coupled oscillators have been seen to produce remarkable and unexpected phenomena in a wide variety of applications. Here we present two mathematical models of such oscillators. The first model is applied to the case of London's Millennium Bridge, which underwent unexpected lateral vibration due to pedestrian synchronization on opening day in 2000. The second model analyzes a new mode of collective behavior observed for a ring of nonlocally coupled phase oscillators.

BIOGRAPHICAL SKETCH

Danny Abrams grew up in Houston, Texas. He attended Bellaire High School and the California Institute of Technology, where he graduated with a Bachelor of Science in Applied Physics. He has many hobbies—e.g., basketball, squash, foreign languages— but his favorite is still science.

Dedicated to those who had no opportunity for a quality education.

ACKNOWLEDGEMENTS

"If you wish your merit to be known, acknowledge that of other people."

—Oriental Proverb

This dissertation would not have been possible without an incredible amount of help and support by many people in my life.

My advisor, Steve Strogatz, has been an amazing mentor. He's made my time at Cornell really enjoyable, giving me great advice and guidance, and always coming up with interesting projects to work on. Sometimes I think I should have delayed graduating to keep our collaboration going for longer!

Richard Rand, a member of my special committee, gave useful feedback at both A and B exams, and taught me a lot about perturbation theory in his courses in TAM.

My other special committee member, David Hysell, did a great job with feedback at both A and B exams. I wish I had the opportunity to get to know more about his research.

Richard Wiener was a good friend and mentor to me during my first years at Cornell. His enthusiasm is contagious, and our new collaboration should soon bear fruit.

My longtime house-mate Marc Favata contributed to both my research and my quality of life through long conversations about science and everything else. He's been a great friend, and it will be hard getting used to life without him next year.

All of my other friends and housemates from Caltech's Ruddock House—Zach Medin, Ryan Gutenkunst, David Fang, and Chris Liu—have been great pals over the past several years, and I'd like to thank them for that.

My officemate David Yoon provided help with math and some great conversations. Tuncay Alan, Cedric Langbort, Tuhin Sahai, and many others in the TAM department made my Cornell experience a really terrific one.

Of course, I owe an immeasurable amount to my family. My parents gave me a great start in life, including an excellent education (both at home and at school), and exposed me to numerous interesting activities when I was young. My older brother David helped with more than hand-me-down clothes, providing a superb role model and a free tutor, besides a partner for one-on-one basketball. My younger sister Susan was a great counterpoint, a source of interesting ideas and someone who would always listen to my crazy theories.

One final thanks to the US National Science Foundation, who have provided financial support through fellowships during the past five years, and amazingly will now fund my postdoctoral work during the coming three years. If their budget (about \$5 billion) were even 10% of the defense budget (about \$500 billion), it would be a much better world.

TABLE OF CONTENTS

LIST OF TABLES

LIST OF FIGURES

LIST OF ABBREVIATIONS

- CAM = Center for Applied Math

- CL1 = Fundamental Lateral mode on the Center span

- CL2 = First harmonic (2nd lateral mode) on the Center span

- NL1 = Fundamental Lateral mode on the North span

- SL1 = Fundamental Lateral mode on the South span

- TAM = Theoretical and Applied Mechanics

LIST OF SYMBOLS

- X = Bridge lateral displacement $[m]$

- A = Bridge lateral oscillation amplitude $[m]$

- M = Bridge modal mass for a given span $[kg]$

- m_{ped} = Mass of a single average pedestrian $[kg]$

- K = Bridge modal spring constant for a given span $[kg/s^2]$

- B = Bridge modal damping for a given span $[kg/s]$

- C = Pedestrian sensitivity to lateral bridge motion $[m^{-1}s^{-1}]$

- Θ_i = Phase of the ith pedestrian in his walking cycle $[rad]$

- Φ = Phase of the oscillating bridge $[rad]$

- $\Omega_0 = \sqrt{K/M}$ = Bridge undamped natural frequency for a given span $[rad/s]$

- $f_0 = \Omega_0/(2\pi)$ = Bridge undamped natural frequency for a given span $[Hz]$

- q = Angular frequency of the combined bridge-crowd system $[rad/s]$

- q_0 = Angular frequency of the combined bridge-crowd system at vibration onset$[rad/s]$

- $\zeta = \frac{1}{2}B\Omega_0/K$ = Dimensionless damping ratio

- $\Omega_d = \Omega_0\sqrt{1-\zeta^2}$ = Bridge damped natural frequency for a given span $[rad/s]$

- $f_d = \Omega_d/(2\pi)$ = Bridge damped natural frequency for a given span $[Hz]$

- Ω_i = Natural frequency of lateral forcing for the ith walker $[rad/s]$

- N = Number of walkers on a given span of the bridge

- $L_1 = NG/K$ = Bridge displacement if full pedestrian load were applied statically (see 4.4) $[m]$

- $L_2 = \Omega_0/C$ = Bridge oscillation amplitude necessary for a unit change in pedestrian angular frequency (see 4.4) $[m]$

- $L = \sqrt{L_1 L_2}$ = Scaling length used for nondimensionalization (see 4.4) $[m]$

- $\epsilon = \sqrt{L_1/L_2}$ = Dimensionless small parameter used for perturbation theory

- t = Time $[s]$

- $\tau = \Omega_0 t =$ Dimensionless time

- $T = \epsilon\tau = \epsilon\Omega_0 t =$ Slow time

- $x = X/L =$ Dimensionless bridge displacement

- $a = A/L =$ Dimensionless bridge oscillation amplitude

- $b = \epsilon^{-1}\zeta = \mathcal{O}(1)$ perturbative damping

- $\omega_i = \epsilon^{-1}(\Omega_i/\Omega_0 - 1) = \mathcal{O}(1)$ pedestrian detunings

- $\bar{\omega} = 1/N \sum \omega_i =$ Mean pedestrian detuning

- $\theta_i = \Theta_i - \Omega_0 t =$ Phase of the ith pedestrian in a frame rotating at Ω_0 $[rad]$

- $\psi = \Psi - \Omega_0 t =$ Phase of the oscillating bridge in a frame rotating at Ω_0 $[rad]$

- $q =$ Frequency of combined bridge-crowd system at the partially-locked or in-phase equilibrium

- $\phi_i = \theta_i - qt =$ The phase of the ith pedestrian in a frame co-rotating with the bridge-crowd system at equilibrium

- $W =$ Width of distribution in numerical code (see Chapter 6)

- $R = |\langle\exp(i\theta_i)\rangle| =$ Order parameter magnitude

- $\Phi = \arg\langle\exp(i\theta_i)\rangle =$ Order parameter angle

- $\mathcal{R} =$ Level of additive noise used in determining initial conditions for numerical simulations

- $\xi_i =$ A uniform random variable on $[0,1)$.

PREFACE

Oscillatory systems surround us. The motors in our cars, the daily temperature variation, the annoying din of the air conditioner—even the cells of our bodies undergo regular periodic oscillation.

Freshman physics students are taught all about the simple harmonic oscillator. They learn the concept of steady-state motion, the effects of damping and forcing, and they may solve homework problems on some of the ubiquitous real-world oscillators. In advanced courses, physics students sometimes learn about nonlinear effects such as amplitude dependent spring softening or hardening, and nonlinear oscillators like those of Duffing or Van der Pol.

Unfortunately, the topic of oscillation rarely progresses beyond its discovery or observation. It's as though having learned the law of universal gravitation, we might be asked to calculate the attraction of two bodies, but somehow we would completely ignore the rich implications for orbital mechanics. Oscillators are everywhere. Knowledge of simple and nonlinear limit-cycle systems is just the beginning for an understanding of what can happen in the real world, where unending mechanical, electromagnetic, and biological vibrations interact over 30 orders of magnitude in space and time.

In this dissertation I will investigate two systems, each composed of weakly-coupled limit cycle oscillators. One may be considered a generic model for nonlocal coupling, while the other simulates crowd behavior on a bridge. In both cases, extremely modest assumptions lead to rich and complex, but still theoretically tractable behavior.

A system can be more than the sum of its parts. Understanding the complex ways that oscillators interact is vital to understanding more of our world.

CHAPTER 1

INTRODUCTION

"Every writer creates his own precursors. His work modifies our conception of the past, as it will modify the future."

—Jorge Luis Borges

This dissertation focuses on two different coupled-oscillator models that I investigated during the course of my time at Cornell University. Because the second model comprises the bulk of my dissertation, I will present it first (Chapters 2–6). However, in chronological terms, this was not the first model that I studied.

Chronologically, the first model that I studied, in collaboration with Steve Strogatz, was a one-dimensional system of nonlocally, nonglobally coupled oscillators. This intermediate system was shown to support a unique phenomenon that we dubbed a "chimera state," in which both phase-locked and incoherent oscillators coexist, each occupying some fraction of the system. It was originally detected by Yoshiki Kuramoto of Kyoto University [14], and a later paper describing it [4] piqued my interest during 2003, my third year at Cornell. Our work on this phenomenon has been published in [1] and [2], and is discussed in Chapter 7.

The other phenomenon discussed in this dissertation is much more physically intuitive, yet was more difficult to model. As described in Chapter 2, the Millennium Bridge in London, England unexpectedly began to vibrate laterally on opening day in June 2000, and had to be closed two days later. Video footage of the crowd during this oscillation shows remarkable correlation in left-right motion, suggesting that some type of biological synchronization had occurred among the pedestrians. Experiments later showed that the vibration happened only when

the crowd was dense enough—that is, above a critical threshold in the number of walkers. Below that threshold, bridge motion was undetectable, but above that threshold, large amplitude motion spontaneously developed.

The idea of modeling a system of biological oscillators appealed to me, as well as the idea of modeling human behavior, while still remaining grounded in the well-studied field of bridge mechanics. The work in collaboration with Steve Strogatz (my advisor) and Allan McRobie of Cambridge University has thus far resulted in one publication [23], but much remains unpublished. I hope to use this dissertation as a more complete documentation of our efforts to understand this interesting system.

1.1   Navigating this Dissertation

The research described in this volume did not proceed linearly from a problem statement to conclusions and results. There were many dead-ends, side-projects, and relatively interesting but unimportant (and ultimately unpublished) results. For that reason, much of the material presented here will be secondary to the main thrust of the argument.

Most of the material outside of Chapter 4 and Chapter 7 can be skipped or read without particular focus on the order. Within Chapter 4, the reader will be best served by completing the first 9 sections in order before skipping to any other part of the dissertation. Chapter 7 is reprinted from a previous publication, and thus is best read as a single unit.

CHAPTER 2

BACKGROUND ON THE MILLENNIUM BRIDGE

"The hardest thing to learn in life is which bridge to cross and which to burn."

—David Russel

2.1   The Story

"By day the bridge will be an extraordinarily thin 'blade' of stainless steel and cable, whilst at night it will appear as a 'blade of light.'"

—Foster and Partners, Ove Arup and Partners, and Sir Anthony Caro in Millennium Bridge design competition submission

On June 10, 2000, a new footbridge over London's Thames river was opened to the public (see Figure 2.1). Designed by a team including renowned sculptor Sir Anthony Caro and Britain's leading architect, Lord Norman Foster, the Millennium Bridge was built with an extremely shallow profile, intended to resemble "a blade of light." It was constructed during 1998–2000 at a cost of £18.2 million ($29.9 million in January 2000 dollars), including a £2.2 million cost overrun. As an eager crowd streamed onto the bridge for the opening celebration, something went wrong. Within minutes, the bridge developed large amplitude side-to-side oscillations, and the crowd simultaneously began to fall into step. Due to this completely unanticipated motion, city authorities were forced to close the bridge just two days after its inauguration. During the following 18 months, Arup, the engineering firm that built the bridge, spent £5 million to develop a system of passive dampers aimed at controlling the unwanted wobble [20]. Their testing

Figure 2.1: The Millennium Bridge

and modeling led to a partial understanding of the problem, but left several interesting phenomena—including the apparently spontaneous synchronization of the pedestrians—unexplained.

2.2   Bridge Design and Construction

"*Nothing is built on stone; all is built on sand, but we must build as if the sand were stone.*"

—Jorge Luis Borges

The design of the Millennium Bridge was the result of a competition organized in the summer of 1996, with each submission coming from a collaborative team of architects, artists, and engineers. There were 227 entries in the competition, demonstrating the high level of interest in this project. The winning design was chosen in December 1996, and after two and a half years of planning and bureaucratic wrangling, construction on the bridge began in April 1999.

Figure 2.2 shows a computer rendering used in the planning of the Millennium Bridge. Emphasized in successive images are the pile foundations, the north
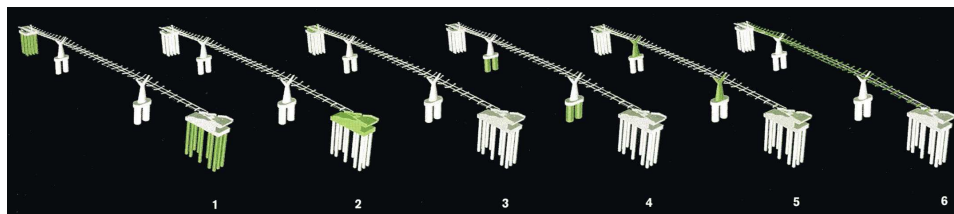
Figure 2.2: Computer-generated renderings emphasizing the various components of the Millennium Bridge (taken from [24]).

abutment, the south "wing" abutment, the caisson foundations, the piers and pier arms, and the transverse arms.

Figure 2.3 shows front, side, and top cross-sectional views of the piers (each supported on two 6-meter diameter caissons), while Figures 2.4 and 2.5 demonstrate the construction of the aluminum deck sections. The deck is about 4 meters wide, made up of a series of 16 meter sections referred to as 'trestles', connected by sliding joints.

Figure 2.6 is a full length top-view schematic diagram of the bridge including all three spans. It demonstrates the positions of the abutments, piers, and cables, as well as the transverse arms (spaced every 8 meters) upon which the deck rests. Figure 2.7 show a close-up view of one 16 meter section of bridge, with the deck removed. This close-up indicates the changes made to stabilize the bridge against unwanted vibrations: viscous and tuned-mass dampers were added together with chevron bracing.

2.3 Controlled Tests

After the bridge was closed, Arup initiated a series of experiments to better determine the number of pedestrians necessary to destabilize a given span of the bridge. Figures 2.8 and 2.9 show the results of tests conducted on the bridge's north span.
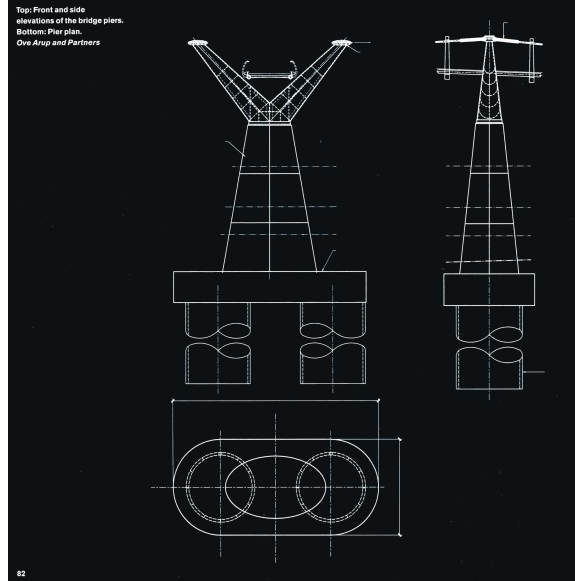
Figure 2.3: Cross sectional schematic of the supports for Millennium Bridge (taken from [24]).

These tests were administered by having Arup employees enter the span in a controlled fashion, so that the size of the crowd was known, while accelerometers recorded the resulting vibrations.

During the course of testing, Arup found several empirical relations that will be discussed later in this dissertation.

2.4 Available Data

The data relevant to opening day is limited to some archival video footage available via the Arup web page[1] at `http://www.arup.com/millenniumbridge/indepth/video.html`. Peak crowd densities can be estimated from the videos and from published Arup statistics at about 1.3–1.5 persons per square meter, or about 450 total walkers on the north span (324 square meters - see 2.2) [6, 10].

---

[1]Videos were available at the time of writing, July 13, 2006. If they later become unavailable please contact the author for copies.
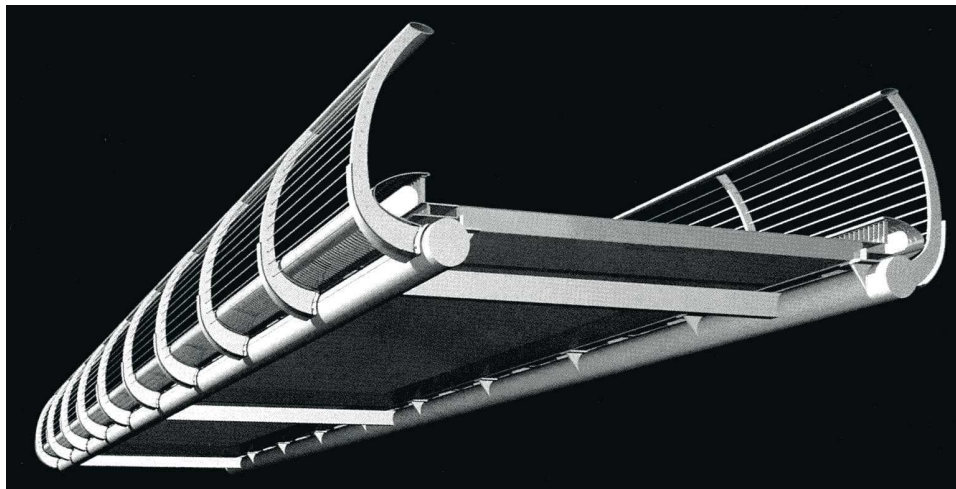
Figure 2.4: Computer rendering of a deck section for the Millennium Bridge (taken from [24]).
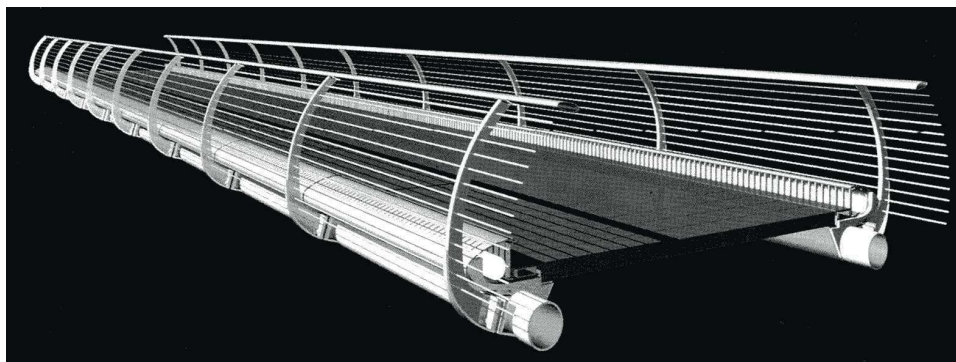
Figure 2.5: Computer rendering of a deck section for the Millennium Bridge (taken from [24]).

However, several papers have been published pertaining to the bridge design, and experiments done on the bridge after it was closed to the public [7, 6, 10]. Thus we can form reasonable guesses about the conditions on opening day.

2.5 Bridge Parameters

Because the majority of published experimental data pertains to the fundamental lateral mode of the north span, we've used those parameters in most of the calculations presented in the following chapters. Table 2.1 (page 10) presents all of the
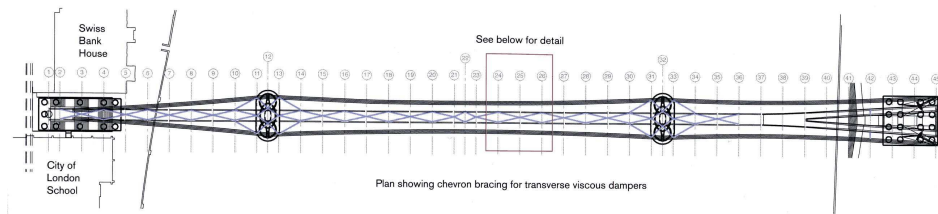
Figure 2.6: Top schematic view of the bracing and dampers for the Millennium Bridge. See also Figure 2.7 (taken from [24]).

Typical plan showing dampers with deck removed
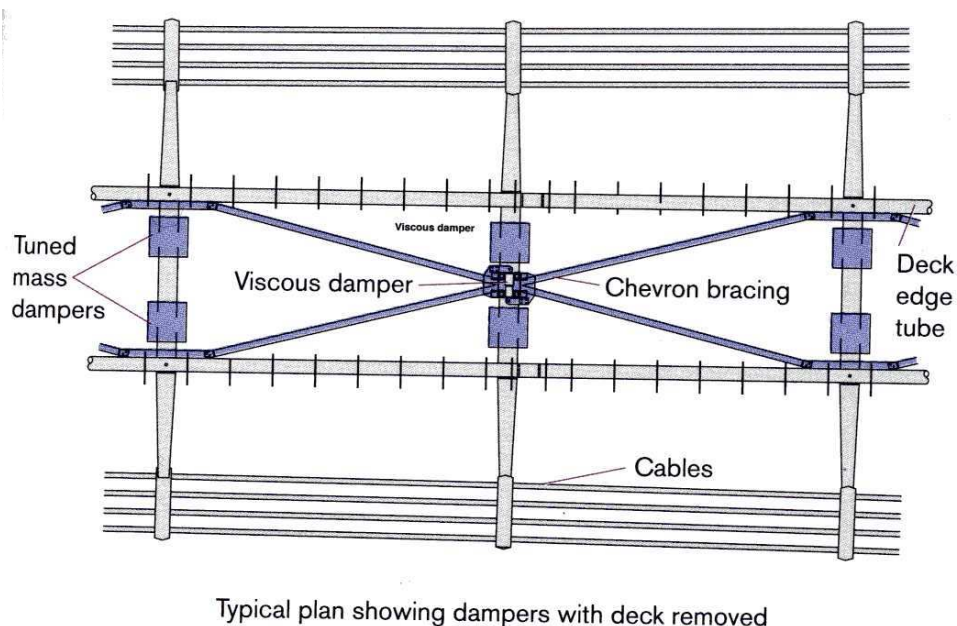
Figure 2.7: Schematic view of placement for dampers and bracing on the Millennium Bridge. See also Figure 2.6 (taken from [24]).

published data for the three spans of the Millennium Bridge.

Since there are ranges of possible values presented in Table 2.1, we must choose some numbers to use for numerical calculations. We follow previous work [7, 16, 19] and take $\zeta = 0.75\%$ when it is not known exactly, and we use the theoretical value $M = 113 \times 10^3 kg$ for the modal mass of the north span. This gives $B = 11.0 \times 10^3 kg/s$ and $K = 4730 \times 10^3 kg/s^2$ for the north span's fundamental mode.

The resonant frequencies of various footbridges are presented for comparison in Figure 2.10 (from [7]).
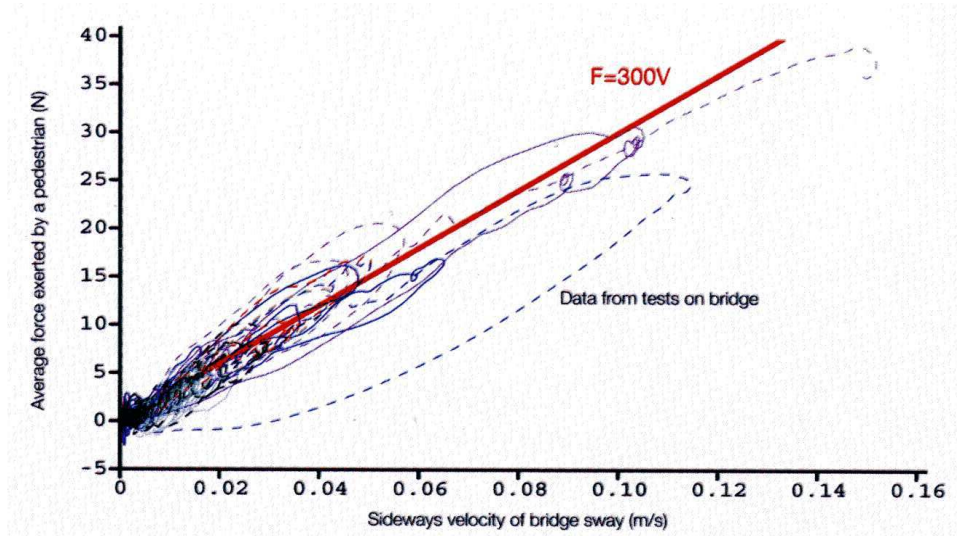
Figure 2.8: Experimental results based on Arup's controlled tests conducted after closure of the Millennium Bridge (taken from [24]). Note the generally linear relationship between force exerted and sideways velocity. See Section 3.2 for a more detailed description of Arup's model.

Some other possibly useful numbers for the north span fundamental mode:

- Undamped natural frequency $\Omega_0 = \sqrt{K/M} = 6.4717$ ($f_0 = 1.03\text{Hz}$).

- Damped natural frequency $\Omega_d = \Omega_0\sqrt{1 - \zeta^2} = 6.4715$ ($f_d = 1.02997\text{Hz}$).

- Quality factor $Q = 2\pi/(1 - e^{-4\pi\zeta}) = 69.85$.

- Approximate quality factor $\widetilde{Q} = 1/(2\zeta) = 66.67$.
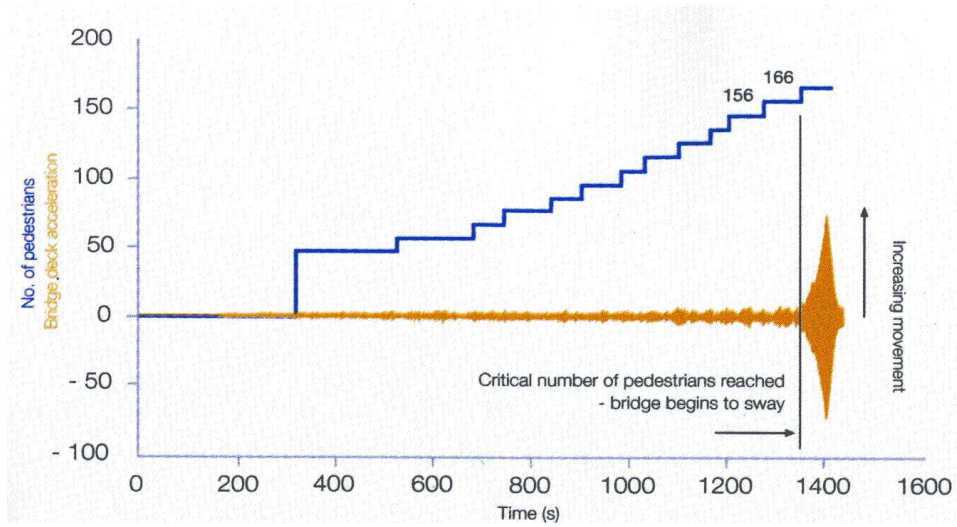
Figure 2.9: Controlled walker test used to determine critical number of walkers on the north span of the Millennium Bridge (taken from [24]). The blue staircase-like trace shows the number of walkers, while the lower red trace shows measured lateral acceleration of the bridge deck.

Table 2.1: A table of values for the Millennium Bridge. NL1 is the fundamental lateral mode on the north span, CL1 is the fundamental lateral mode on the center span, SL1 is the fundamental lateral mode on the south span, and CL2 is the first harmonic (second mode) on the center span. Data comes from from [6]. *Entries with an asterisk are theoretical estimates, not measured values. Entries for modal damping are calculated from the formula $B = 2\zeta M\Omega_0$, and entries for the spring constant are calculated from the formula $K = M\Omega_0^2$.

	NL1	CL1	SL1	CL2
Length $[m]$	81	144	108	144
Modal mass $[kg \times 10^3]$	113*	128–130	160	145–148
Resonant frequency $[Hz]$	1.03	0.48	0.80	0.95
Damping Ratio $[\%]$	0.6–0.8	0.765	0.6–0.8	0.6–0.8
Modal Damping $[kg/s \times 10^3]$	8.78–11.7	5.91–6.00	9.65–12.9	10.4–14.1
Spring Constant $[kg/s^2 \times 10^3]$	4730	1160–1180	4040	5170–5270
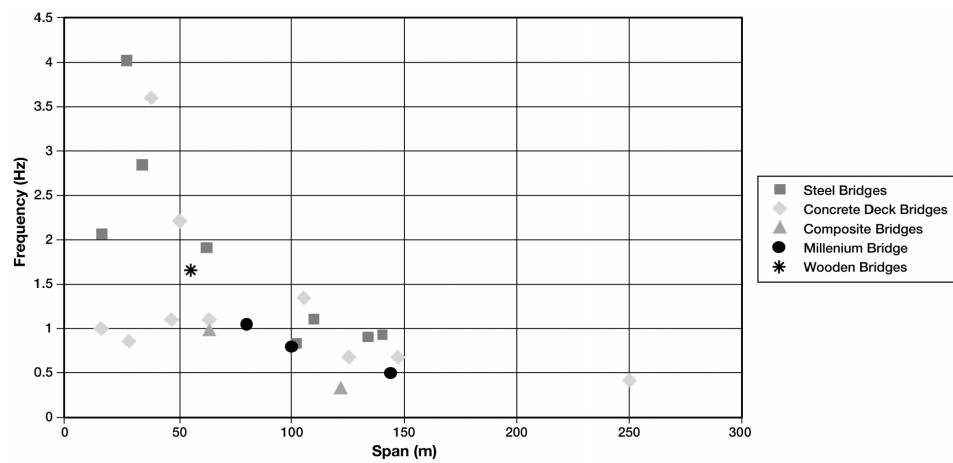
Figure 2.10: Natural frequencies of footbridge spans of varying lengths, composed of different materials. (taken from [7]).

CHAPTER 3

EXISTING MODELS OF THE MILLENNIUM BRIDGE

INSTABILITY

"It is venturesome to think that a coordination of words (philosophies are nothing more than that) can resemble the universe very much. It is also venturesome to think that of all those illustrious coordinations, one of them—at least in an infinitesimal way—does not resemble the universe a bit more than the others."

—Jorge Luis Borges

In this section, I review in general terms the existing theories for the cause of the lateral vibration on the Millennium Bridge. I point out limitations of each model and list predictions.

3.1 Josephson's Model

Two days after the Millennium Bridge was closed, a letter from Nobel-prize winning physicist Brian Josephson appeared in London's respected newspaper "The Guardian." This letter offered the first insight into what may have caused the unwanted vibration, and though it does not explicitly present mathematical equations, it might serve as a basis for a model[1]. The letter (still available as of the time of writing via the online Guardian archives at `http://www.guardian.co.uk/letters/story/0,3604,331652,00.html`) is quoted below:

---

[1]Private correspondence with Josephson later indicated that he feels Haken's synergetics [13] would be a good starting point for a mathematical model. The idea is that the walkers are "slaved" to the bridge's slight motion, and in trying to maintain their balance, they inadvertently pump energy into the bridge's vibration.

> **Out of step on the bridge**
>
> Wednesday June 14, 2000
>
> *The Guardian*
>
> The Millennium Bridge problem (Millennium bug strikes again, June 13) has little to do with crowds walking in step: it is connected with what people do as they try to maintain balance if the surface on which they are walking starts to move, and is similar to what can happen if a number of people stand up at the same time in a small boat. It is possible in both cases that the movements that people make as they try to maintain their balance lead to an increase in whatever swaying is already present, so that the swaying goes on getting worse.
>
> Is it true that "the bridge is never going to fall down", or at any rate get damaged, as a result of the swaying? That has been said about bridges before, and those responsible for this one need to understand, before making such pronouncements, that the problem involves more than engineering principles.
>
> Prof Brian Josephson
>
> Department of Physics
>
> University of Cambridge
>
> bdj10@cam.ac.uk

Predictions

Without a mathematical formulation, it is impossible to make quantitative predictions for comparison with experiment.

Limitations

The lack of an explicit model makes Josephson's comments interesting, but limited in applicability.

3.2 Arup's Model

In June of 2001, the first of several papers authored by Arup engineers was published by the Royal Academy of Engineering [10, 7, 6]. These papers describe the experiments done by Arup employees and the resulting theory that they developed to explain the onset of lateral oscillation.

The key result of Arup's work is an observation that pedestrians act like negative damping. Thus they formulate a model based on that assumption, where the correlated lateral force per person αF_1 is proportional to the local lateral bridge velocity V_{local}, i.e., $\alpha F_1 = k V_{local}$. The proportionality constant k was measured empirically to be about 300 kg/s (see Figure 3.1). The lateral correlated force was estimated in experiment by measuring the gain in kinetic energy per cycle, under the assumption that work done must have come from the difference between pedestrian forcing and known damping.

Predictions

Using their model for the pedestrian forcing, Arup found a formula for the critical number of pedestrians by solving for the point at which the bridge damping is exactly counteracted by pedestrians' effective negative damping:

$$N_c = 8\pi c f M/k \ .$$

(3.1)
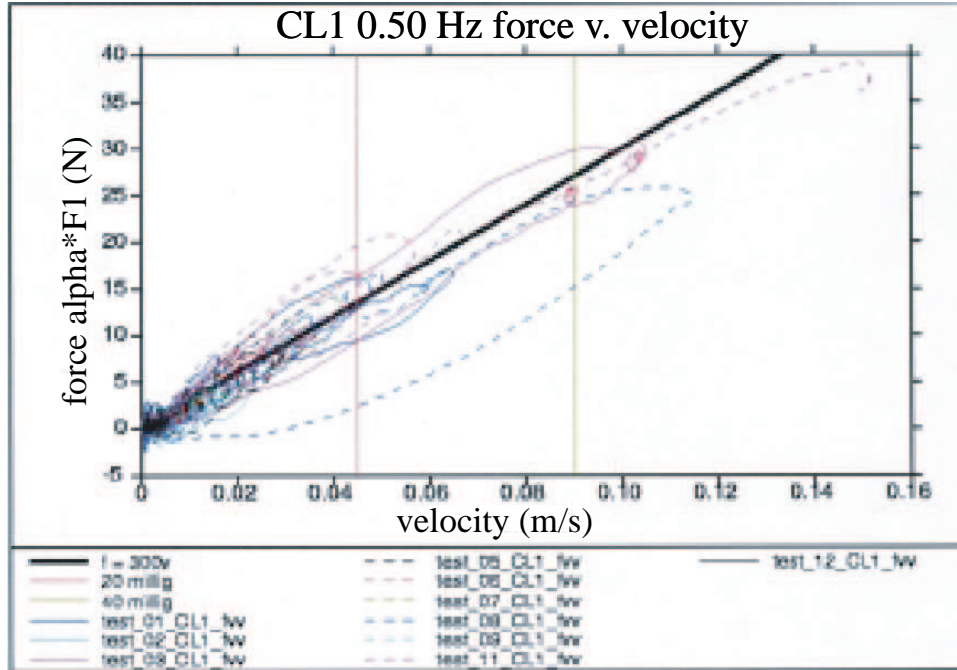
Figure 3.1: Arup's evidence for the linear relationship between amplitude of lateral forcing and velocity (taken from [6]). The heavy black line is a linear regression fit with a slope of approximately 300 kg/s.

Here c is the damping ratio (ζ in my notation), and f the natural frequency in Hz ($f_0 = \Omega_0/2\pi$ in my notation).

Plugging in for c in terms of the bridge parameters, their prediction reduces to $N_c = 2B/k$. On the north span, plugging in appropriate values for the bridge parameters (see Table 2.1) yields a prediction of approximately $N_c = 70$, the correct order of magnitude but off by more than a factor of two from the experiment, which showed $N_c \approx 165$.

Limitations

The primary disadvantage of Arup's model is the empirical nature of the description of pedestrians. The linear relationship between F and V should ideally be explained by the model, rather than assumed.

Also, the empirical law leaves no room for explanation of the observed synchronization effect. Born out by numerous firsthand accounts and video footage from opening day, synchronization clearly occurred and was related to the unwanted wobble. What caused people to fall into step?

Another downside to this approach is that the predicted critical number of pedestrians depends only on the damping, and is independent of the natural frequency of the bridge. One might expect different bridges (or spans) to have different critical thresholds. The effect of the walker frequency distribution is also unknown in this model.

Finally, the steady state amplitude for bridge motion cannot be predicted, as it is due to unmodeled nonlinearities in Arup's system.

3.3   Newland's Model

Professor Newland (Cambridge University) published two papers relating to the Millennium Bridge during July 2002 and July 2003.

His approach in the first publication is similar to that commonly taken in control theory, defining a transfer function for the effect of driving on the bridge and another for the feedback on the people.

He then assumes, based on the empirical evidence of Arup's tests, that the pedestrians naturally tend to shift their phases such that they maximally destabilize the bridge (a worst-case scenario). By solving for the phase in the feedback transfer function at which the bridge is maximally destabilized, he shows that pedestrians do indeed act like negative dampers (i.e., their force leads bridge displacement by $\pi/2$ in phase) under such assumptions.

In his second relevant publication, Dr. Newland includes a summary of data

about human driving frequencies under different conditions and the vertical and horizontal loading patterns (his Tables 1 and 2).

He then explores the problem with the approach of a delayed differential equation, assuming that pedestrian motion $z(t)$ is smaller in amplitude than bridge motion $y(t)$ and delayed by a value Δ, i.e., $z(t) = \alpha y(t - \Delta)$ where α is a positive real number less than 1.

A steady state assumption $y(t) = Y \exp(i\omega t)$ results in the stability condition for damping $C_{crit} = \alpha m \omega$, in his notation (Equations 9 and 11 in [19]). In my notation this would be expressed as $B_{crit} = \alpha(N m_{ped}/2)\Omega_0$, where α is a constant and m_{ped} is the average mass of a pedestrian.

For the modal mass of the pedestrians it is assumed that only some fraction β of the population locks into sync with the bridge, and both β and α are estimated from Arup's experimental data. Dr. Newland uses $\alpha \approx 2/3$ and $\beta \approx 0.4$.

Professor Newland goes on to reframe his criterion in terms of a so-called "Scruton Number" that he defines in terms of the bridge and walker parameters. This is an analogue to the dimensionless number commonly used to assess bridge stability to perturbations from wind excitation.

Predictions

We write $m = \beta N m_{ped}/2$, where $N m_{ped}$ is the total mass of pedestrians and the factor of 1/2 comes from the assumption of uniform distribution of pedestrians along a sinusoidal modeshape. Thus, expressing Dr. Newland's predictions in our notation, we have $N_c = 2B/\alpha\beta m_{ped}\Omega_0$ which gives $N_c \approx 170$ for parameters on the north span, very close to the observed value of about 165.

Limitations

Dr. Newland assumes a style of walker dynamics that should be observable, but does not give any evidence to support his idea for the delayed differential equation.

He assumes a worst case scenario in order to find his critical damping C_{crit}, though the justification is not provided.

He uses an empirical assumption that 40% of the walkers are locked to the bridge frequency regardless of that natural frequency and regardless of the amplitude of motion.

His set of equations does not account for differences in walker frequency distributions, and does not explain the onset of synchronization.

He does not address the question of steady-state amplitude of bridge motion.

3.4   Roberts' Model

In his 2003 paper [20], Dr. Roberts writes down a PDE with a 4th order spatial derivative as the governing equation for the bridge. His pedestrians have a sideways acceleration proportional to the interaction force, which is assumed sinusoidal with a frequency ω, different from the bridge frequencies ω_n which are expressed in terms of bridge parameters. His key assumption is that bridge displacement amplitude and pedestrian displacement amplitude will be equal in steady state oscillation. He eventually reaches a condition $N_p = \rho L/m_p \Omega^2 D$, where ρ is the mass per unit length of the bridge span, L the length of the span, m_p the mass of the average pedestrian, $\Omega = \omega/\omega_n$ is the frequency ratio, and D is the "dynamic amplification factor." When on resonance, $D = 1/(2\zeta)$. A table of values of $\Omega^2 D$ is given for different values of the damping ratio ζ and for different distributions of native

frequencies.

Predictions

In my one-dimensional variables, with pedestrian natural frequency matching the bridge fundamental, $N_c = M/(m_p D) = 2M\zeta/m_{ped} = B/m_{ped}\Omega_0$. This gives $N_c \approx$ 23 on the north span, a very low estimate. This estimate increases dramatically with some detuning or if a distribution of natural frequencies is assumed. For a uniform distribution of pedestrian frequencies between 0.9 Hz and 1.1 Hz on a 1 Hz bridge, the prediction becomes $N_c \approx 94$. Note that the formula is similar to Newland's when reduced to 1D.

His 2005 paper adds an additional 5th order mixed-derivative term for the bridge's governing equation. The new instability condition is expressed as $N_p = M_i L/M_{pi}\Omega_i^2 D$, where $\Omega_i = \omega/\omega_i = 1$ on resonance, $D = 1/2\zeta$ on resonance, M_i is the modal mass of the bridge, and $M_{pi} = (2L/\pi)m_p$ for a sinusoidal mode-shape at the fundamental frequency. Thus in our notation, his prediction is $N_c = \pi M\zeta/m_{ped}$. That gives $N_c \approx 36$ on the north span, again a very low estimate, however, it gives a much more reasonable $N_c \approx 147$ if the walker frequencies are assumed to be uniformly distributed between 0.9 and 1.1 Hz.

Limitations

Roberts assumes that pedestrians will synchronize so as to destabilize the bridge; he does not describe the underlying cause of the synchronization. Because of that, he can't describe the onset of the synchronization/vibration, and therefore can't explain Arup's empirical law for linearity between pedestrian forcing and bridge velocity.

3.5   Nakamura's Model

Nakamura's work [18] starts from the model by Arup, but includes the additional assumption that a pedestrian response to bridge motion will saturate at large amplitudes. That is, he assumes that Dallard's $\alpha F_1 \propto k V_{local}$ is only valid for small local bridge velocities.

After writing down the model, much of the paper is dedicated to presentation and interpretation of results from numerical integration of the model.

Predictions

Nakamura's predictions match those of Arup for onset of the instability. His work differs in that the steady state amplitude may be predicted, although no algebraic solution is given, only numerical results.

Limitations

The limitations to Nakamura's model are the same as those that were observed for Arup's model. The empirical nonlinearity between αF_1 and V_{local} is observed but not explained, synchronization is assumed but not explained, and the critical number of pedestrians implicit in Nakamura's model is independent of the natural frequency of the bridge.

3.6   Fujino's Model

Fujino et al [11] start by modeling the bridge as a damped harmonic oscillator, driven sinusoidally by a crowd of identical walkers whose phases are initially randomly distributed. The implied predictions for steady-state amplitude are too

small, so the authors review footage of a case of synchronous lateral excitation, and find that approximately 20% of the crowd is phase-synchronized. Using that assumption, they modify their predictions and find that the steady-state amplitudes in their model with 20% synchronization are reasonable.

Predictions

Fujino et al predict that about 20% of the walkers on a laterally vibrating bridge will synchronize in phase. The steady state amplitude that they predict comes from the steady state behavior of a sinusoidally driven damped harmonic oscillator.

In the case of the Millennium Bridge, that prediction would be about 3mm without any phase synchronization, and about 2cm with 20% synchronization, the correct order of magnitude.

Limitations

The model proposed by Fujino et al does not predict any sudden transition to a vibrating bridge state; rather it assumes a continuous increase in the vibration amplitude as the number of walkers increases. This conflicts with the observations made by Arup on the Millennium Bridge.

Also, Fujino's model uses the empirical value of 20% synchronization without providing a theoretical basis. It doesn't indicate what causes that partial sync to occur, or at what amplitude it begins to happen.

Finally, this model cannot account for the observed linearity between the magnitude of pedestrian forcing and peak bridge velocity, since pedestrian forcing is independent of time (it depends only on the number of walkers), whereas the peak bridge velocity builds up throughout the transient growth of bridge vibrations.

CHAPTER 4

OUR MODEL OF THE MILLENNIUM BRIDGE INSTABILITY

Our goal was to create a simplified set of equations that capture the essential dynamics for both pedestrians and the bridge. The key difference from previous models is the attempt to model the behavior of the pedestrians with tools borrowed from mathematical biology, which we hoped would allow us to predict both the onset of instability and the onset of crowd synchronization.

4.1 The Bridge

We begin by using the simplest model for a single span of the Millennium Bridge - a damped harmonic oscillator:

$$M\frac{d^2X}{dt^2} + B\frac{dX}{dt} + KX = F_{ped} \ . \tag{4.1}$$

Here M is the modal mass of the bridge, B is the modal damping and K is the modal stiffness. F_{ped} is the net force exerted by the pedestrians on the bridge,

$$F_{ped} = G\sum_{i=1}^{N}\sin\Theta_i \ , \tag{4.2}$$

where G is the amplitude of the lateral forcing and Θ_i is the phase in the walking cycle for each of the N pedestrians. We approximate the pedestrian forcing as sinusoidal, although the real data in Figure 4.4 reveals this to be a somewhat crude idealization.

4.2 The Walkers

The more difficult equation for us to write down was the governing equation for the pedestrians. It's difficult for several reasons. First of all, very few studies have
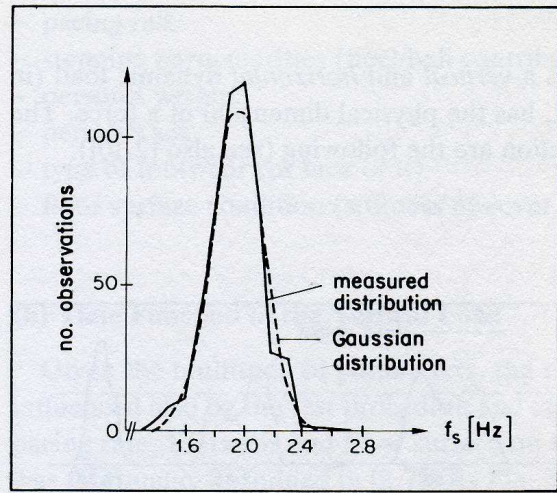
Figure 4.1: A graph of walker frequency distributions in a representative sample of the population, reprinted from [3], who reprinted it from [15]. The frequencies shown are for vertical forcing, so the lateral frequencies dealt with in this dissertation would be half those. Bachmann cites publications in German indicating a standard deviation between 0.13Hz and 0.3Hz for vertical forcing frequencies.

been done on the response of pedestrians to lateral forcing [16, 6]. Those that have been done do not measure the details of the response dependency on the frequency of the forcing, and they do not keep track of the phase relationship between the walker and the oscillating platform.

There is ample data about undriven pedestrian behavior in the literature. Walkers tend to have a natural frequency of pacing that varies depending on the height and weight of the individual. A representative sample of the population will show a bell-shaped distribution of frequencies, with a measurable standard deviation [3] (see Figure 4.1).

For that reason, we model the pedestrians as limit-cycle phase oscillators with a distribution of native frequencies. In an undriven system, we set

$$\frac{d\Theta_i}{dt} = \Omega_i \, ,$$

where Θ_i represents the phase and Ω_i the native frequency of the ith pedestrian.
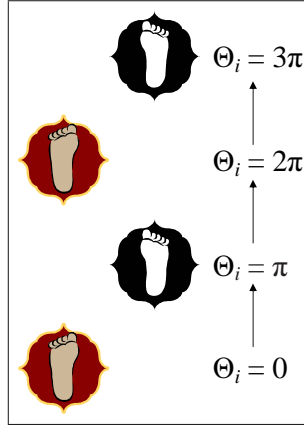
Figure 4.2: A diagram showing the definition of Θ_i.

Phases can be interpreted in various ways, but one simple measure would be to take $\Theta_i = 0$ when the pedestrian's left foot first touches the ground, and $\Theta_i = \pi$ when his or her right foot makes contact with the ground, interpolating for phases between these events (see Figure 4.2). Of course this is subject to the arbitrary choice of any constant additive phase.

Thus far there is nothing controversial in our model of a pedestrian. However, the effect of a laterally oscillating surface must now be included. To jump directly to the point, our model is

$$\frac{d\Theta_i}{dt} = \Omega_i + C_i A \sin(\Psi - \Theta_i + \alpha) \ . \tag{4.3}$$

Here C_i, with units of angle/distance per unit time, measures the sensitivity of a pedestrian to lateral oscillation of a given amplitude. A is that amplitude of the bridge's oscillation, Ψ is the phase of the bridge in its oscillating motion, and α is a constant "phase-lag" parameter that is determined by a pedestrian's desired phase relationship with the moving surface.
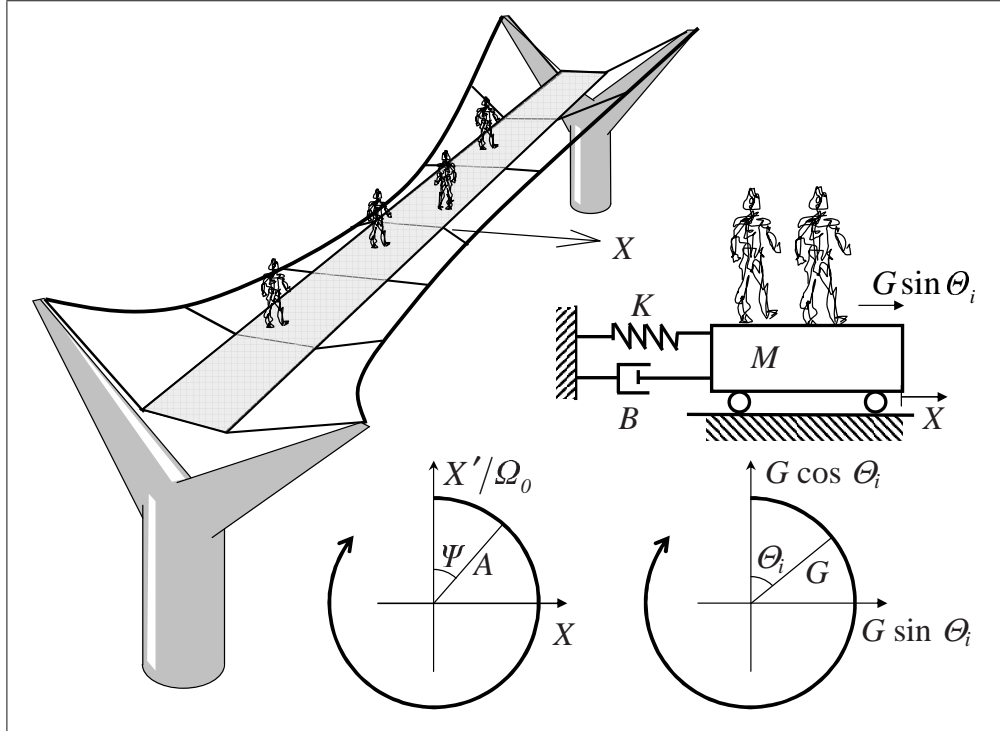
Figure 4.3: A schematic diagram showing the definitions of X, A, and Ψ. (Figure designed by Allan McRobie.)

4.2.1 Biological Oscillators

We chose the form 4.3 in analogy with a model taken from mathematical biology [9, 21, 17]. In Ermentrout & Rinzel's model, fireflies are observed to alter the frequency of their flashing in response to observed signals from others. Each firefly has its own native frequency at which it flashes when isolated from its peers. However, the phase in its flashing cycle can be influenced by observed flashes from others, and Ermentrout & Rinzel use the model:

$$\frac{d\theta}{dt} = \omega + A\sin(\Theta - \theta) \ , \tag{4.4}$$

where θ is an individual firefly's phase, ω the firefly's native frequency, and Θ the phase of the stimulus signal.

Similar models have been used for human rhythmic finger tapping, cricket

chirping, and non-biological oscillations such as those observed in laser arrays and phase-locked-loops.

Because human walking is governed by unconscious rhythmic biological signals, it seems possible that an analogy with the rhythmic flashing of fireflies may be apt, at least as a first approximation.

4.2.2   A Minimal Model

Another justification of our choice for (4.3) is that it is the simplest reasonable governing equation that can produce synchronization behavior.

You could imagine some general response function of the form

$$\frac{d\Theta_i}{dt} = \Omega_i + f(A, \Psi, \Theta_i) \; , \tag{4.5}$$

where f may be a function of the bridge motion amplitude, the bridge phase, and the walker phase. In fact, we could even imagine that f might depend on the history of interaction with the bridge, or other variables such as the walker's lateral amplitude or the bridge frequency. But if we assume that the phenomena is driven mostly by physical kinetics, the above three variables should suffice.

In order to create a model in which synchronization is a possible outcome, f have the effect of shifting walkers to a phase closer to that of the bridge. So f must be positive, to increase the walker frequency, when Θ lags Ψ. Similarly, it must be negative when Θ leads Ψ. Thus f must look like $f \propto \Psi - \Theta$ for small values of $\Psi - \Theta$. Of course f must be periodic in $\Psi - \Theta$, and the simplest periodic function that satisfies these requirements is $f \propto \sin(\Psi - \Theta)$. This can be interpreted as taking the first term in a Fourier expansion of an arbitrary periodic function f.

The same argument holds if we want Θ to synchronize at a constant phase offset $\Psi + \alpha$ rather than Ψ, as in (4.3). Then we must have $f \propto \sin(\Psi + \alpha - \Theta)$.

Regarding the constant of proportionality, we know that the effect should not occur if the amplitude of the bridge motion is below the threshold for detection by the walkers. That is, it should satisfy $f = 0$ when $A = 0$. It seems a reasonable first approximation to take f as a smooth function in A, and it is believable that the influence of the bridge becomes stronger as the amplitude of the bridge's motion increases. Therefore we can write $f \propto \sum_{n=0}^{\infty} c_n A^n$, where dependence on A is expanded in a power series for a monotonically increasing function, with $c_0 = 0$. The simplest case, to be used in our first approximation model, is to assume a linear relationship $f \propto A$.

The constant of proportionality used in $f \propto A$ will determine how big an effect bridge motion of a given amplitude has on a walker. It determines the maximum phase shift for a given bridge amplitude, and so acts like a "sensitivity" to bridge motion.

Since this phenomenon has not been explored in the literature, it seems natural to assume that there may be some variation among individuals in the population. We should in general use a (perhaps Gaussian) distribution C_i for these sensitivities, but since nothing is known a priori about the width or mean of the distribution, we will later make the simplifying assumption that $C_i = C$, a single value for all walkers.

This is how we arrived at the model in equation (4.3):

$$\frac{d\Theta_i}{dt} = \Omega_i + C_i A \sin(\Psi - \Theta_i + \alpha) \ .$$

4.2.3 Constants in Our Model

We take $G = 30$ Newtons for the mean amplitude of lateral forcing by a pedestrian during normal walking. Figure 4.4 shows a typical time series for lateral forcing
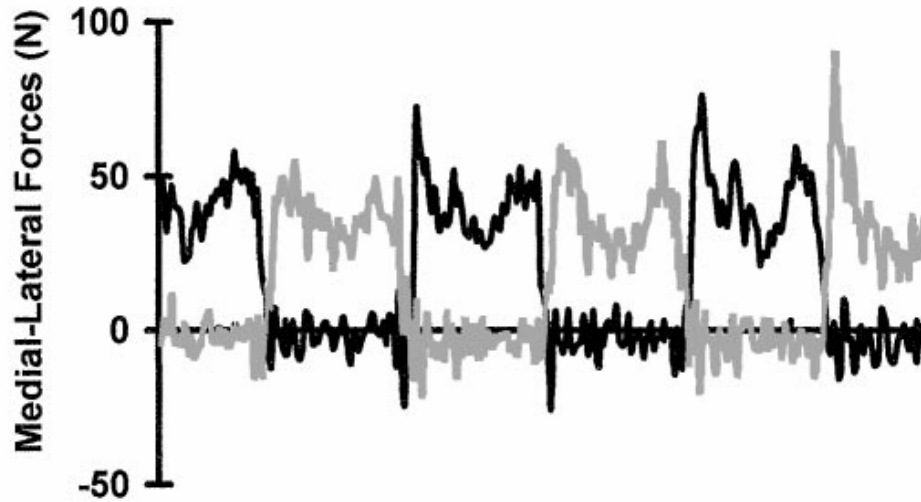
Figure 4.4: Typical time series of lateral forcing for a 63 kg pedestrian on a treadmill (taken from [5]). The black trace corresponds to the rightward force, while the gray trace represents the leftward force (measured independently).

as measured by experiments on a treadmill in [5]. Measurements by McRobie et al reinforce this number as a reasonable estimate [16].

We choose to use $C = 16m^{-1}s^{-1}$ for the pedestrian sensitivity. This choice was made in order for the model to give reasonable results when compared with experimental data such as that shown in Figure 2.9. A fairly simple experiment could determine an objective value for C and would be very welcome.

4.3 Other Possible Walker Models

It is possible to imagine several models of pedestrian behavior that differ radically from ours. One candidate would be a model in which a walker can shift not only her phase, but also her native frequency in response to bridge motion. This would be analogous to a biological model for synchronization in both fireflies and cricket chirping [8]. It might look like (4.5), but with Ω_i replaced by a function $\Omega(A, \Omega_0)$.

4.4 Scaling the Model

The complete model, as given in equations (4.1), (4.2), and (4.3) above, is

$$M\frac{d^2 X}{dt^2} + B\frac{dX}{dt} + KX = G\sum_{i=1}^{N} \sin\Theta_i \; , \tag{4.6}$$

$$\frac{d\Theta_i}{dt} = \Omega_i + C_i A\sin(\Psi - \Theta_i + \alpha), \qquad i = 1\ldots N \; .$$

We start our analysis by non-dimensionalizing the model. We need to find a length scale and a time scale with which to scale the dimensional variables X, A, and Ω_i. An obviously relevant time scale is determined by the bridge's natural frequency Ω_0. However, two plausible length scales can be found via combinations of the parameters:

$$L_1 = NG/K$$

$$L_2 = \Omega_0/C \; .$$

L_1 is a measure of the displacement that would be caused by a static load equal to the lateral force of N synchronized pedestrians.

L_2 measures the bridge oscillation amplitude necessary to produce a unit change in phase per unit time for a pedestrian of sensitivity C.

When we tried to use either L_1 or L_2 as the length scale for our nondimensionalization, we found that it was problematic to establish a small parameter in the resulting equations for use in perturbation theory. The small parameter ϵ would only appear in one or the other $\mathcal{O}\left(1\right)$ equation, but not both. In essence, the problem boiled down to L_1 being too small, and L_2 being too large, given realistic assumptions about the parameter ranges. Neither gave a realistic scale for A.

During Spring 2005—the time we were working on this problem—Dr. Strogatz and I were visitors at Denmark's Niels Bohr Institute. After a short time of being

frustrated by this nondimensionalization issue, I can recall eating lunch together one day at a picnic table near the cafeteria. We thought, "If L_1 is too big, and L_2 is too small, why not try their mean?"

Happily, that approach was successful. The best length scale for our purposes turned out to be their geometric mean, $L = \sqrt{L_1 L_2}$. With that scaling, the small parameter $\epsilon = \sqrt{L_1/L_2}$ came out of the equations immediately, and ϵ appeared in both $\mathcal{O}(1)$ equations in perturbation theory—the bridge equation and the walker equation.

Thus the scaling we finally chose was:

$$
\begin{aligned}
\tau &= \Omega_0 t \\
x &= X/L \\
a &= A/L \;,
\end{aligned}
\tag{4.7}
$$

with parameters

$$
\begin{aligned}
\Omega_0 &= \sqrt{K/M} \\
\zeta &= \frac{B\Omega_0}{2K} \\
L &= \sqrt{L_1 L_2} = \sqrt{\frac{NG\Omega_0}{KC}} \\
\epsilon &= \sqrt{L_1/L_2} = \sqrt{\frac{NGC}{K\Omega_0}} \;.
\end{aligned}
\tag{4.8}
$$

The governing equations of the model could now be rewritten in dimensionless form as

$$
\begin{aligned}
\frac{d^2x}{d\tau^2} + 2\zeta\frac{dx}{d\tau} + x &= \epsilon\langle\sin\Theta_i\rangle \;, \\
\frac{d\Theta_i}{d\tau} &= \frac{\Omega_i}{\Omega_0} + \epsilon a\sin(\Psi - \Theta_i + \alpha), \qquad i = 1\ldots N \;.
\end{aligned}
\tag{4.9}
$$

Here we've introduced the shorthand notation of using angle brackets to indicate

an average over all oscillators,

$$\langle Y_i \rangle = \frac{1}{N} \sum_{i=1}^{N} Y_i \; , \qquad (4.10)$$

where Y_i is any function that can be evaluated for each oscillator.

In the limit of $\epsilon \to 0$, system (4.9) becomes

$$\frac{d^2 x}{d\tau^2} + 2\zeta \frac{dx}{d\tau} + x \; = \; 0 \; , \qquad (4.11)$$

$$\frac{d\Theta_i}{d\tau} \; = \; \frac{\Omega_i}{\Omega_0}, \qquad i = 1 \ldots N \; .$$

These are the governing equations for an undriven damped harmonic oscillator and a set of N uncoupled limit cycle oscillators. They correspond to the case of weak or insensitive pedestrians on a stiff bridge, and can produce no interesting phenomena, as expected.

4.5 Assumptions

In order to apply perturbation theory to the system (4.9), we must make some assumptions about the damping ratio ζ and the distribution of pedestrian natural frequencies Ω_i. We assume—as is realistic for most suspension bridges—that the damping for lateral motion is small, i.e.,

$$\zeta = \epsilon b \; , \qquad (4.12)$$

where b is assumed to be $\mathcal{O}(1)$ or smaller. The measured value for ζ on the Millennium bridge was about 0.0075.

We also assume that the pedestrians' native frequencies are close to the natural frequency of the bridge, i.e.,

$$\frac{\Omega_i}{\Omega_0} = 1 + \epsilon \omega_i \; . \qquad (4.13)$$

Here ω_i is the "detuning" from the bridge frequency, and is assumed to be $\mathcal{O}(1)$ or smaller. The limits of this assumption will be tested later on, but it should be valid for any bridge span having a natural frequency in the range of 0.75-1.25 Hz, near normal walking frequencies. More plainly, it seems reasonable to think that the pedestrians are most likely to excite a bridge when they are walking at a frequency near resonance.

Objections to this assumption have been raised by Pat Dallard and others at Arup. We feel that our model is a reasonable description at this level of complexity, and that the additional complication of super or sub-harmonic resonance can be dealt with after a fundamental understanding has been established.

Applying (4.12) and (4.13) to the model in (4.9), we get

$$
\begin{aligned}
\frac{d^2x}{d\tau^2} + x &= \epsilon\left[\langle\sin\Theta_i\rangle - 2b\frac{dx}{d\tau}\right] \;, \\
\frac{d\Theta_i}{d\tau} &= 1 + \epsilon\left[\omega_i + a\sin(\Psi - \Theta_i + \alpha)\right], \qquad i = 1\ldots N \;.
\end{aligned}
\tag{4.14}
$$

4.6 Rotating Frame

One final simplification can be made by changing to a rotating frame, moving at the undamped natural frequency of the bridge Ω_0. We'll set

$$
\theta_i = \Theta_i - \Omega_0 t = \Theta_i - \tau,
$$

$$
\psi = \Psi - \Omega_0 t = \Psi - \tau \;,
\tag{4.15}
$$

which leads to the following governing equations for the model in the rotating frame:

$$
\begin{aligned}
\frac{d^2x}{d\tau^2} + x &= \epsilon\left[\langle\sin(\tau + \theta_i)\rangle - 2b\frac{dx}{d\tau}\right] \;, \\
\frac{d\theta_i}{d\tau} &= \epsilon\left[\omega_i + a\sin(\psi - \theta_i + \alpha)\right], \qquad i = 1\ldots N \;.
\end{aligned}
\tag{4.16}
$$

4.7 Perturbation Theory

In the limit $\epsilon \to 0$, the system (4.16) has solution $x(\tau) = a\sin(\tau + \psi)$, $\theta_i = \text{const}$, where a and ψ are constants. When ϵ is small but nonzero, the dimensionless bridge amplitude a and the bridge phase ψ will both drift slowly, on a slow time scale $\mathcal{O}\left(1/\epsilon\right)$.

We are making an explicit assumption here that $\epsilon \ll 1$. In section 4.11 we will verify that this assumption is appropriate and justified for the case of the Millennium Bridge, but for the moment, just trust us!

4.7.1 Developing Slow-Time Equations

We use the perturbative method of averaging to find a new set of governing equations in a slow time variable

$$T = \epsilon \tau \ . \tag{4.17}$$

Consider the form of the system in equation (4.16) above,

$$\frac{d^2 x}{d\tau^2} + x = \epsilon f \ , \tag{4.18}$$

where f is an arbitrary function. Derivatives with respect to τ can be expanded in terms of the slow time variable $T = \epsilon \tau$ to get

$$\frac{dx}{d\tau} = \frac{\partial x}{\partial \tau} + \frac{\partial x}{\partial T}\frac{\partial T}{\partial \tau} = \left(\frac{\partial}{\partial \tau} + \epsilon\frac{\partial}{\partial T}\right)x \tag{4.19}$$

and

$$\begin{aligned}
\frac{d^2 x}{d\tau^2} &= \frac{d}{d\tau}\left(\frac{\partial x}{\partial \tau} + \epsilon\frac{\partial x}{\partial T}\right) \\
&= \frac{\partial}{\partial \tau}\left(\frac{\partial x}{\partial \tau} + \epsilon\frac{\partial x}{\partial T}\right) + \epsilon\frac{\partial}{\partial T}\left(\frac{\partial x}{\partial \tau} + \epsilon\frac{\partial x}{\partial T}\right) \\
&= \left(\frac{\partial^2}{\partial \tau^2} + 2\epsilon\frac{\partial^2}{\partial T\partial \tau}\right)x + \mathcal{O}\left(\epsilon^2\right) \ ,
\end{aligned} \tag{4.20}$$

assuming that mixed partial derivatives are equal (always valid for a physical variable like x, which must be twice continuously differentiable in time). Thus equation (4.18) becomes, to first order in ϵ,

$$\frac{\partial^2 x}{\partial \tau^2} + 2\epsilon \frac{\partial^2 x}{\partial T \partial \tau} + x = \epsilon f \ . \tag{4.21}$$

Expanding x as a power series in ϵ

$$x = x_0 + \epsilon x_1 + \epsilon^2 x_2 + \dots \ , \tag{4.22}$$

plugging it into equation (4.21), and retaining only terms of order ϵ or lower yields

$$\frac{\partial^2 x_0}{\partial \tau^2} + x_0 + \epsilon \left(\frac{\partial^2 x_1}{\partial \tau^2} + x_1 + 2\frac{\partial^2 x_0}{\partial T \partial \tau} \right) = \epsilon f \ . \tag{4.23}$$

Matching terms at the different orders of ϵ gives two equations:

$$\mathcal{O}\left(1\right): \qquad \frac{\partial^2 x_0}{\partial \tau^2} + x_0 = 0, \tag{4.24}$$

$$\mathcal{O}\left(\epsilon\right): \qquad \frac{\partial^2 x_1}{\partial \tau^2} + x_1 + 2\frac{\partial^2 x_0}{\partial T \partial \tau} = f \ . \tag{4.25}$$

The solution to (4.24) can be written as

$$x_0 = a(T)\sin(\tau + \psi(T)) \ , \tag{4.26}$$

where $\psi(T)$ is a slowly varying phase. So

$$\begin{aligned}
\frac{\partial^2 x_0}{\partial T \partial \tau} &= \frac{\partial}{\partial T}\left[a(T)\cos(\tau + \psi(T))\right] \\
&= \frac{\partial a}{\partial T}\cos(\tau + \psi(T)) - a\sin(\tau + \psi(T))\frac{\partial \psi}{\partial T} \ .
\end{aligned}$$

Plugging that into (4.25) gives

$$\frac{\partial^2 x_1}{\partial \tau^2} + x_1 = f - 2\frac{\partial a}{\partial T}\cos(\tau + \psi(T)) + 2a\frac{\partial \psi}{\partial T}\sin(\tau + \psi(T)) \ . \tag{4.27}$$

Remove Secular Terms

In order to ensure that the solution to (4.27) be bounded, we must remove any secular terms—those with resonant frequency—from the right hand side. We can do that by imposing the condition that the right hand side be orthogonal to both the homogeneous solutions, $\sin(\tau + \psi(T))$ and $\cos(\tau + \psi(T))$.

Starting with $\sin(\tau + \psi(T))$:

$$\oint f \sin(\tau + \psi(T))d\tau \quad - \quad \oint 2\frac{\partial a}{\partial T}\cos(\tau + \psi(T))\sin(\tau + \psi(T))d\tau \; +$$
$$+ \quad \oint 2a\frac{\partial \psi}{\partial T}\sin^2(\tau + \psi(T))d\tau = 0 \; .$$

As usual in this type of calculation, we treat slow variables as constants during integration over one (fast) cycle. This may introduce an error of $\mathcal{O}\left(\epsilon^2\right)$, which is acceptable for small ϵ:

$$\oint f \sin(\tau + \psi(T))d\tau + 2a\frac{\partial \psi}{\partial T}\oint \sin^2(\tau + \psi(T))d\tau = 0 \; ,$$

so

$$\oint f \sin(\tau + \psi(T))d\tau = -a\frac{\partial \psi}{\partial T} \; . \tag{4.28}$$

Repeating for $\cos\tau + \psi(T)$):

$$\oint f \cos(\tau + \psi(T))d\tau \quad - \quad \oint 2\frac{\partial a}{\partial T}\cos^2(\tau + \psi(T))d\tau \; +$$
$$+ \quad \oint 2a\frac{\partial \psi}{\partial T}\sin(\tau + \psi(T))\cos(\tau + \psi(T))d\tau = 0 \; ,$$

so

$$\oint f \cos(\tau + \psi(T))d\tau = \frac{\partial a}{\partial T} \; . \tag{4.29}$$

Equations (4.28) and (4.29) constitute a system in the slow-time variable T that can be analyzed given a specific form for the function f.

4.7.2 Applying Slow-Time Equations

Equations (4.28) and (4.29) can now be used to analyze our system (4.16). Here $f = \langle \sin(\tau + \theta_i) \rangle - 2b\frac{dx}{d\tau}$, but we use only the lowest order expression for x in the derivative term to avoid quantities of $\mathcal{O}(\epsilon^2)$ (recall that f already has a pre-factor of ϵ in equation (4.18)). So we plug $x = x_0$ from equation (4.26) and simplify, retaining only terms of $\mathcal{O}(1)$,

$$
\begin{aligned}
f &= \langle \sin(\tau + \theta_i) \rangle - 2b\frac{dx}{d\tau} \\
&= \langle \sin(\tau + \theta_i) \rangle - 2b\frac{\partial x_0}{\partial \tau} \\
&= \langle \sin(\tau + \theta_i) \rangle - 2ba\cos(\tau + \psi(T))
\end{aligned} \tag{4.30}
$$

First Equation

Using the value of f from (4.30) in the first slow-time equation (4.28), we can first simplify the expression due to orthogonality between sine and cosine:

$$
\begin{aligned}
\oint [\langle \sin(\tau + \theta_i) \rangle - 2ba\cos(\tau + \psi(T))] \sin(\tau + \psi(T))d\tau &= -a\frac{\partial \psi}{\partial T}, \\
\oint \langle \sin(\tau + \theta_i) \rangle \sin(\tau + \psi(T))d\tau &= -a\frac{\partial \psi}{\partial T}.
\end{aligned} \tag{4.31}
$$

Recall from (4.10) that the angle bracket indicates an average over all oscillators, and thus the integral on the left hand side of (4.31) can be rewritten as

$$
\begin{aligned}
\oint \langle \sin(\tau + \theta_i) \rangle \sin(\tau + \psi(T))d\tau &= N^{-1}\oint \sum_{i=1}^{N} [\sin(\tau + \theta_i)] \sin(\tau + \psi(T))d\tau, \\
&= N^{-1}\sum_{i=1}^{N} \oint \sin(\tau + \theta_i) \sin(\tau + \psi(T))d\tau.
\end{aligned}
$$

Trigonometric expansion, together with the orthogonality of sine and cosine,

allow the evaluation of the integral above to get

$$\oint \langle \sin(\tau + \theta_i) \rangle \sin(\tau + \psi(T)) d\tau = \frac{1}{2} N^{-1} \sum_{i=1}^{N} \cos(\theta_i - \psi(T)) ,$$

$$= \frac{1}{2} \langle \cos(\theta_i - \psi(T)) \rangle . \tag{4.32}$$

Going back to equation (4.31), we now have a closed form for the first slow-time equation:

$$a \frac{\partial \psi}{\partial T} = -\frac{1}{2} \langle \cos(\theta_i - \psi) \rangle . \tag{4.33}$$

Second Equation

By a similar process to what was done above, but this time plugging (4.30) into equation (4.29):

$$\frac{\partial a}{\partial T} = \oint \left[\langle \sin(\tau + \theta_i) \rangle - 2ba \cos(\tau + \psi(T)) \right] \cos(\tau + \psi(T)) d\tau ,$$

$$\frac{\partial a}{\partial T} = \oint \langle \sin(\tau + \theta_i) \rangle \cos(\tau + \psi(T)) d\tau - 2ba \oint \cos^2(\tau + \psi(T)) d\tau ,$$

$$ba + \frac{\partial a}{\partial T} = \oint \langle \sin(\tau + \theta_i) \rangle \cos(\tau + \psi(T)) d\tau .$$

Changing the order of integration and summation, and simplifying yields the second slow-time equation:

$$\frac{\partial a}{\partial T} = \frac{1}{2} \langle \sin(\theta_i - \psi) \rangle - ba . \tag{4.34}$$

Third Equation

The second equation in the system (4.16) provides us with one more slow-time equation. Expanding the derivative on the left hand side gives:

$$\frac{d\theta_i}{d\tau} = \frac{\partial \theta_i}{\partial \tau} + \epsilon \frac{\partial \theta_i}{\partial T} = \epsilon \left[\omega_i + a \sin(\psi - \theta_i + \alpha) \right] . \tag{4.35}$$

From this expression, it's clear that θ_i evolves on a time scale of T, because the entire right hand side is multiplied by the pre-factor ϵ. Equating terms of order ϵ yields the third slow-time equation,

$$\frac{\partial \theta_i}{\partial T} = \omega_i + a \sin(\psi - \theta_i + \alpha) . \tag{4.36}$$

Slow-Time System

The slow-time equations derived above in (4.33), (4.34), and (4.36) can be summarized as follows (and henceforth we'll use the more compact notation of an overdot to represent derivatives with respect to slow time T):

$$\begin{aligned}
a\dot{\psi} &= -\frac{1}{2} \langle \cos(\theta_i - \psi) \rangle , \\
\dot{a} &= \frac{1}{2} \langle \sin(\theta_i - \psi) \rangle - ba, \\
\dot{\theta}_i &= \omega_i + a \sin(\psi - \theta_i + \alpha), \qquad i = 1, \ldots, N .
\end{aligned} \tag{4.37}$$

The similarity of the system (4.37) to the well-studied Kuramoto model [14, 22] is useful for our subsequent analysis. The following work uses his approach in many respects.

Order Parameter Formulation

It's possible to define an order parameter as the centroid of the distribution of phase oscillators in the complex plane (assuming unit amplitude for each oscillator),

$$R e^{i\Phi} = \left\langle e^{i\theta_j} \right\rangle . \tag{4.38}$$

So

$$\begin{aligned}
R \cos \Phi &= \langle \cos \theta_j \rangle , \\
R \sin \Phi &= \langle \sin \theta_j \rangle .
\end{aligned} \tag{4.39}$$

Here R can be interpreted as a measure of the degree of phase synchronization in the population of oscillators. When the system is fully phase-synchronized, we'll have $R = 1$. When the system is uncorrelated (independent randomly phased oscillators), we should have $R \sim 1/\sqrt{N}$, with $R \to 0^+$ as the number of oscillators increases.

We can rewrite the system (4.37) in terms of R and Φ by noting the following trigonometric relationships:

$$
\begin{aligned}
\langle \cos(\theta_j - \psi) \rangle &= \langle \cos \theta_j \rangle \cos \psi + \langle \sin \theta_j \rangle \sin \psi, \\
&= R \cos \Phi \cos \psi + R \sin \Phi \sin \psi, \\
&= R \cos(\Phi - \psi) , \quad\quad\quad\quad\quad\quad (4.40)
\end{aligned}
$$

$$
\begin{aligned}
\langle \sin(\theta_j - \psi) \rangle &= \langle \sin \theta_j \rangle \cos \psi - \langle \cos \theta_j \rangle \sin \psi, \\
&= R \sin \Phi \cos \psi - R \cos \Phi \sin \psi, \\
&= R \sin(\Phi - \psi) . \quad\quad\quad\quad\quad\quad (4.41)
\end{aligned}
$$

So the system becomes

$$
\begin{aligned}
a\dot{\psi} &= -\frac{1}{2} R \cos(\Phi - \psi), \\
\dot{a} &= \frac{1}{2} R \sin(\Phi - \psi) - ba, \\
\dot{\theta}_i &= \omega_i + a \sin(\psi - \theta_i + \alpha), \quad\quad i = 1 \ldots N . \quad\quad (4.42)
\end{aligned}
$$

4.8   Steady-States in the Slow-Time System

The system (4.37) has two steady-state solutions that we can be found, corresponding to the motionless bridge and the oscillating bridge. In this chapter we will consider the existence of these two solutions, and in Chapter 5 we'll discuss stability.

4.8.1 Motionless Bridge - Incoherent State

The motionless bridge is described by the state where the dimensionless amplitude of vibration $a = 0$. In that case, (4.37) becomes

$$
\begin{aligned}
\langle \cos(\theta_i - \psi) \rangle &= 0, \\
\langle \sin(\theta_i - \psi) \rangle &= 0, \\
\dot{\theta}_i &= \omega_i, \qquad i = 1 \ldots N \ .
\end{aligned}
\tag{4.43}
$$

Thus, in this situation the bridge remains motionless and each pedestrian walks at his own natural frequency Ω_i. This can be seen by changing variables back to the original dimensional system,

$$
\begin{aligned}
\frac{d\Theta_i}{dt} &= \frac{\partial \Theta_i}{\partial t} + \frac{\partial \Theta_i}{\partial T}\frac{\partial T}{\partial t} \\
&= \Omega_0 + \epsilon \Omega_0 \frac{\partial \theta_i}{\partial T} \\
&= \Omega_0(1 + \epsilon \omega_i) \\
&= \Omega_i,
\end{aligned}
$$

where we've used (4.15), (4.43), and (4.13) along with the chain rule.

Because each pedestrian walks at his or her own natural frequency, and there is a distribution of natural frequencies in the pedestrian population, the net forcing on the bridge averages out to zero. Pacing is incoherent, with no correlation between the footfall times of different walkers.

The condition (4.43) requires that $\langle \cos\theta_i \rangle = \langle \sin\theta_i \rangle = 0$ initially, and that this persist for all time. For finite N, this can only be satisfied by choosing values of θ_i so that all oscillators with a given frequency ω have a centroid at the origin in the phase plane. That type of initial condition must occur for all frequencies ω, and will then persist for all time as the oscillators of each frequency rotate rigidly,

thus maintaining the centroid at the origin.

This becomes reasonable only in the large N limit, when a random distribution of phases will mean that the centroid is very close to the origin for each frequency ω.

Note that this incoherent state can exist for all values of α, for all distributions of ω_i.

4.9 Partially Synchronized State

Starting from (4.37), we will assume that some of the oscillators have locked to the bridge, and we will go into a rotating reference frame moving at the combined frequency q, which will be determined at the end of the calculation.

4.9.1 Rotating Frame

Taking q as the frequency of the bridge and locked oscillators, we transform to a co-rotating frame,

$$
\begin{aligned}
\theta_i &= qT + \phi_i, \\
\psi &= qT - \alpha ,
\end{aligned}
\tag{4.44}
$$

where we've chosen the phase of ψ so that $\psi(T = 0) = -\alpha$.

So the system (4.37) becomes

$$
\begin{aligned}
a\dot{\psi} &= -\frac{1}{2} \langle \cos(\phi_i + \alpha) \rangle , \\
\dot{a} &= \frac{1}{2} \langle \sin(\phi_i + \alpha) \rangle - ba, \\
\dot{\phi_i} &= \omega_i - q - a\sin(\phi_i), \qquad i = 1 \ldots N .
\end{aligned}
\tag{4.45}
$$

4.9.2   Stationary State

If the system is at a stationary state, then the (nonzero) dimensionless amplitude must be fixed, i.e., $\dot{a} = 0$. We've already decided that q will be the frequency of the bridge and of the locked oscillators, so the first two equations of the system (4.45) become:

$$\begin{aligned} -\frac{1}{2} \langle \cos(\phi_i + \alpha) \rangle &= qa, \\ \frac{1}{2} \langle \sin(\phi_i + \alpha) \rangle &= ba \ . \end{aligned} \tag{4.46}$$

The third equation from (4.45) will be different for the two groups of oscillators: drifting and locked.

- **Locked group**: This group is frequency-locked with each other and with the bridge, and thus has $\dot{\phi}_i = 0$ (i.e., $\dot{\theta}_i = q$). It is composed of walkers whose native frequencies are fairly close to the resonant frequency of the bridge. The exact condition for this group is $|\omega_i - q| \leq a$, so that the third equation of (4.45) can be satisfied with $\dot{\phi}_i = 0$. In dimensional variables, this corresponds to the requirement that $|\Omega_i - \Omega_0| \leq AC$.

- **Drifting group**: This group cannot frequency-lock because the walkers that compose it have natural frequencies too far from that of the bridge. Instead, these walkers gradually drift relative to the locked pack, but still spend a majority of time near the pack in phase space (see Figure 4.5). The drift rate is given by the last equation in (4.45). These oscillators have $|\omega_i - q| > a$ (i.e., $|\Omega_i - \Omega_0| > AC$).

  Although this drifting group never approaches a fixed point, the oscillators can reach a statistical steady state by distributing themselves in a stationary
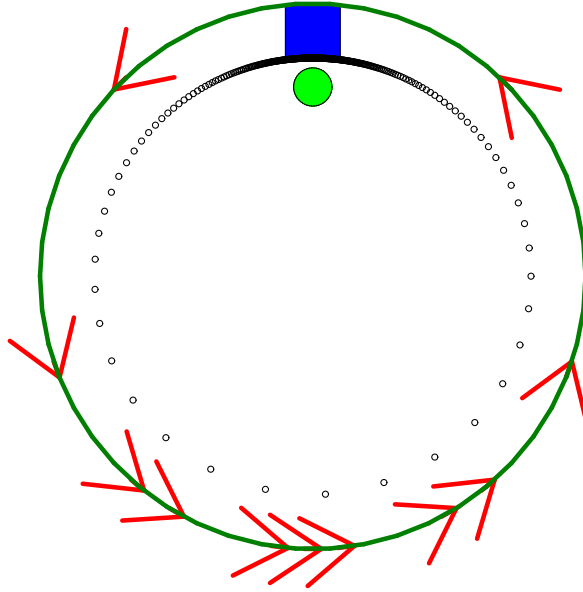
Figure 4.5: A sketch of the positions of drifting oscillators in phase space. The blue square indicates the position of the "barely locked" group of oscillators. Black dots indicate individual drifting oscillators, and arrows indicate speed of movement around the unit circle in phase space, with the highest speed occurring when the oscillators are 180 degrees away from the locked clump. The green circle is the centroid of the distribution of drifting oscillators, regarded as points in the complex plane.

distribution. To fully understand that case, we need to make an assumption that $N \gg 1$, so that a continuum limit is possible (this assumption was already implicit in the claim that the incoherent state exists and is stationary.)

4.9.3 Continuum Limit

We make the assumption that $N \gg 1$, so we'll move to a continuum limit for (4.45). In that limit, it becomes

$$
\begin{aligned}
a\dot{\psi} &= -\frac{1}{2} \int_{-\infty}^{\infty} \left[\oint \cos(\phi + \alpha)\rho(\phi; \omega)d\phi \right] g(\omega)d\omega, \\
\dot{a} &= \frac{1}{2} \int_{-\infty}^{\infty} \left[\oint \sin(\phi + \alpha)\rho(\phi; \omega)d\phi \right] g(\omega)d\omega - ba, \\
\dot{\phi} &= \omega - q - a\sin(\phi) \ ,
\end{aligned} \tag{4.47}
$$

where we now imagine a continuous density of oscillators around a unit circle in phase space. Given a value for the detuning ω, the probability of finding an oscillator with phase between $\phi - \frac{1}{2}d\phi$ and $\phi + \frac{1}{2}d\phi$ is $\rho(\phi; \omega)d\phi$. The distribution of detunings in the population is determined by $g(\omega)$.

Notation

To simplify the following work, we'll reuse the angle-bracket notation $\langle \cdot \rangle$ to indicate the mean value over the population. It will be the continuum analogue of the previously used definition (4.10):

$$
\langle Y(\phi; \omega) \rangle = \int_{-\infty}^{\infty} \oint Y(\phi; \omega)\rho(\phi; \omega)d\phi g(\omega)d\omega \ , \tag{4.48}
$$

where Y is any function of ϕ parameterized by ω.

4.9.4 Finding $\rho(\phi; \omega)$

To find the density of oscillators $\rho(\phi; \omega)$, consider the continuity equation for compressible flow

$$
\frac{\partial \rho}{\partial T} + \nabla \cdot (\rho \boldsymbol{v}) = 0 \ , \tag{4.49}
$$

where $\boldsymbol{v}$ represents the velocity field of the flow. In our one dimensional system of phase oscillators, the velocity is simply $\dot{\phi}$, and (4.49) reduces to

$$\frac{\partial \rho}{\partial T} + \frac{\partial}{\partial \phi}(\rho \dot{\phi}) = 0 \; . \tag{4.50}$$

We are looking for solutions where the oscillators are distributed in a statistical steady state, so we must impose

$$\frac{\partial \rho}{\partial T} = 0 \; ,$$

which implies that

$$\frac{\partial}{\partial \phi}(\rho \dot{\phi}) = 0 \; , \tag{4.51}$$

i.e.,

$$\rho \dot{\phi} = \text{constant} \; . \tag{4.52}$$

The constant is independent of ϕ but may be a function of ω.

Thus, the density ρ can be determined from the third equation of (4.47), along with (4.52) and a normalization condition. So

$$\rho(\phi; \omega) \propto \frac{1}{\omega - q - a\sin(\phi)} \; , \tag{4.53}$$

and the constant of proportionality can be determined by the normalization condition

$$\oint \rho(\phi; \omega) d\phi = 1 \; . \tag{4.54}$$

The necessary integral has the value

$$\oint \frac{1}{\omega - q - a\sin(\phi)} d\phi = \frac{2\pi}{\sqrt{(\omega - q)^2 - a^2}} \text{sign}\,(\omega - q) \; , \tag{4.55}$$

where it has been assumed that $|\omega - q| > a$. Thus, for drifting oscillators,

$$\rho_{\text{drift}}(\phi; \omega) = \frac{1}{2\pi} \frac{\sqrt{(\omega - q)^2 - a^2}}{|\omega - q - a\sin(\phi)|} \; , \tag{4.56}$$
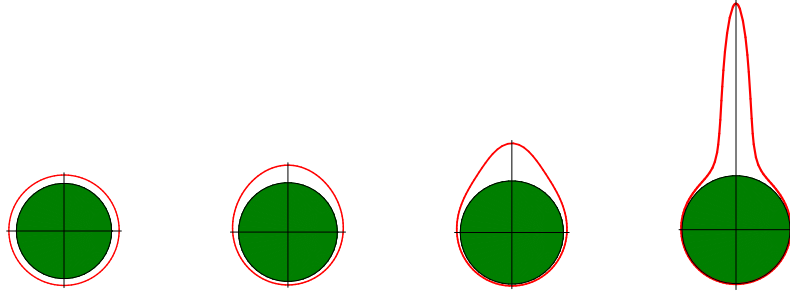
Figure 4.6: Typical examples of the probability distribution of drifting oscillators $\rho(\phi)$, as $\omega - q$ gets closer in magnitude to a (see equation (4.56)). Here we use $\omega - q$=10, 1.5, 1.1, 1.005, with $a = 1$. Probability is plotted in polar coordinates, with radial distance measured from the unit circle rather than the origin.

a function with even symmetry about $\phi = \pm\pi/2$.

For the locked oscillators, the density $\rho(\phi; \omega)$ will be a Dirac delta function, with all individuals locked at the phase ϕ^* determined by setting $\dot{\phi} = 0$ in (4.47) and choosing the stable fixed point:

$$\phi^* = \arcsin(\frac{\omega - q}{a}) \ . \tag{4.57}$$

We have chosen the root corresponding to the *stable* fixed point of (4.47), since that's where locked oscillators will settle.

Thus the density ρ is given by the following piecewise function:

$$\rho(\phi; \omega) = \begin{cases} \dfrac{1}{2\pi} \dfrac{\sqrt{(\omega - q)^2 - a^2}}{|\omega - q - a\sin(\phi)|} & |\omega - q| > a \\ \delta\left(\phi - \arcsin\left(\dfrac{\omega - q}{a}\right)\right) & |\omega - q| \leq a \end{cases} \tag{4.58}$$

4.9.5 Self-Consistency Equations

Having determined the density ρ, we are now ready to evaluate the averages that appear in the two equations, (4.46). The trig functions can be expanded to get

$$2qa = -\langle\cos(\phi + \alpha)\rangle = \sin\alpha\,\langle\sin\phi\rangle - \cos\alpha\,\langle\cos\phi\rangle,$$

$$2ba = \langle\sin(\phi + \alpha)\rangle = \cos\alpha\,\langle\sin\phi\rangle + \sin\alpha\,\langle\cos\phi\rangle \ . \tag{4.59}$$

Evaluating $\langle \sin \phi \rangle$ **and** $\langle \cos \phi \rangle$

The values of the population averages $\langle \sin \phi \rangle$ and $\langle \cos \phi \rangle$ may be calculated using (4.48) as

$$\langle \sin \phi \rangle = \int_{-\infty}^{\infty} \oint \sin \phi \rho(\phi; \omega) d\phi g(\omega) d\omega,$$

$$\langle \cos \phi \rangle = \int_{-\infty}^{\infty} \oint \cos \phi \rho(\phi; \omega) d\phi g(\omega) d\omega . \tag{4.60}$$

Inserting the expression for ρ from (4.58) splits the ω integral into two domains:

$$\langle \sin \phi \rangle = \int_{|\omega-q|\leq a} \sin \phi^* g(\omega) d\omega + \int_{|\omega-q|>a} \oint \sin \phi \, \tfrac{1}{2\pi} \tfrac{\sqrt{(\omega-q)^2 - a^2}}{|\omega-q-a\sin(\phi)|} \, d\phi g(\omega) d\omega,$$

$$\langle \cos \phi \rangle = \int_{|\omega-q|\leq a} \cos \phi^* g(\omega) d\omega + \int_{|\omega-q|>a} \oint \cos \phi \, \tfrac{1}{2\pi} \tfrac{\sqrt{(\omega-q)^2 - a^2}}{|\omega-q-a\sin(\phi)|} \, d\phi g(\omega) d\omega ,$$

$$\tag{4.61}$$

where the integral of the delta function for $|\omega - q| \leq a$ has been evaluated.

The values for $\sin \phi^*$ and $\cos \phi^*$ implied by (4.57) are:

$$\sin \phi^* = \frac{\omega - q}{a},$$

$$\cos \phi^* = \frac{\sqrt{a^2 - (\omega - q)^2}}{a} .$$

Here the positive root has been taken in the cosine expression for stability of the fixed point in (4.47).

To evaluate the integrals with respect to ϕ in (4.61), note the following:

$$\oint \frac{\sin \phi}{|\omega - q - a \sin \phi|} d\phi = \frac{2\pi}{a} \left[\frac{\omega - q}{\sqrt{(\omega - q)^2 - a^2}} - \operatorname{sign}(\omega - q) \right], \tag{4.62}$$

$$\oint \frac{\cos \phi}{|\omega - q - a \sin \phi|} d\phi = 0 . \tag{4.63}$$

It's clear that the cosine expression must integrate to zero because the integrand is odd about $\phi = \pi/2$, and the domain of integration can be taken as symmetric about that point.

Using the above in (4.61) yields

$$\langle \sin \phi \rangle = \int\limits_{|\omega-q| \leq a} \frac{\omega - q}{a} g(\omega) d\omega \tag{4.64}$$

$$+ \int\limits_{|\omega-q| > a} \left[(\omega - q) - \sqrt{(\omega - q)^2 - a^2} \text{sign} \, (\omega - q) \right] \frac{g(\omega)}{a} d\omega,$$

$$\langle \cos \phi \rangle = \int\limits_{|\omega-q| \leq a} \sqrt{a^2 - (\omega - q)^2} \frac{g(\omega)}{a} d\omega \; . \tag{4.65}$$

These expressions, inserted into the two equations (4.59), form a self-consistent algebraic system whose solutions determine the two unknowns a and q. These determine the steady-state amplitude of vibration $A = aL$ and the frequency of the oscillating bridge $\Omega = \Omega_0(1 + \epsilon q)$ for a given set of bridge parameters and a given number of walkers.

4.9.6 Threshold for Onset of Wobbling

We can find simplified self-consistency equations for the case where the bridge is near the threshold b_c. For dimensionless damping $b \geq b_c$, there is no bridge movement, but for $b < b_c$ the damping is insufficient and the wobble begins. That threshold can be found by examining the behavior of (4.64) and (4.65) for small a.

Starting with (4.64), we'll write the Taylor expansion about $\omega = q$ for the integrand of the first integral (valid since $a \ll 1$ and $|\omega - q| \leq a$ in that integral), and we'll Taylor expand the square root about $a = 0$ in the second integral,

retaining terms up to order a^2 for intermediate steps:

$$\langle \sin \phi \rangle \approx \int_{q-a}^{q+a} \left[\frac{g(q)}{a}(\omega - q) + \frac{g'(q)}{a}(\omega - q)^2 + \mathcal{O}\left((\omega - q)^3\right) \right] d\omega$$

$$+ \int_{|\omega - q| > a} \left[(\omega - q) - |\omega - q| \left(1 - \frac{a^2}{2(\omega - q)^2} \right) \text{sign} \, (\omega - q) \right] \frac{g(\omega)}{a} d\omega \ . \quad (4.66)$$

Evaluating the first integral and simplifying the integrand of the second,

$$\langle \sin \phi \rangle \approx \left[\frac{g(q)}{a} \left(\frac{1}{2}\omega^2 - q\omega \right) + \frac{g'(q)}{3a}(\omega - q)^3 + \mathcal{O}\left((\omega - q)^4\right) \right]_{\omega = q - a}^{\omega = q + a}$$

$$+ \lim_{a \to 0^+} \int_{|\omega - q| > a} \left[\frac{a^2}{2(\omega - q)} \right] \frac{g(\omega)}{a} d\omega \ , \quad (4.67)$$

thus

$$\langle \sin \phi \rangle \approx \frac{2}{3}g'(q)a^2 + \frac{a}{2}PV \int_{-\infty}^{\infty} \frac{g(\omega)}{\omega - q} d\omega \ .$$

But for small a, only the leading order term will be retained, so

$$\langle \sin \phi \rangle \approx \frac{a}{2}PV \int_{-\infty}^{\infty} \frac{g(\omega)}{\omega - q_0} d\omega \ . \quad (4.68)$$

Here q_0 denotes the value of q near the threshold, when $a \to 0^+$. The "PV" preceding the integral indicates that the Cauchy principal value is to be taken, defined by the limit shown above in (4.67). But that Cauchy principal value integral is exactly the definition of the Hilbert transform, scaled by π! So we can write

$$\langle \sin \phi \rangle \approx \frac{\pi}{2} a \tilde{g}(q_0) \ , \quad (4.69)$$

where $\tilde{g}(q_0) = \mathcal{H}\left[g(\omega)\right]$ represents the Hilbert transform of g evaluated at q_0.

Repeating a similar process for the cosine equation (4.65):

$$\langle \cos \phi \rangle = \int_{|\omega - q| \leq a} \sqrt{1 - \frac{(\omega - q)^2}{a^2}} g(\omega) d\omega \ . \quad (4.70)$$

Next, change variables in order to make the small a behavior of this integral easier to evaluate. Using $\omega = q + a \sin \phi$ for the locked oscillators (from (4.57)), we find

$$\langle \cos \phi \rangle = \int_{-\pi/2}^{\pi/2} a \cos^2 \phi \, g(q + a \sin \phi) d\phi \ . \tag{4.71}$$

Thus to leading order in a, the integral's value is

$$\langle \cos \phi \rangle \approx \frac{\pi}{2} a g(q_0) \ , \tag{4.72}$$

since $\oint \cos^2 \phi d\phi = \pi$.

Finally, insert the expressions from (4.72) and (4.69) into the system (4.59):

$$2q_0 a = \frac{\pi}{2} \sin \alpha a \tilde{g}(q_0) - \frac{\pi}{2} \cos \alpha a g(q_0),$$
$$2b_c a = \frac{\pi}{2} \cos \alpha a \tilde{g}(q_0) + \frac{\pi}{2} \sin \alpha a g(q_0) \ , \tag{4.73}$$

Cancelling the common factor of a (which we expected since the incoherent state $a = 0$ exists for all parameter values), we find the threshold conditions for onset of bridge motion ($a \neq 0$):

$$
\begin{aligned}
q_0 &= \frac{\pi}{4} \left(\tilde{g}(q_0) \sin \alpha - g(q_0) \cos \alpha \right) , \\
b_c &= \frac{\pi}{4} \left(\tilde{g}(q_0) \cos \alpha + g(q_0) \sin \alpha \right) \ .
\end{aligned}
\tag{4.74}
$$

The two equations determine two important properties of the bridge at threshold: through q_0, the frequency of the combined bridge-crowd system ($\Omega = \Omega_0 (1 + \epsilon q)$), and, through b_c, the critical number of walkers to destabilize the bridge ($N_c = \zeta^2 K \Omega_0 G^{-1} C^{-1} b_c^{-2}$). Figures 4.7, 4.8, and 4.9 graphically show various solutions q_0 to the first equation of (4.74), with a Lorentzian distribution for $g(\omega)$:

$$g(\omega) = \frac{1}{\pi} \frac{\Gamma/2}{(\omega - \overline{\omega})^2 + (\Gamma/2)^2} \ .$$
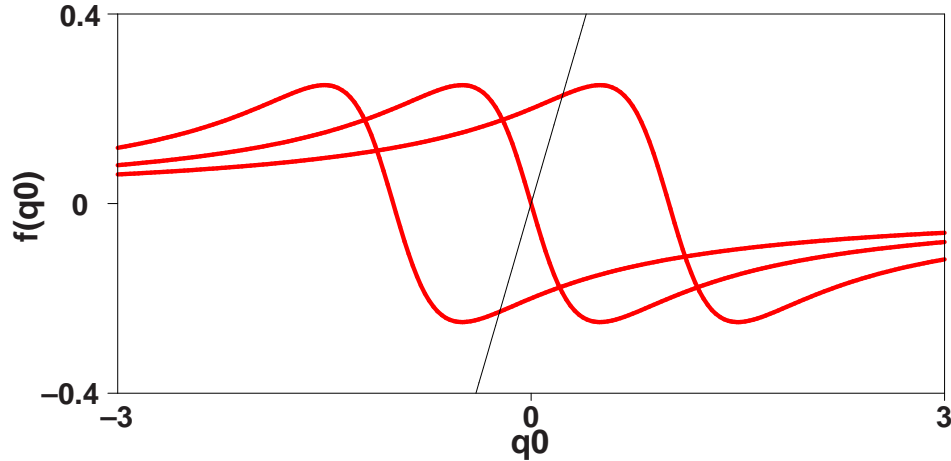
Figure 4.7: **Detuning Varies**: The right hand side of the first equation (4.74) is plotted along with the line $f(q_0) = q_0$ for a Lorentzian $g(\omega)$ with three different values of the detuning $\overline{\omega}$: -1, 0, and 1 (rightmost). For each curve, $\Gamma = 1$ and $\alpha = \pi/2$.

Figures 4.10, 4.11, 4.12, 4.13, 4.14, and 4.15 show the critical threshold b_c as a function of various parameters for a Lorentzian $g(\omega)$. Note that in some cases, there are multiple solutions for q_0. This implies the existence of several wobbling states for the bridge, which could lead to hysteresis or other interesting phenomena.

There is one caveat: even though these equations determine the critical threshold b_c (or N_c) at which the partially locked state comes into existence, they say nothing about the stability of either the partially locked or incoherent states.

4.9.7 Special Cases

In the following subsections, several special cases of the general self-consistency equations will be considered.

The Special Case $\alpha = \pi/2$

The equations (4.74) become especially simple in the case $\alpha = \pi/2$. This case is of interest because empirical and computational evidence suggests that $\alpha =$
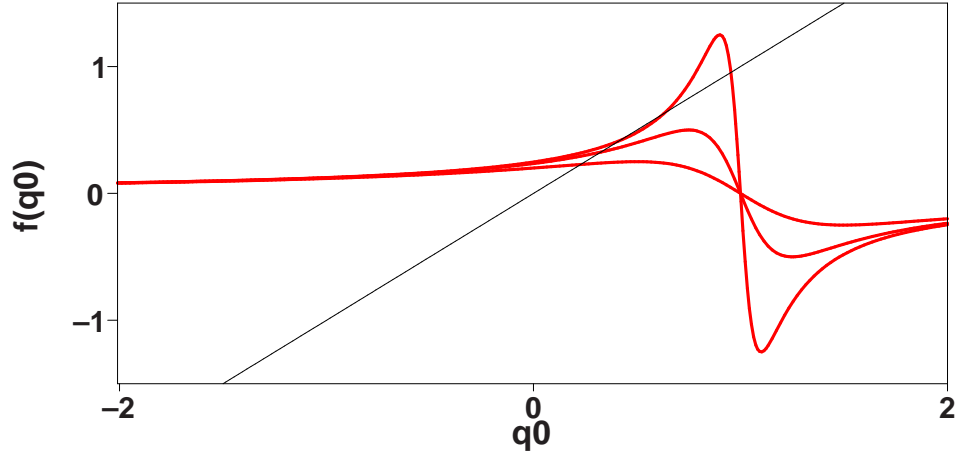
Figure 4.8: **Distribution Width Varies**: The right hand side of the first equation (4.74) is plotted along with the line $f(q_0) = q_0$ for a Lorentzian $g(\omega)$ with three different values of the full-width Γ: 0.2 (highest), 0.5, and 1. For each curve, $\overline{\omega} = 1$ and $\alpha = \pi/2$.

$\pi/2$ is close to the correct value for human response to lateral vibrations. It's also the worst-case scenario, in which the bridge is maximally destabilized, so the resulting prediction of the critical number of walkers is conservative. However, an experiment to test this evidence would be very welcome.

$$
\begin{aligned}
q_0 &= \frac{\pi}{4}\tilde{g}(q_0), \\
b_c &= \frac{\pi}{4}g(q_0) .
\end{aligned}
\tag{4.75}
$$

Even Symmetric Distribution $g(\omega)$ With No Detuning If we further assume a function $g(\omega)$ with even symmetry—i.e., a symmetric pedestrian frequency distribution centered on the bridge frequency—then we can easily solve the system (4.75). In that case, $q_0 = 0$ is always a solution to the first equation, which can be seen by writing out the Hilbert transform with $q = 0$:

$$
q_0 = 0 = \frac{1}{4}PV \int_{-\infty}^{\infty} \frac{g(\omega)}{\omega} .
\tag{4.76}
$$
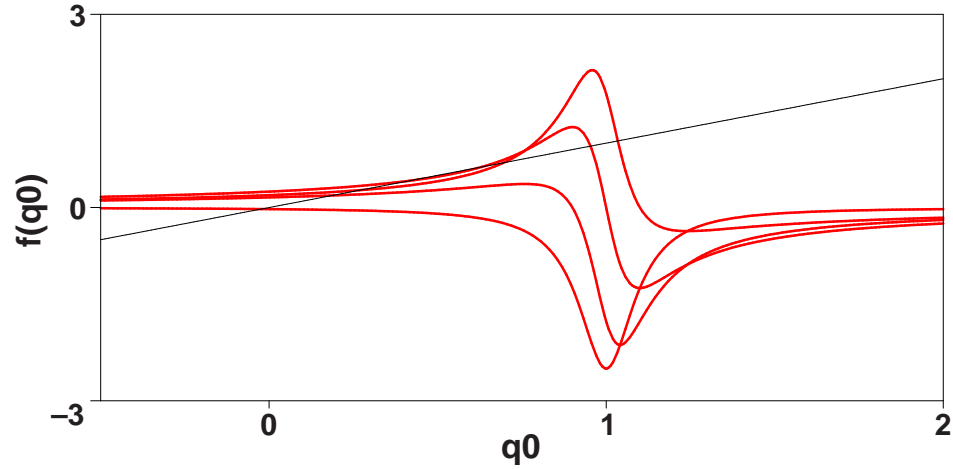
Figure 4.9: **Lag Varies**: The right hand side of the first equation (4.74) is plotted along with the line $f(q_0) = q_0$ for a Lorentzian $g(\omega)$ with four different values of α: 0, $\pi/4$, $\pi/2$, and $3\pi/4$ (highest). For each curve, $\overline{\omega} = 1$ and $\Gamma = 0.2$.

The integrand is odd, and it is integrated over a symmetric domain, so its Cauchy principal value is zero.

It can be shown that $q_0 = 0$ is the only solution to (4.75) for any even Lorentzian function $g(\omega)$. It's hypothesized that this is the case for any singly peaked C^∞ function $g(\omega)$. In this case, the partially locked state is unique.
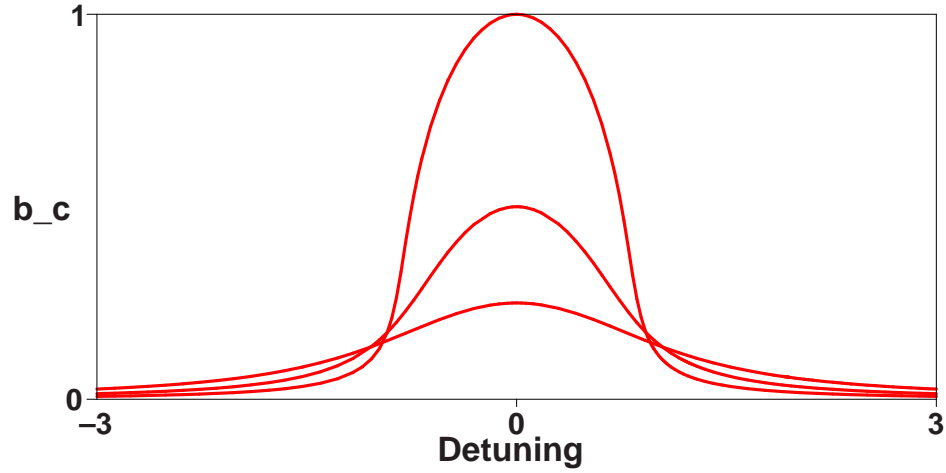
Figure 4.10: **Detuning Varies**: The right hand side of the second equation (4.74) is plotted versus the detuning $\overline{\omega}$ for a Lorentzian $g(\omega)$ with three different values of Γ: 0.5, 1, and 2 (lowest). For each curve, $\alpha = \pi/2$. $b_c \approx 1/(2\Gamma) - 2\overline{\omega}^2\Gamma/(\Gamma^2+1)^2$ for small detunings with $\alpha = \pi/2$.

A quick demonstration of uniqueness for Lorentzian $g(\omega)$.

For a Lorentzian with no detuning, the Hilbert transform is

$$\mathcal{H}\left[\frac{1}{\pi}\frac{\Gamma/2}{(\Gamma/2)^2 + \omega^2}\right] = -\frac{1}{\pi}\frac{q_0}{(\Gamma/2)^2 + q_0^2} \ .$$

So the equation (4.75) becomes

$$q_0 = -\frac{1}{4}\frac{q_0}{(\Gamma/2)^2 + q_0^2} \ .$$

If $q_0 \neq 0$, then we get

$$q_0^2 + (\Gamma/2)^2 = -\frac{1}{4} \ .$$

But the entire left hand side must be positive for any real q_0 and Γ, so this equation cannot be satisfied. Hence, $q_0 = 0$ is the unique solution.

Under the above assumptions the second equation of (4.75) gives

$$\boxed{b_c = \frac{\pi}{4}g(0) \ .} \tag{4.77}$$
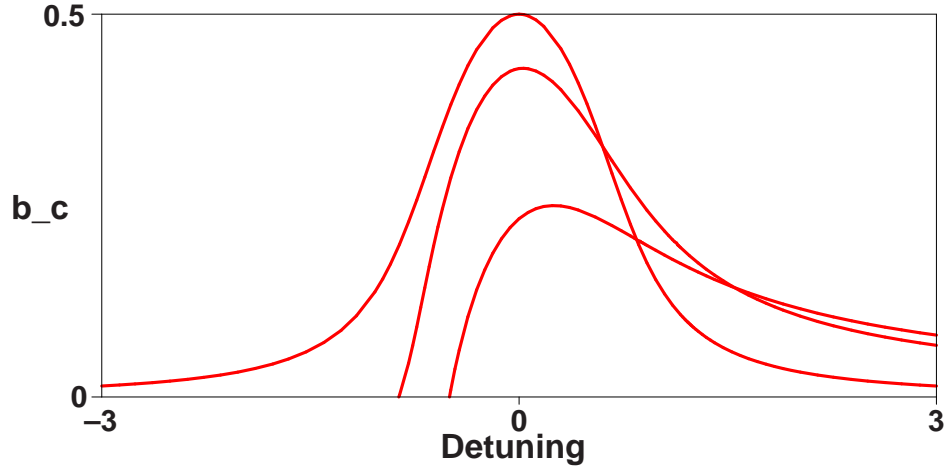
Figure 4.11: **Detuning Varies**: The right hand side of the second equation (4.74) is plotted versus the detuning $\overline{\omega}$ for a Lorentzian $g(\omega)$ with three different values of α: 0, $\pi/4$, and $\pi/2$ (leftmost). For each curve, $\Gamma = 1$. $b_c \approx 1/(2\Gamma) - 2\overline{\omega}^2\Gamma/(\Gamma^2+1)^2$ for small detunings with $\alpha = \pi/2$.

The $g(0)$ in this expression can be related to the probability distribution function for oscillators in the dimensional variables $P(\Omega)$ by using (4.13), extended to the continuum limit:

$$\frac{\Omega}{\Omega_0} = 1 + \epsilon\omega \ ,$$

$$d\Omega = \epsilon\Omega_0 d\omega \ .$$

So

$$g(\omega = 0)d\omega \ = \ P(\Omega = \Omega_0)d\Omega,$$

$$g(0) \ = \ \epsilon\Omega_0 P(\Omega_0) \ . \tag{4.78}$$
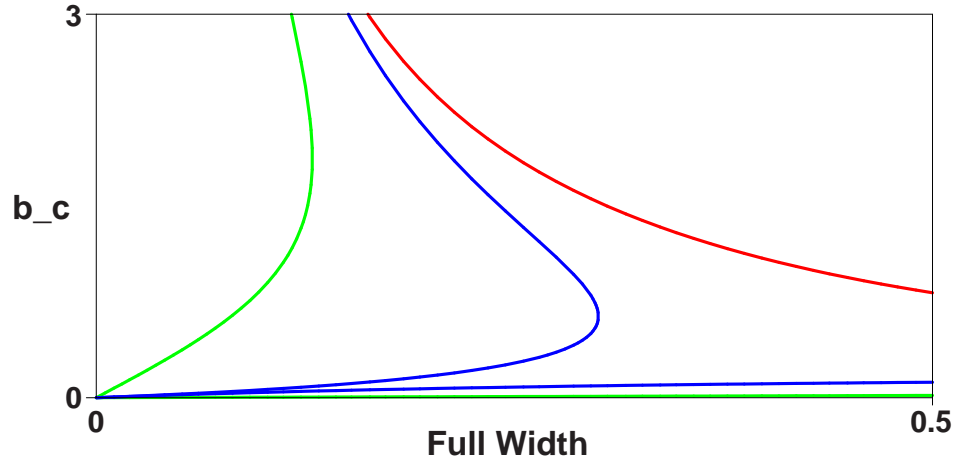
Figure 4.12: **Distribution Width Varies**: The right hand side of the second equation (4.74) is plotted versus the full-width Γ for a Lorentzian $g(\omega)$ with three different values of $\overline{\omega}$: 2, 1, and 0.5 (rightmost). For each curve, $\alpha = \pi/2$. $b_c = 1/(2\Gamma)$ when $\overline{\omega} = 0$ with $\alpha = \pi/2$.

Thus in dimensional variables, (4.77) becomes

$$
\begin{aligned}
b_c &= \frac{\pi}{4}(\epsilon \Omega_0 P(\Omega_0)), \\
\zeta_c &= \frac{\pi}{4}\epsilon^2 \Omega_0 P(\Omega_0), \\
\zeta &= \frac{\pi}{4}N_c GCP(\Omega_0)/K, \\
N_c &= \frac{4\zeta K}{\pi GCP(\Omega_0)}, \\
N_c &= \boxed{\frac{2B\Omega_0}{\pi GCP(\Omega_0)}},
\end{aligned}
\tag{4.79}
$$

where we've made use of (4.12) and (4.8).

The Special Case $\alpha = 0$

Alternatively, if we take $\alpha = 0$ in the system (4.74), it reduces to

$$
\begin{aligned}
q_0 &= -\frac{\pi}{4}g(q_0), \\
b_c &= \frac{\pi}{4}\tilde{g}(q_0) \, .
\end{aligned}
\tag{4.80}
$$
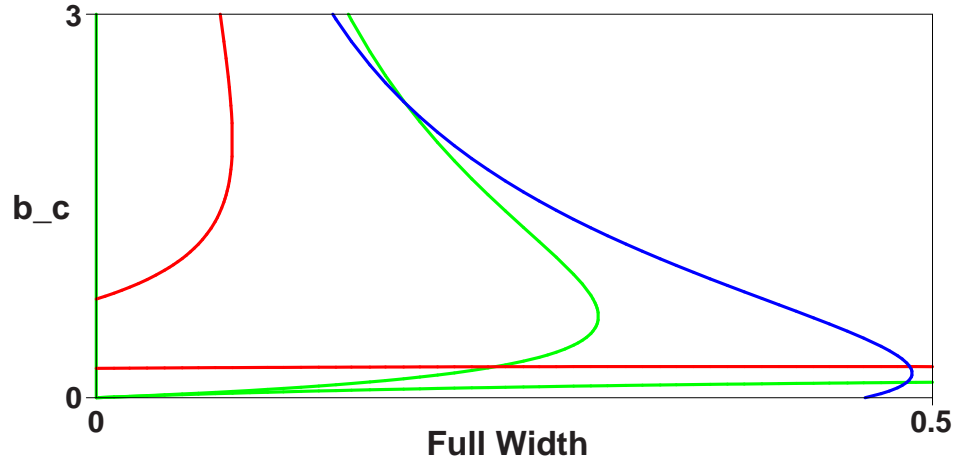
Figure 4.13: **Distribution Width Varies**: The right hand side of the second equation (4.74) is plotted versus the full-width Γ for a Lorentzian $g(\omega)$ with three different values of α: $\pi/4$, $\pi/2$, and $3\pi/4$ (rightmost). For each curve, $\overline{\omega} = 1$. $b_c = 1/(2\Gamma)$ when $\overline{\omega} = 0$ with $\alpha = \pi/2$.

The Special Case $q = 0$

There is an entire class of solutions to the self-consistency equations for $q = 0$. The virtue of this special case is that we can study the partially synchronized state for arbitrary bridge amplitude a, not just the near-threshold limit $a \to 0^+$.

Seeking solutions with $q = 0$, we find that the equations (4.59) become

$$0 = \sin\alpha \langle \sin\phi \rangle - \cos\alpha \langle \cos\phi \rangle ,$$

$$2ba = \cos\alpha \langle \sin\phi \rangle + \sin\alpha \langle \cos\phi \rangle , \qquad (4.81)$$

and the expressions for the population averages (4.64) and (4.65) become

$$\langle \sin\phi \rangle = \int\limits_{|\omega| \leq a} \frac{\omega}{a} g(\omega) d\omega + \int\limits_{|\omega| > a} \left[\omega - \sqrt{\omega^2 - a^2} \mathrm{sign}\,(\omega) \right] \frac{g(\omega)}{a} d\omega, \qquad (4.82)$$

$$\langle \cos\phi \rangle = \int\limits_{|\omega| \leq a} \sqrt{a^2 - \omega^2} \frac{g(\omega)}{a} d\omega . \qquad (4.83)$$

Even Symmetric Distribution $g(\omega)$ **With No Detuning**   For the remainder of this section we'll assume that the distribution of walker frequencies $g(\omega)$ is
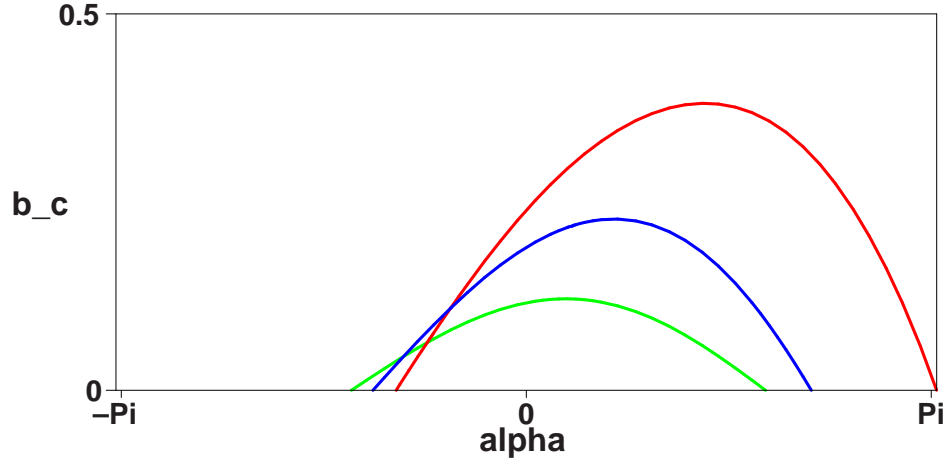
Figure 4.14: **Lag Varies**: The right hand side of the second equation (4.74) is plotted versus α for a Lorentzian $g(\omega)$ with three different values of $\overline{\omega}$: 2, 1, and 0.5 (rightmost). For each curve, $\Gamma = 1$. For $\Gamma = 1$ with small $\overline{\omega}$ and α near $\pi/2$, $8b_c \approx [4 - (\alpha - \pi/2)^2] - \overline{\omega}^2[4 - (\alpha - \pi/2)^2]$.

symmetric and even. This means that the mean walker frequency is $\Omega = \Omega_0$, so the bridge is being driven exactly on resonance, a worst-case scenario. The case where the mean walker frequency is detuned away from Ω_0 is considered elsewhere.

Under this assumption, both of the integrands of (4.82) will be odd functions, and the integration limits define even domains, so that we end up with $< \sin \phi >= 0$. The integrand of (4.83) will be even,

$$\langle \sin \phi \rangle = 0, \tag{4.84}$$

$$\langle \cos \phi \rangle = \frac{1}{a} \int_{-a}^{a} \sqrt{1 - (\omega/a)^2} g(\omega) d\omega . \tag{4.85}$$

Thus (4.81) becomes

$$0 = \cos \alpha \int_{-a}^{a} \sqrt{1 - (\omega/a)^2} g(\omega) d\omega,$$

$$2ba = \sin \alpha \int_{-a}^{a} \sqrt{1 - (\omega/a)^2} g(\omega) d\omega . \tag{4.86}$$

The integrals can be expressed in terms of ϕ by a change of variables using
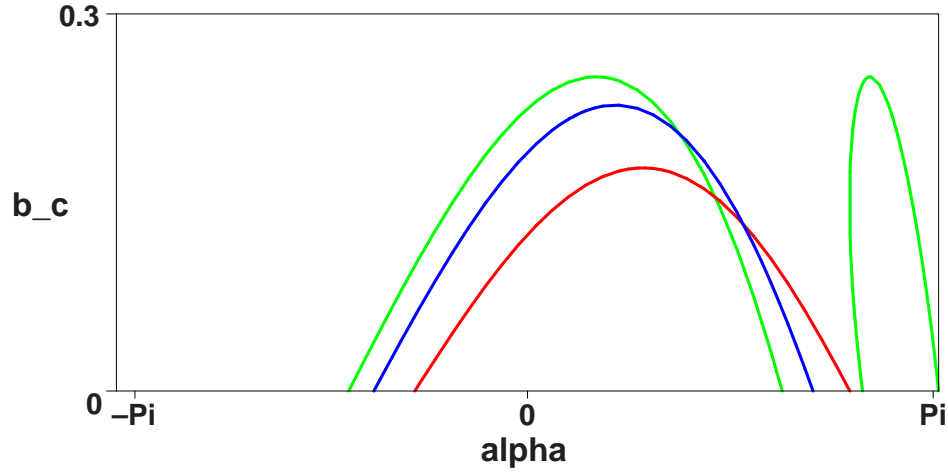
Figure 4.15: **Lag Varies**: The right hand side of the second equation (4.74) is plotted versus α for a Lorentzian $g(\omega)$ with three different values of full-width Γ: 2, 1, and 0.5 (leftmost). For each curve, $\overline{\omega} = 1$.

$\omega = a \sin \phi$:

$$\int_{-a}^{a} \sqrt{1 - (\omega/a)^2} g(\omega) d\omega = \int_{-\pi/2}^{\pi/2} \cos \phi g(a \sin \phi)(a \cos \phi d\phi) \ .$$

So

$$0 = a \cos \alpha \int_{-\pi/2}^{\pi/2} \cos^2 \phi g(a \sin \phi) d\phi,$$

$$2b = \sin \alpha \int_{-\pi/2}^{\pi/2} \cos^2 \phi g(a \sin \phi) d\phi \ . \tag{4.87}$$

Equation (4.87) requires that $\cos \alpha = 0$, since we've already assumed that a is nonzero in this partially locked state. So it turns out that the combination of assumptions (1) $g(\omega)$ even and (2) $q = 0$ requires that $\alpha = \pi/2$! We already looked into that special case at the beginning of Section 4.9.7, but we will do a bit more work on it here to see how the bridge amplitude a varies with other parameters.

Details of the exact solutions to Equation (4.87) in the special cases where $g(\omega)$

is a Lorentzian or Gaussian distribution will be presented below.

As a check, we can verify that the limit of Equation (4.87) for small a agrees with the expression derived above, (4.77), since both have $\alpha = \pi/2$.

$$
\begin{aligned}
\lim_{a \to 0}(2b) &= \lim_{a \to 0} \int_{-\pi/2}^{\pi/2} \cos^2 \theta g(a \sin \theta) d\theta, \\
b_c &= \frac{1}{2} \int_{-\pi/2}^{\pi/2} \cos^2 \theta g(0) d\theta , \\
b_c &= \frac{\pi}{4} g(0) ,
\end{aligned}
\tag{4.88}
$$

as expected.

Special case: Lorentzian distribution of pedestrian frequencies

Assume a Lorentzian distribution of walker frequencies,

$$
g(\omega) = \frac{1}{\pi} \frac{\Gamma/2}{\omega^2 + (\Gamma/2)^2} ,
\tag{4.89}
$$

where we are still operating under the earlier assumption that the mean walker frequency is on resonance (i.e., the mean detuning $\overline{\omega}$ is zero). With this form, the integral in equation (4.87) can be solved exactly:

$$
b = \frac{\sqrt{\Gamma^2 + 4a^2} - \Gamma}{4a^2} ,
\tag{4.90}
$$

or, solving for a,

$$
a = \frac{\sqrt{1 - 2b\Gamma}}{2b}
\tag{4.91}
$$

(see Figure 4.16).

This formula can be converted to dimensional units and solved to find the steady-state amplitude of bridge vibration as a function of the number of walkers,

$$
A^2 = \frac{NG}{CB^2 \Omega_0^2} (NGC - B\Gamma \Omega_0) .
\tag{4.92}
$$
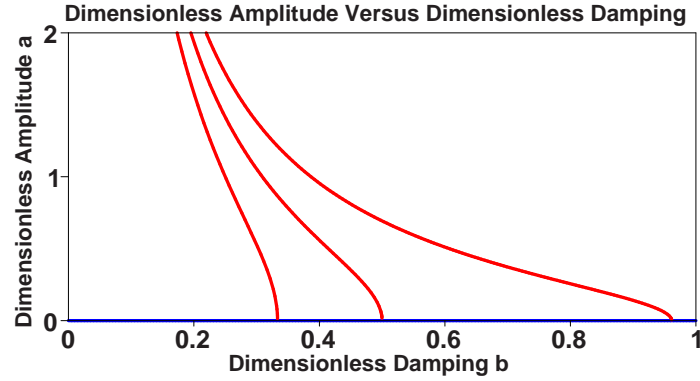
Figure 4.16: Three examples from the family of curves $a(b)$ described by equation (4.91), showing the dimensionless amplitude of vibration a versus the dimensionless damping b, when $g(\omega)$ is an even Lorentzian distribution. From left to right, the values of Γ used in each curve are 1.5, 1, and 0.52.

Taking the limit as $A \to 0$, we find

$$N_c = \frac{\Gamma B \Omega_0}{GC} \; .$$
(4.93)

Because this closed-form solution is possible, we can easily write down the asymptotic solutions for N near N_c and $N \to \infty$. These asymptotic solutions may also apply for other native frequency distributions with heavy tails, similar to the Lorentzian distribution.

For N close to the critical value N_c, we find that

$$A^2 \approx \frac{G\Gamma}{CB\Omega_0}(N - N_c)$$
(4.94)

to lowest order in $N - N_c$.

In the limit $N \to \infty$, we find

$$A \approx \frac{G}{B\Omega_0} N \; .$$
(4.95)

Figure 4.17 plots equations (4.92), (4.94), and (4.95), using parameter values relevant to the north span of the Millennium bridge.
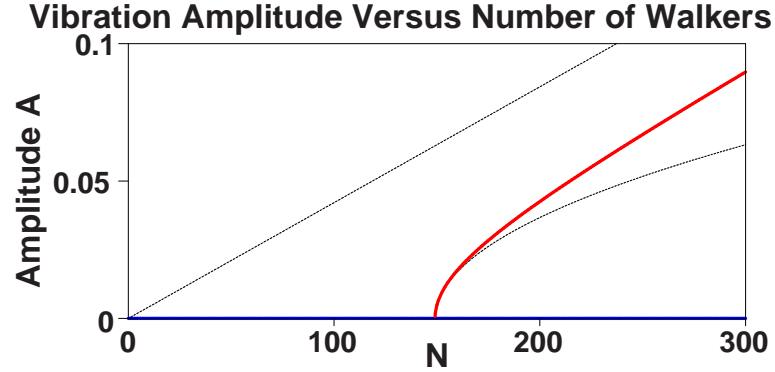
Figure 4.17: A curve $A(N)$ from equation (4.92). It shows the predicted amplitude of vibration A in meters versus the number of pedestrians N, assuming a Lorentzian distribution of walker frequencies $P(\Omega)$ with parameters estimated for the north span of the Millennium Bridge (see Section 2.5). Γ was taken to be 1 rad/s (0.16 Hz). G was taken to be a constant 30 Newtons, and C was taken as $16 m^{-1} s^{-1}$. The upper dotted line is the approximation for $N \to \infty$, while the lower dotted line is the first order approximation for N near N_c.

The value of G used in simulations was 30 Newtons, which corresponds to the forcing of a person of average mass on an unmoving surface. In [16], McRobie et al show that the magnitude of that forcing can increase by almost an order of magnitude when the pedestrian is on a laterally moving surface, and is forced to adopt a different gait (reminiscent of the way a penguin walks). Note that both that effect, and the possible detuning of a slow-moving crowd have not been included in this calculation. The predicted amplitude of the bridge motion is still very close to the observed value of about 7cm on opening day.

Special case: Gaussian distribution of pedestrian frequencies

Assume a Gaussian distribution of walker frequencies,

$$g(\omega) = \frac{1}{\sigma\sqrt{2\pi}} e^{-\omega^2/(2\sigma^2)} \; , \tag{4.96}$$

where we are still operating under the earlier assumption that the mean walker frequency is on resonance (i.e., the mean detuning $\overline{\omega}$ is zero). With this form, the
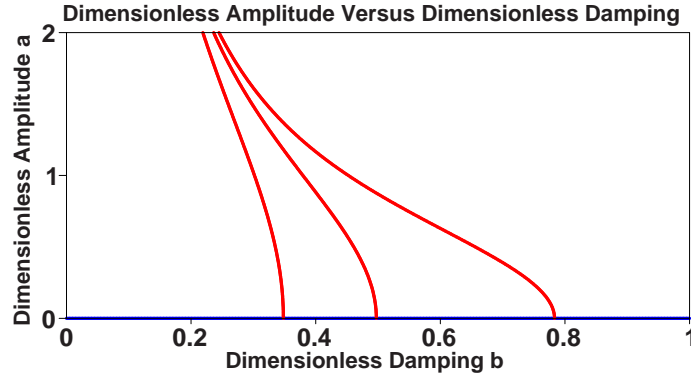
Figure 4.18: Three example from the family of curves $a(b)$ described by equation (4.97), showing the dimensionless amplitude of vibration a versus the dimensionless damping b, when $g(\omega)$ is an even Gaussian distribution. From left to right, the values of σ used in each curve are 0.9, 0.63, and 0.4.

integral in equation (4.87) can be solved exactly:

$$b = \frac{\sqrt{2\pi}}{8\sigma} e^{-a^2/(4\sigma^2)} \left[I_0 \left(\frac{a^2}{4\sigma^2} \right) + I_1 \left(\frac{a^2}{4\sigma^2} \right) \right] , \tag{4.97}$$

where $I_0(x)$ and $I_1(x)$ are modified Bessel functions of the first kind. The implicit function $a(b)$ is plotted for several values of σ in Figure 4.18.

This formula can be converted to dimensional units to get an implicit function for $A(N)$,

$$B = \frac{\sqrt{2\pi}NGC}{4\sigma\Omega_0} e^{-\frac{A^2C^2}{4\sigma^2}} \left[I_0 \left(\frac{A^2C^2}{4\sigma^2} \right) + I_1 \left(\frac{A^2C^2}{4\sigma^2} \right) \right] , \tag{4.98}$$

where σ now refers to the standard deviation of the distribution $P(\Omega)$ (note that $\sigma_\omega = \epsilon\Omega_0\sigma_\Omega$).

We take the limit as $A \to 0$, using the fact that $I_0(0) = 1$ and $I_1(0) = 0$, and solve for N to find

$$N_c = \frac{2\sqrt{2}}{\pi} \frac{B\Omega_0\sigma}{GC} . \tag{4.99}$$

We can also find asymptotic solutions for N near N_c and $N \to \infty$, using series expansions for the modified Bessel functions. The hope is that these asymptotic

solutions would also apply for other native frequency distributions with shapes similar to a Gaussian.

For N close to the critical value N_c, we find that

$$A^2 \approx 2\sqrt{2\pi}\frac{G\sigma}{CB\Omega_0}(N - N_c) \ . \tag{4.100}$$

to lowest order in $N - N_c$. Note the factor of $2\sqrt{2\pi}$ difference with (4.94). This large factor appears because Γ is the full width at half maximum for a Lorentzian, whereas σ is a single standard deviation, less than half the full-width for a Gaussian.

In the limit $N \to \infty$, we find

$$A \approx \frac{G}{B\Omega_0}N \ . \tag{4.101}$$

Figure 4.19 plots equations (4.98), (4.100), and (4.101), using parameter values relevant to the north span of the Millennium bridge.

As mentioned previously in the special case for a Lorentzian distribution, the value of G used in numerics was held constant at the value for normal walking. McRobie et al [16] show that the magnitude of that forcing can increase by almost an order of magnitude when the pedestrian is on a laterally moving surface, and is forced to adopt a different gait. Neither that effect nor the effect of detuning was included here, yet the predicted steady-state amplitudes are in good agreement with the values observed on opening day on the Millennium Bridge.

4.10   Examining the Effects of Various Parameters

This section is primarily composed of a series of figures that demonstrate the behavior of the important equations covered until this point. For each parameter
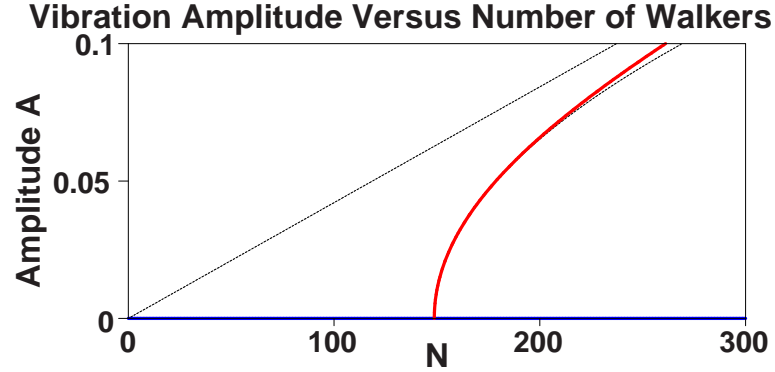
Figure 4.19: The implicit curve $A(N)$ from equation (4.98). It shows the predicted amplitude of vibration A in meters versus the number of pedestrians N, assuming a Gaussian distribution of walker frequencies $P(\Omega)$ with parameters estimated for the north span of the Millennium Bridge (see Section 2.5). σ was taken to be 0.63 rad/s (0.1 Hz). G was taken to be a constant 30 Newtons, and C was taken as $16m^{-1}s^{-1}$. The upper dotted line is the approximation for $N \to \infty$, while the lower black line is the first order approximation for N near N_c.

(Γ, α, and $\overline{\omega}$) we show two graphs, indicating how both b_c and its inverse b_c^{-1} vary with the parameter. The inverse graphs are useful because $b_c^{-1} \propto \sqrt{N}$, so it's easier to get an idea of how the critical number of pedestrians will vary with the parameter.

That said, please peruse the graphs starting from Figure 4.20 (page 67) through 4.26 (page 73).

The first two graphs—Figure 4.20 (page 67) and Figure 4.21 (Page 68)—compare numerical simulation to theory for b_c versus the half width of the pedestrian frequency distribution $\Gamma/2$ for two different values of α, when there is no detuning. Here the theoretical boundary for existence of the in-phase state agrees well with the numerical simulation, which finds the stability boundary starting from the incoherent state.

The next two graphs—Figure 4.22 (page 69) and Figure 4.23 (Page 70)—compare numerical simulation to theory for b_c versus the detuning of the pedestrian

frequency distribution $\overline{\omega}$ for two different values of α.

The green upper lines come from the stability analysis of the in-phase state (see section 5.3 and Figure 5.2), which was done *only* for the case of identical oscillators $\Gamma \to 0^+$. Therefore it's presented for comparison to the symmetric solid line, which should approach it as Γ decreases (see also Figure 4.10 if the stability boundary coincides with the existence boundary.

The thin red upper line on the right side of the b_c graph is the theoretical stability boundary when $\alpha = 0$, also presented for comparison (see section 5.3 and Figure 5.1). Please note though that the asymmetric existence boundary shown has $\alpha = \pi/4$ and nonzero Γ, so the comparison is not a direct one.

The next two graphs—Figure 4.24 (page 71) and Figure 4.25 (Page 72)—compare numerical simulation to theory for b_c versus the lag parameter α. The show good agreement between simulation and theory. There is a systematic bias in the numerics in favor of the incoherent state, because of the very long transient times associated with onset of vibration near threshold (see Section 4.11).

The final graph of this section—Figure 4.26 (page 73)—shows a stability boundary, *not* the boundary of existence of the in-phase state. It plots how b_{cs}^{-1} varies with lag α, as detuning is varied.

4.11 Time Scales

There are three time variables used in this analysis, namely, dimensional time t, dimensionless time τ, and slow time T. Recall the definitions from (4.7) and (4.17),

$$\tau = \Omega_0 t,$$

$$T = \epsilon\tau = \epsilon\Omega_0 t \ .$$
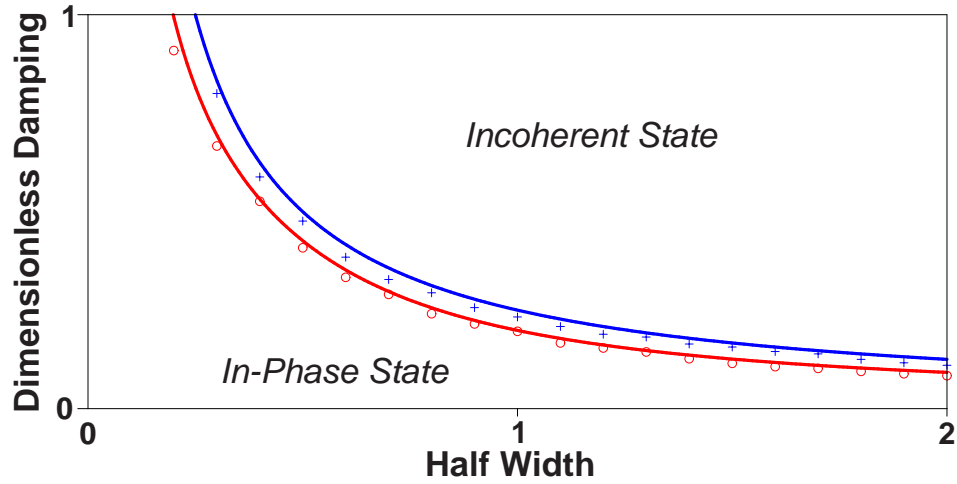
Figure 4.20: The behavior of b_c, the critical dimensionless damping, versus the half width of the Lorentzian distribution $g(\omega)$. Detuning $\overline{\omega} = 0$. Upper line (blue) is for $\alpha = \pi/2$, lower line (red) for $\alpha = \pi/4$. Points are results of numerical integration of the slow-time equations. Lines are theoretical predictions for the threshold of existence of the in-phase state, from the system (4.74). Upper line (blue) is $b = 1/(2\Gamma)$ (where Γ=FWHM).

The fast time scale is determined by the natural frequency of the bridge, that used to non-dimensionalize time above. Thus

$$t_{\text{fast}} = 2\pi/\Omega_0 \approx 1sec , \tag{4.102}$$

where the natural frequency for the north span fundamental mode has been used (see Section 2.5).

The slow time scale is determined by the interaction time between the bridge and the crowd, i.e., how long it takes the bridge to build up significant motion with a large crowd. For that reason, it will be a function of the number of pedestrians N. It's given by the dimensional version of the slow time variable T as

$$t_{\text{slow}} = \frac{2\pi}{\epsilon\Omega_0} \approx \frac{245}{\sqrt{N}}sec , \tag{4.103}$$

again using the parameters relevant to the north span fundamental mode. At the
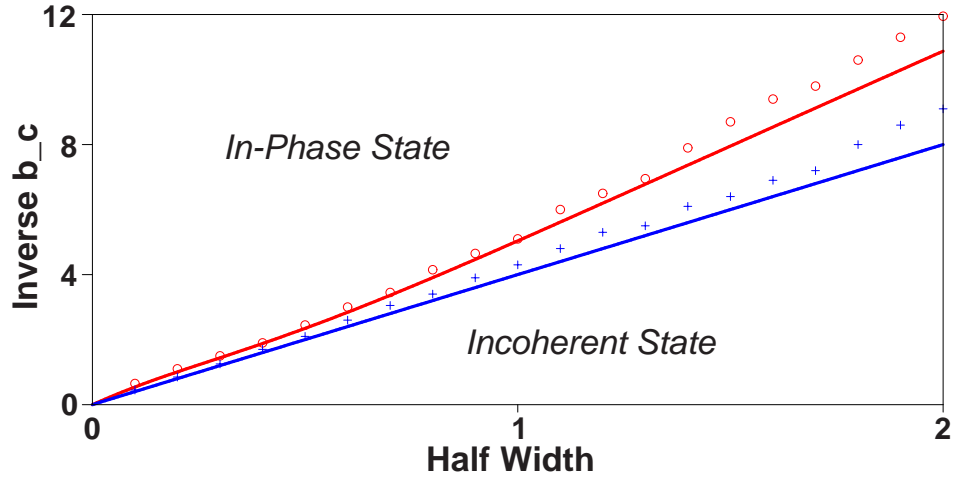
Figure 4.21: The behavior of b_c^{-1}, the inverse critical dimensionless damping, versus the half width of the Lorentzian distribution $g(\omega)$. Detuning $\overline{\omega} = 0$. Upper line (red) is for $\alpha = \pi/4$, lower line (blue) for $\alpha = \pi/2$. Points are results of numerical integration of the slow-time equations. Lines are theoretical predictions for the threshold of existence of the in-phase state, from the system (4.74). Lower line (blue) is $b = 2\Gamma$ (where Γ=FWHM).

critical N value, the slow time scale is

$$t_{\text{slow}} \approx 20 sec . \tag{4.104}$$

The separation of time scales is acceptable here because, as it turns out,

$$\epsilon = \sqrt{\frac{NGC}{K\Omega_0}} \approx 0.05$$

(obtained by plugging in parameters from the Millennium Bridge's north span in the definition of ϵ, (4.8)). This confirms our earlier assumption that $\epsilon \ll 0$.

There remains at least an order of magnitude separation of time scales ($\epsilon \leq 0.1$) for values of N up to approximately 635, meaning that our approximations are valid for any reasonable crowd size (the crowd size on opening day was approximately 450 on the north span, and was close to the densest possible packing).

There is one more time scale that is relevant for this problem. We refer to it as t_{onset}, the time for exponential growth of the instability when N is close to the
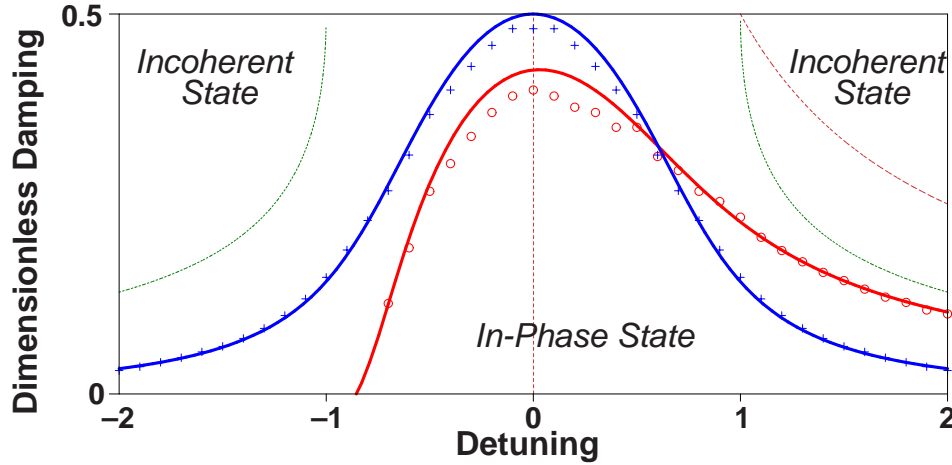
Figure 4.22: The behavior of b_c, the critical dimensionless damping, versus the detuning $\overline{\omega}$ of the Lorentzian distribution $g(\omega)$. Full width is $\Gamma = 1$. Thick upper line (blue) for $\alpha = \pi/2$, thick lower line (red) for $\alpha = \pi/4$. Points are results of numerical integration of the slow-time equations. Thick lines are theoretical predictions for the threshold of existence of the in-phase state, from the system (4.74). Symmetric upper thin line (green) is the stability boundary for the in-phase state (5.52) when $\Gamma \to 0$ and $\alpha = \pi/2$. The dotted upper thin line on the right (red) is the stability boundary for the in-phase state when $\Gamma \to 0$ and $\alpha = 0$.

critical value N_c. Assuming an initially incoherent walker population, this time constant diverges as $N \to N_c$ from above. The asymptotic formula (4.147), to be derived at the end of Section 4.13, behaves as

$$t_{\text{onset}} \approx \frac{3200}{N - N_c} sec .$$
(4.105)

Thus this time scale is the slowest for values of N just above the critical threshold. It's not until more than 150 walkers beyond N_c that it becomes comparable in magnitude to t_{slow}.

4.12 Estimation of Unknown Parameters α and C

We chose to use $\alpha = \pi/2$ in many calculations for two reasons. First, that was the only value besides $\alpha = 0$ for which an analytical solution to the self-consistency
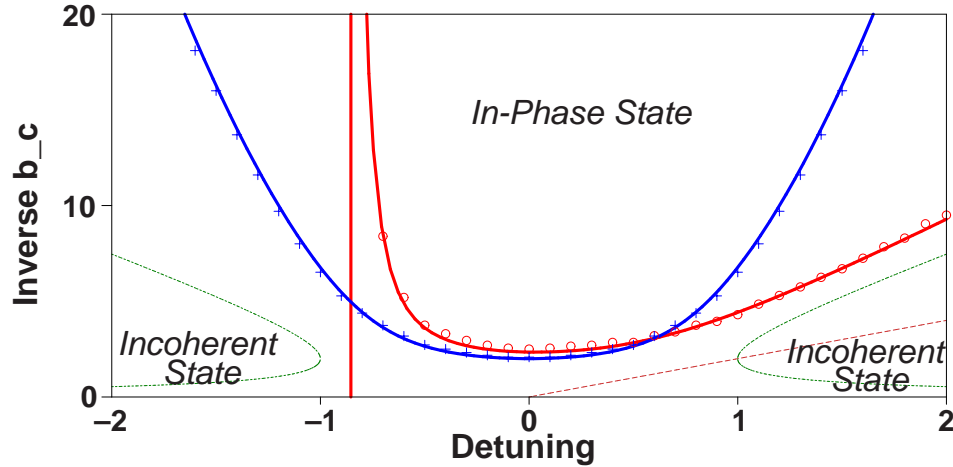
Figure 4.23: The behavior of b_c^{-1}, the critical dimensionless damping, versus the detuning $\overline{\omega}$ of the Lorentzian distribution $g(\omega)$. Full width is $\Gamma = 1$. Thick asymmetric line (red) for $\alpha = \pi/4$, thick symmetric line (blue) for $\alpha = \pi/2$. Points are results of threshold detection during numerical integration of the slow-time equations. Thick lines are theoretical predictions for the threshold of existence of the in-phase state, from the system (4.74). Lower thin lines (green) are the stability boundary for the in-phase state (5.52) when $\Gamma \to 0$ and $\alpha = \pi/2$. The dotted thin line on the right (red) is the stability boundary for the in-phase state when $\Gamma \to 0$ and $\alpha = 0$.

equations could be found. Second, $\alpha = \pi/2$ gives a "worst-case scenario" in the sense that the critical number of walkers N_c is minimized with respect to α (see Figure 4.25, and recall that $b_c^{-1} \propto \sqrt{N}$).

While $\alpha = 0$ was also explored, it the results of that case seemed physically implausible due to asymmetries in the predictions for $b_c(\omega)$. The predictions with $\alpha = \pi/2$, on the other hand, were quite believable.

We chose $C \approx 16m^{-1}s^{-1}$ by matching our model predictions to the Arup experiment shown in Figure 2.9. We wanted our prediction of N_c to be about 150 in that case, and so we solved for the appropriate C value. Equation (4.99) was used, with all the parameters for the fundamental mode on the North span of the Millennium Bridge, taking $\sigma = 0.1Hz$.

As a check, we were able to successfully predict the steady-state bridge vibra-
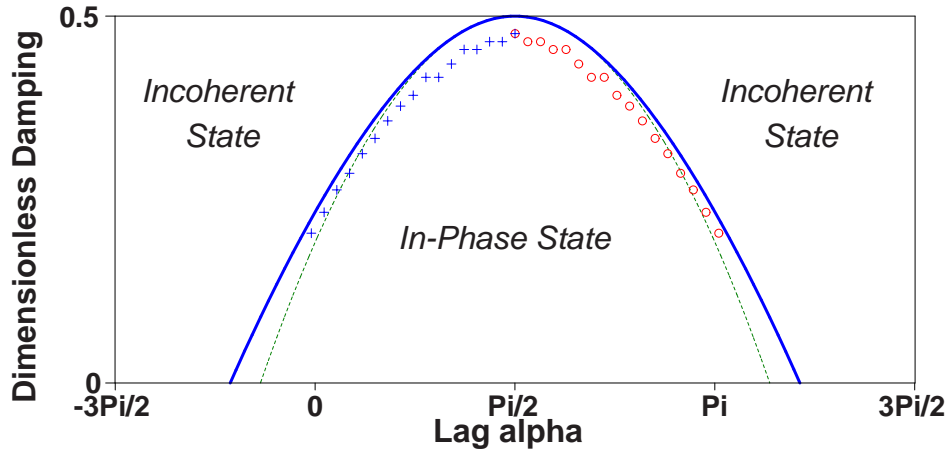
Figure 4.24: The behavior of b_c, the critical dimensionless damping, versus the lag parameter α assuming a Lorentzian distribution of native walker frequencies $g(\omega)$, with full width $\Gamma = 1$ and no detuning ($\overline{\omega} = 0$). The thick line (blue) is the theoretical prediction from the system (4.74). Crosses are results of threshold detection during numerical integration of the slow-time equations. Circles are mirrored values for the true calculated values (the system was fully symmetric). The dotted green line is the approximation to (4.74) for α near $\pi/2$, $8b = 4 - (\alpha - \pi/2)^2$.

tion amplitude and the time scales for onset, and we obtain the correct order of magnitude for the proportionality constant in Arup's $\alpha F_1 = kV_{local}$ relation without further tuning of parameters (see Sections 4.11 and 4.13). The prediction of k was off by about a factor of 5, possibly due to an affect discussed in Section 4.13.1, where we predict that the slope k is not really a constant. If the measured k were interpreted as an initial value during a long transient, then our prediction would be more consistent with the data.

4.13 Comparison to Published Experimental Data

In their publications, Arup considered an observed empirical relationship $\alpha F_1 \propto V_{local}$ to be very important. Their supporting data is reproduced from [6] in Figure 3.1, and again (perhaps more legibly) from [24] in Figure 2.8.
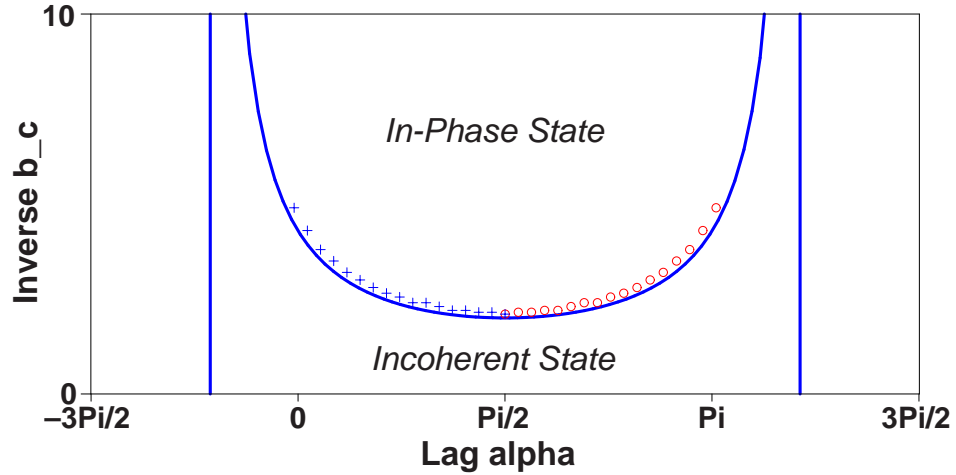
Figure 4.25: The behavior of b_c^{-1}, the critical dimensionless damping, versus the lag parameter α assuming a Lorentzian distribution of native walker frequencies $g(\omega)$, with full width $\Gamma = 1$ and no detuning ($\overline{\omega} = 0$). The thick line (blue) is the theoretical prediction from the system (4.74). Crosses are results of threshold detection during numerical integration of the slow-time equations. Circles are mirrored values for the true calculated values (the system was fully symmetric).

We would like to examine the implications of our model, with the goal of comparing our predictions to the empirical law documented in Arup's experiments. In order to do so, we need to consider the analogue of αF_1 in our system.

The quantity that Arup calls αF_1 is the component of the mean pedestrian force in phase with the velocity of the bridge, per person. Thus it would be the component of $G \langle \sin \Theta_j \rangle$ in phase with $\frac{dX}{dt}$ in our model. To express this quantity, we start with the definition of A and Ψ, as described in [23]:

$$
\begin{aligned}
X &= A \sin \Psi, \\
\frac{dX}{dt} &= \Omega_0 A \cos \Psi .
\end{aligned}
\tag{4.106}
$$

These definitions are shown in Figure 4.3. As in (4.15), we write Ψ as a sum of a periodic oscillation with angular frequency Ω_0 and a slowly drifting piece $\psi(T)$, so
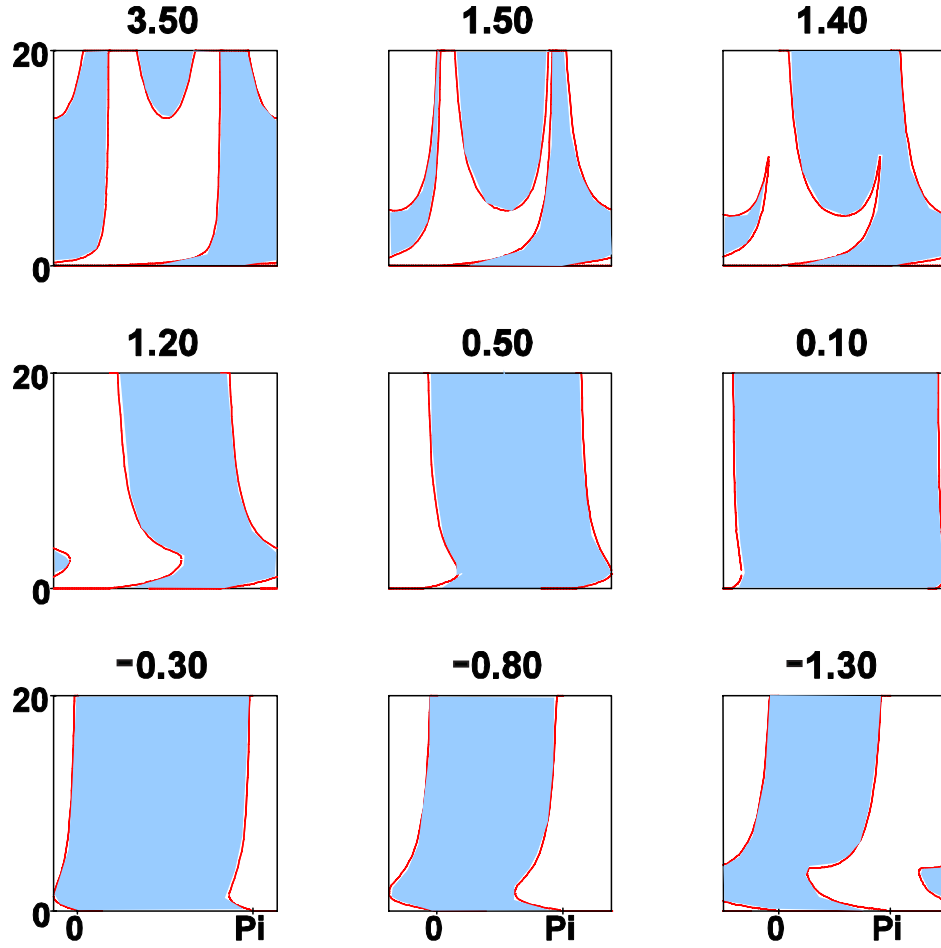
Figure 4.26: The behavior of b_c^{-1}, the inverse critical dimensionless damping, versus the lag parameter α assuming identical oscillators with varying detuning $\overline{\omega}$. Detunings are marked as the title of each panel. These boundaries are calculated from the stability of the in-phase state, using the characteristic equation (5.38). The in-phase state is stable in the shaded regions.

that

$$
\begin{aligned}
X &= A(T)\sin(\Omega_0 t + \psi(T)), \\
\frac{dX}{dt} &= \Omega_0 A(T)\cos(\Omega_0 t + \psi(T)) .
\end{aligned}
\tag{4.107}
$$

This is the velocity of the bridge. We can verify that this is valid for small ϵ by writing out the derivative

$$
\begin{aligned}
\frac{dX}{dt} &= \frac{dA}{dT}\frac{dT}{dt}\sin(\Omega_0 t + \psi(T)) + A(T)\cos(\Omega_0 t + \psi(T))\left(\Omega_0 + \frac{d\psi}{dT}\frac{dT}{dt}\right), \\
&= \Omega_0 A(T)\cos(\Omega_0 t + \psi(T)) + \mathcal{O}\left(\epsilon\right) ,
\end{aligned}
$$

where we've used (4.8) and (4.17). What Arup calls V_{local} is the amplitude of the oscillating lateral bridge deck velocity, i.e., $\Omega_0 A$ in (4.106). We can also write this in dimensionless variables,

$$
V_{local} = \Omega_0 A = \Omega_0 a \sqrt{\frac{NG\Omega_0}{KC}} .
\tag{4.108}
$$

Now we calculate the component of the mean pedestrian force in phase with the bridge velocity,

$$
\begin{aligned}
G\left\langle \sin\Theta_j \right\rangle &= G\left\langle \sin(\Omega_0 t + \psi + (\theta_j - \psi)) \right\rangle, \tag{4.109} \\
&= G\sin(\Omega_0 t + \psi)\left\langle \cos(\theta_j - \psi) \right\rangle + G\cos(\Omega_0 t + \psi)\left\langle \sin(\theta_j - \psi) \right\rangle .
\end{aligned}
$$

We saw above in (4.107) that the bridge velocity goes like $\cos(\Omega_0 t + \psi(T))$. So the coefficient of that same term in (4.109) must be the in-phase component of the mean pedestrian force in our model:

$$
\begin{aligned}
\alpha F_1 &= G\left\langle \sin(\theta_j - \psi) \right\rangle, \\
&= G\left[\left\langle \sin\theta_j \right\rangle\cos\psi - \left\langle \cos\theta_j \right\rangle\sin\psi\right] .
\end{aligned}
\tag{4.110}
$$

We can write down Arup's constant of proportionality k in our model as the ratio $\alpha F_1 / V_{local}$,

$$k = \frac{G}{\Omega_0 A} \left[\langle \sin \theta_j \rangle \cos \psi - \langle \cos \theta_j \rangle \sin \psi \right] . \tag{4.111}$$

We can improve the notation by writing population averages in terms of the complex order parameter $R \exp i\Phi$, defined as

$$R e^{i\Phi} = \langle e^{i\theta_j} \rangle , \tag{4.112}$$

(see "Order Parameter Formulation" on page 38). This defines the centroid of a system of phase oscillators with unit amplitude distributed in in the complex plane.

So

$$\begin{aligned} R \cos \Phi &= \langle \cos \theta_j \rangle , \\ R \sin \Phi &= \langle \sin \theta_j \rangle , \end{aligned} \tag{4.113}$$

thus (4.111) becomes

$$\begin{aligned} k &= \frac{G}{\Omega_0 A} \left[R \sin \Phi \cos \psi - R \cos \Phi \sin \psi \right], \\ &= \frac{GR}{\Omega_0 A} \sin(\Phi - \psi) . \end{aligned} \tag{4.114}$$

4.13.1 Invariant Manifold

There is an antisymmetric invariant manifold in the slow-time system (4.42) with $\alpha = \pi/2$, defined by

$$\begin{aligned} \theta_j &= -\theta_{-j}, \\ \omega_j &= -\omega_{-j}, \\ \psi &= -\pi/2, \\ \Phi &= 0 . \end{aligned} \tag{4.115}$$

If the initial condition lies on this manifold, then the system will remain on the manifold for all T. This can be seen because, under the listed conditions, we have at $T = 0$

$$\dot{\theta}_j = \omega_j - a \sin \theta_j \ . \tag{4.116}$$

$\Phi = 0$ implies that $\langle \sin \theta_j \rangle = 0$. The antisymmetry in the system means that for every oscillator with increasing θ_j (positive $\dot{\theta}_j$), there will be a corresponding oscillator with equally decreasing θ_{-j} (negative $\dot{\theta}_j$). Thus the mean value $\langle \sin \theta_j \rangle$ will remain zero for all time.

The first equation in (4.42) becomes

$$a\dot{\psi} = -\frac{1}{2} R \cos(-\pi/2) = 0 \ , \tag{4.117}$$

a verification that $\psi = -\pi/2$ is a valid solution.

So using $\psi = -\pi/2$ and $\Phi = 0$ in (4.114), we see

$$k = \frac{G}{\Omega_0} \frac{R(T)}{A(T)} \ , \tag{4.118}$$

which is *not* constant in our model, but rather a slowly varying function of time.

At steady state, the second equation in (4.42) must reach $\dot{a} = 0$ when $T \to \infty$. Thus we get

$$0 = \lim_{T \to \infty} \left(\frac{1}{2} R(T) - ba(T) \right) \ , \tag{4.119}$$

$$\boxed{\lim_{T \to \infty} \frac{R(T)}{a(T)} = 2b \ .} \tag{4.120}$$

Figures 4.27 and 4.28 show the results of numerical integration of the slow-time system (4.37) and comparison with the prediction (4.120). In the case where $b \ll b_c$, the transient curve R vs. a deflects above the steady-state prediction $R = 2ba$. However, when b is near the critical value b_c—equivalent to N just
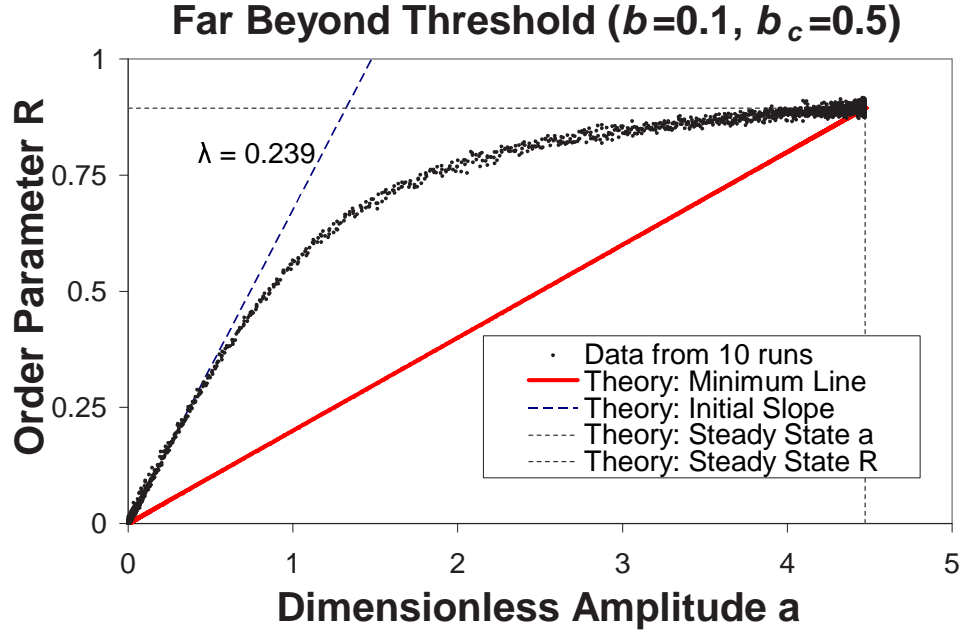
Figure 4.27: A plot of the magnitude order parameter R versus the dimensionless amplitude a during the build-up of oscillation, from numerical integration of the slow-time equations (see Chapter 6). Natural frequencies are Lorentzian distributed with mean $\overline{\omega} = 0$ and full-width $\Gamma = 1.0$. The solid line (red) shows the theoretical lower bound, equivalent to the value of R/a for $T \to \infty$, $R = 2ba$. The line with long dashing (blue) shows the theoretical estimate of the initial slope given by equation (4.139), with $\lambda = 0.239$ calculated from equation (4.137). The horizontal and vertical lines with short dashing (black) show the theoretical estimates for the steady state amplitude a_{ss} and order parameter R_{ss}. Here the dimensionless damping $b = 0.1$ is much less than the critical damping $b_c = 0.5$.

beyond N_c in dimensional variables—then the transient curve closely follows the steady-state line.

We can plug this result into our formula for k (4.114), to find an expression on the invariant manifold

$$
\begin{aligned}
k &= \frac{GR}{\Omega_0 A}, \\
k &= \frac{G}{\Omega_0 L} \frac{R}{a}, \\
\lim_{T \to \infty} k &= \frac{2bG}{\Omega_0 L} .
\end{aligned}
\tag{4.121}
$$

Near Threshold (b=0.4, b_c=0.5)
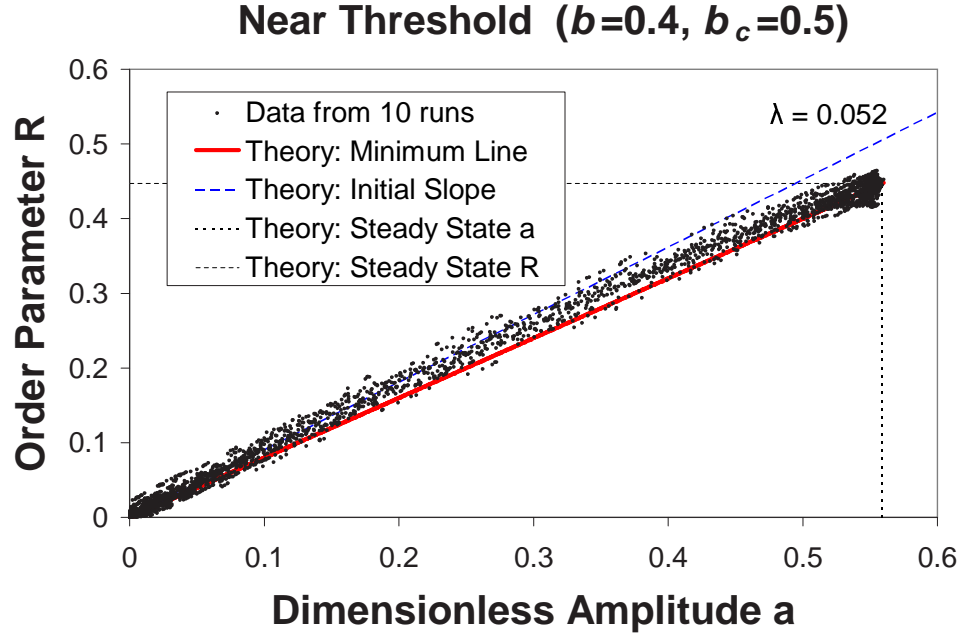
Figure 4.28: A plot of the magnitude order parameter R versus the dimensionless amplitude a during the build-up of oscillation, from numerical integration of the slow-time equations (see Chapter 6). Natural frequencies are Lorentzian distributed with mean $\overline{\omega} = 0$ and full-width $\Gamma = 1.0$. The solid line (red) shows the theoretical lower bound, equivalent to the value of R/a for $T \rightarrow \infty$, $R = 2ba$. The line with long dashing (blue) shows the theoretical estimate of the initial slope given by equation (4.139), with $\lambda = 0.052$ calculated from equation (4.137). The horizontal and vertical lines with short dashing (black) show the theoretical estimates for the steady state amplitude a_{ss} and order parameter R_{ss}. Here the dimensionless damping $b = 0.4$ is close to the critical damping $b_c = 0.5$.

In dimensional variables, this is

$$\lim_{T \rightarrow \infty} k = \frac{2\zeta K}{N\Omega_0} = \frac{B}{N} \ . \tag{4.122}$$

The simple formula indicates a balance between the damping forces of the bridge, and the driving due to the pedestrians.

For the fundamental mode of the unmodified center span of the Millennium Bridge, the formula (4.122) predicts that $k \approx 300$ when $N \approx 20$. However, Arup's published data supporting their value $k \approx 300$ came from a modified center span,
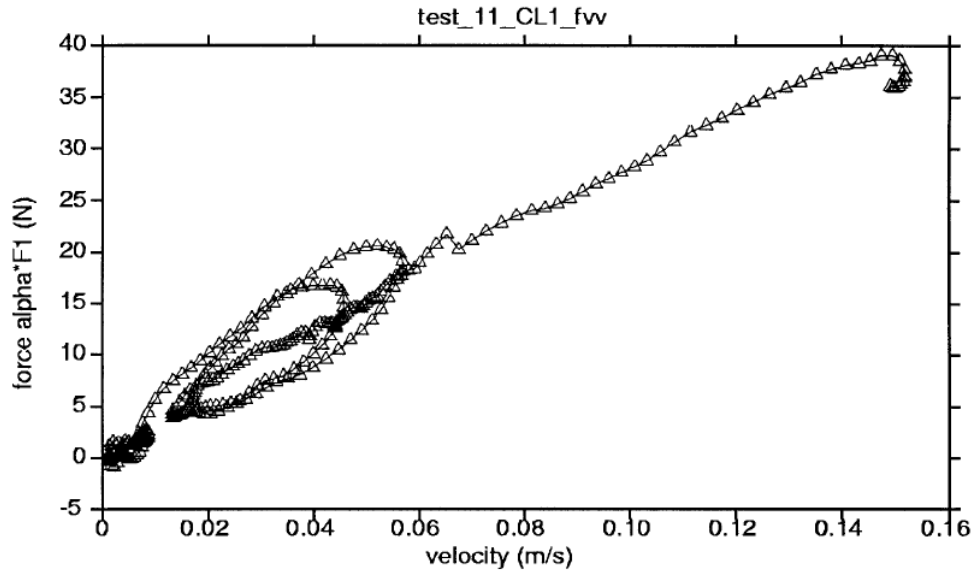
Figure 4.29: Typical plot of correlated lateral modal force per person versus velocity for an experiment done by Arup on the Millennium Bridge. The title indicates that the test was done on the fundamental lateral mode of the center span (CL1). Tests were done with a group size that varied from 165 to 190 to 214 walkers. Figure taken from [10].

in which the damping ratio had been increased to 2.8%[1]. Assuming that modified value for ζ, our model predicts that $k \approx 300$ when $N \approx 73$. For the values of N used in the published data (see Figures 4.29 and 4.30), we predict that k should be in the range $101 - 132$, off from experimental results by about a factor of 3.

It should be noted that the effective value of N varied as the experimental group circulated past the node and antinodes of the span. This effect is clearly seen in a typical lateral force history as shown in Figures 4.29 and 4.30. The fact that the modal force per person was decreasing at times suggests that the group was not uniformly distributed across the modeshape.

[1]Private correspondence with Pat Dallard.
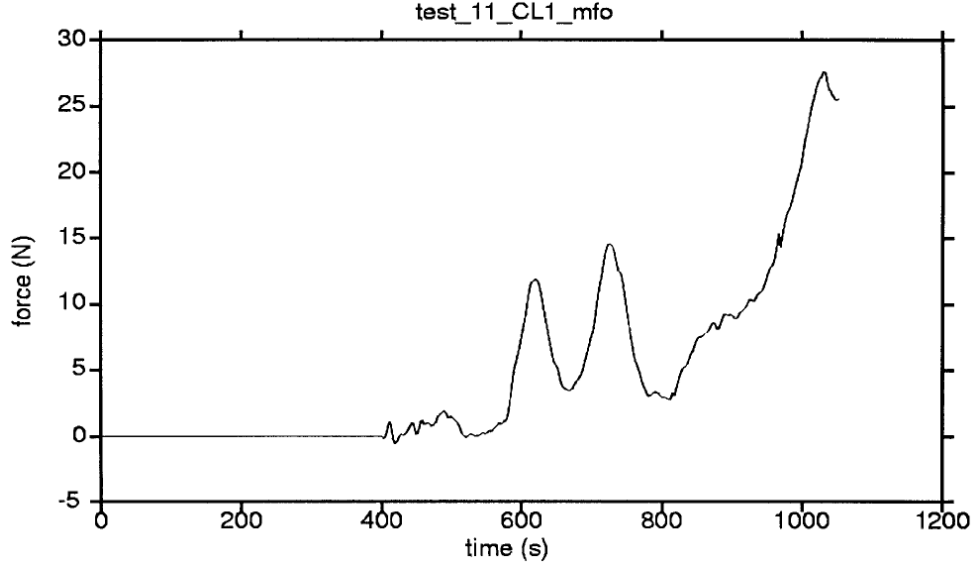
Figure 4.30: Typical plot of lateral modal force per person versus velocity for an experiment done by Arup on the Millennium Bridge. The title indicates that the test was done on the fundamental lateral mode of the center span (CL1). Tests were done with a group size that started with 165 walkers at $t = 400$, then increased to 190 at $t = 816$, and again increased to a final value of 214 at $t = 968$. Figure taken from [10].

Transient Build-up of Oscillations

Numerical simulations indicate that the antisymmetric invariant manifold is locally attracting, so understanding the dynamics within the manifold should give some intuition into the behavior of the system as a whole. By looking at the slow-flow on the invariant manifold described in the previous section, we hope to find a description of the transient behavior of the system—not just the steady state. We'll look for an equation of the form $\dot{R} = f(R, a)$ near the onset of the instability.

The slow-time system on the invariant manifold is

$$
\begin{aligned}
\dot{a} &= \frac{1}{2}R - ba, \\
\frac{\partial \rho}{\partial t} &= -\frac{\partial}{\partial \theta}(\rho v) \,,
\end{aligned}
\tag{4.123}
$$

where we've used (4.115) in (4.42), and have taken the continuum limit. v is given

by the continuum limit of Equation (4.116),

$$v(\theta, T, \omega) = \omega - a \sin \theta \ . \tag{4.124}$$

As described above, $\langle \sin \theta \rangle = 0$ on the manifold, so

$$R = \langle \cos \theta \rangle = \oint \rho(\theta, T, \omega) \cos \theta g(\omega) d\omega \ , \tag{4.125}$$

and of course ρ must be normalized so that $\oint \rho d\theta = 1$ for all T and ω.

To look for the unstable eigenvector, we'll perturb off the incoherent state, using

$$\begin{aligned}
\rho &= \frac{1}{2\pi} + \eta, \\
a &= 0 + a \ ,
\end{aligned} \tag{4.126}$$

where $|\eta| \ll 1$ and $a \ll 1$.

Starting with the second slow-time equation in (4.123),

$$\begin{aligned}
\frac{\partial \eta}{\partial T} &= -\frac{\partial}{\partial \theta} \left[\left(\frac{1}{2\pi} + \eta \right) (\omega - a \sin \theta) \right], \\
&= -\omega \frac{\partial \eta}{\partial \theta} + \frac{a}{2\pi} \cos \theta + \mathcal{O}(\eta a) \ .
\end{aligned} \tag{4.127}$$

Now take $\eta = \eta_0 \exp(\lambda T)$ and $a = a_0 \exp(\lambda T)$. Then, to lowest order,

$$\begin{aligned}
\lambda \eta_0 e^{\lambda T} &= \left(-\omega \frac{\partial \eta_0}{\partial \theta} + \frac{a_0}{2\pi} \cos \theta \right) e^{\lambda T}, \\
\lambda \eta_0 &= -\omega \frac{\partial \eta_0}{\partial \theta} + \frac{a_0}{2\pi} \cos \theta \ .
\end{aligned} \tag{4.128}$$

We guess a harmonic solution

$$\eta_0 = \eta_c \cos \theta + \eta_s \sin \theta \ , \tag{4.129}$$

which gives

$$\lambda \eta_c \cos \theta + \lambda \eta_s \sin \theta = \omega \eta_c \sin \theta - \omega \eta_s \cos \theta + \frac{a_0}{2\pi} \cos \theta \ . \tag{4.130}$$

Equating coefficients of trigonometric terms on both sides of (4.130) yields two equations,

$$\lambda \eta_c = -\omega \eta_s + \frac{a_0}{2\pi},$$
$$\lambda \eta_s = \omega \eta_c \ . \tag{4.131}$$

We solve for η_c and η_s in the system (4.131) to get

$$\eta_c = \frac{\lambda}{\lambda^2 + \omega^2} \frac{a_0}{2\pi},$$
$$\eta_s = \frac{\omega}{\lambda^2 + \omega^2} \frac{a_0}{2\pi} \ . \tag{4.132}$$

Plugging back into our guess (4.129), we get

$$\eta_0 = \frac{a_0}{2\pi} \frac{\lambda \cos\theta + \omega \sin\theta}{\lambda^2 + \omega^2} \ . \tag{4.133}$$

Now we go back to the first slow-time equation in (4.123), and we again plug in for $a = a_0 \exp(\lambda T)$,

$$\lambda a_0 e^{\lambda T} = \frac{1}{2} R - b a_0 e^{\lambda T} \ . \tag{4.134}$$

We can plug in for $R = \langle \cos\theta \rangle$ from above,

$$
\begin{aligned}
R &= \oint \int_{-\infty}^{\infty} \rho g(\omega) d\omega \cos\theta d\theta, \\
&= \oint \int_{-\infty}^{\infty} \left(\frac{1}{2\pi} + \eta_0 e^{\lambda T} \right) g(\omega) d\omega \cos\theta d\theta, \\
&= e^{\lambda T} \int_{-\infty}^{\infty} \oint \eta_0 \cos\theta d\theta g(\omega) d\omega, \\
&= e^{\lambda T} \int_{-\infty}^{\infty} \oint (\eta_c \cos\theta + \eta_s \sin\theta) \cos\theta d\theta g(\omega) d\omega, \\
&= e^{\lambda T} \int_{-\infty}^{\infty} \oint \eta_c \cos^2\theta d\theta g(\omega) d\omega, \\
&= \pi e^{\lambda T} \int_{-\infty}^{\infty} \eta_c(\omega) g(\omega) d\omega, \\
&= \frac{1}{2} a_0 e^{\lambda T} \int_{-\infty}^{\infty} \frac{\lambda}{\lambda^2 + \omega^2} g(\omega) d\omega \ .
\end{aligned}
\tag{4.135}
$$

So Equation (4.134) becomes

$$
\lambda a_0 e^{\lambda T} = \frac{a_0}{4} \int_{-\infty}^{\infty} \frac{\lambda}{\lambda^2 + \omega^2} g(\omega) d\omega e^{\lambda T} - b a_0 e^{\lambda T} \ .
\tag{4.136}
$$

Canceling out the common factor of $a_0 e^{\lambda T}$, we get the characteristic equation for λ:

$$
\boxed{b + \lambda = \frac{1}{4} \int_{-\infty}^{\infty} \frac{\lambda}{\lambda^2 + \omega^2} g(\omega) d\omega \ .}
\tag{4.137}
$$

Now from (4.125) we see that R initially grows exponentially with time scale determined by the unstable eigenvalue. That is, $R(T) = R_0 \exp(\lambda T)$, and with

(4.135) we get

$$R_0 e^{\lambda T} = \frac{1}{2} a_0 e^{\lambda T} \int_{-\infty}^{\infty} \frac{\lambda}{\lambda^2 + \omega^2} g(\omega) d\omega,$$

$$R(T) = a(T) \left[\frac{1}{2} \int_{-\infty}^{\infty} \frac{\lambda}{\lambda^2 + \omega^2} g(\omega) d\omega \right] . \tag{4.138}$$

But we can plug in for the quantity in brackets from the characteristic equation (4.137), so

$$\boxed{R(T) = 2(b + \lambda) a(T) .} \tag{4.139}$$

At the onset of the instability, $\lambda \to 0^+$ and $R \approx 2ba$. After the system reaches steady state, we know from our work in Section 4.13.1 (see Equation (4.120)) that $R(T \to \infty) = 2ba(T \to \infty)$. When $\lambda > 0$ (which it must be if the incoherent state is unstable), then the slope of the function $R(a)$ will be greater than $2b$, so during transients that curve must have initial slope above the line $R = 2ba$, although it must return to the line as $T \to \infty$.

Conveniently, this is exactly the behavior that we see in numerical simulations. Figure 4.27 shows a system where the unstable eigenvalue is fairly large, while Figure 4.28 shows a system just barely unstable—with a value of λ just above zero.

Limit for small λ

If we take $\lambda \to 0^+$ in the characteristic equation (4.137), we should be able to recover the formula for the onset of instability derived given in Equation (4.77).

Taking the limit on both sides of (4.137),

$$
\begin{aligned}
b_c &= \frac{1}{4} \lim_{\lambda \to 0+} \int_{-\infty}^{\infty} \left[\frac{\lambda}{\lambda^2 + \omega^2} \right] g(\omega) d\omega, \\
&= \frac{1}{4} \int_{-\infty}^{\infty} \left[\pi \delta(\omega) \right] g(\omega) d\omega, \\
&= \frac{\pi}{4} g(0) ,
\end{aligned}
\tag{4.140}
$$

where we've used the simplification

$$
\lim_{\lambda \to 0+} \frac{\lambda}{\lambda^2 + \omega^2} = \pi \delta(\omega) ,
$$

since this describes a Lorentzian of full-width-at-half-maximum 2λ.

Special Case: Lorentzian Distribution $g(\omega)$

If we assume a Lorentzian form for $g(\omega)$, the characteristic equation (4.137) becomes exactly solvable.

Taking

$$
g(\omega) = \frac{1}{\pi} \frac{\Gamma/2}{\omega^2 + (\Gamma/2)^2} ,
\tag{4.141}
$$

$$
\begin{aligned}
b + \lambda &= \frac{1}{4} \int_{-\infty}^{\infty} \frac{\lambda}{\lambda^2 + \omega^2} g(\omega) d\omega, \\
b + \lambda &= \frac{1}{4} \left[\frac{2}{2\lambda + \Gamma} \right], \\
b &= \frac{1}{2} \frac{1}{2\lambda + \Gamma} - \lambda .
\end{aligned}
\tag{4.142}
$$

Solving for λ results in a quadratic equation.

Special Case: Gaussian Distribution $g(\omega)$

In the case of a Gaussian distribution of walker frequencies, we can simplify the characteristic equation (4.137) as follows.

Take

$$g(\omega) = \frac{1}{\sigma\sqrt{2\pi}}e^{-\omega^2/(2\sigma^2)} \ , \tag{4.143}$$

$$b + \lambda = \frac{1}{4}\int_{-\infty}^{\infty}\frac{\lambda}{\lambda^2 + \omega^2}g(\omega)d\omega,$$

$$b + \lambda = \frac{1}{4}\left[\frac{1}{\sigma}\sqrt{\frac{\pi}{2}}e^{\lambda^2/(2\sigma^2)}\left\{\mathrm{erf}(\frac{\lambda}{\sigma\sqrt{2}}) - 1\right\}\right],$$

$$b = \frac{\sqrt{2\pi}}{8\sigma}e^{\lambda^2/(2\sigma^2)}\left[\mathrm{erf}(\frac{\lambda}{\sigma\sqrt{2}}) - 1\right] - \lambda \ . \tag{4.144}$$

This expression can't be solved for λ in closed form, so it's not so illuminating. However, we *can* do a Taylor expansion of the right hand side of (4.144) to find $\lambda(b)$ for small λ. That gives:

$$b \approx \frac{\pi}{4}g(0) - \frac{1}{4\sigma^2}\lambda + \mathcal{O}\left(\lambda^2\right) - \lambda,$$

$$b \approx \frac{\pi}{4}g(0) - \lambda\left(1 + \frac{1}{4\sigma^2}\right),$$

$$\lambda\left(1 + \frac{1}{4\sigma^2}\right) \approx \frac{\pi}{4}g(0) - b \ ,$$

$$\lambda \approx \left(\frac{\pi}{4}g(0) - b\right)\frac{4\sigma^2}{4\sigma^2 + 1} \ . \tag{4.145}$$

The time constant for the onset of oscillations is determined by the inverse of λ, since $R(T) = R_0\exp(\lambda T)$, and thus we can write $T_{onset} = 1/\lambda$, or

$$T_{onset} \approx \left(1 + \frac{1}{4\sigma^2}\right)\frac{4}{\pi g(0) - 4b} \ . \tag{4.146}$$

This expression, when converted to dimensional variables, becomes

$$\boxed{t_{onset} \approx \left(1 + \frac{1}{4\sigma^2}\right)\zeta^{-1}\Omega^{-1}\frac{N_c}{N - N_c} \ .} \tag{4.147}$$

Note that σ above still refers to the standard deviation of the detunings in the distribution $g(\omega)$, *not* the standard deviation for $P(\Omega)$. The conversion is $\sigma_\Omega = \epsilon\Omega_0\sigma_\omega$.

In Section 4.11, we used this formula to estimate the onset time scale for the north span of Millennium Bridge.

4.13.2 Conclusions

Our model successfully explains some phenomena, but also has certain limitations. Specifically, we obtained the following results:

- We are able to explain the onset of bridge vibration above a critical threshold in N, and we can predict that value N_c given the parameters of the bridge.

- Our model predicts simultaneous growth of bridge movement and crowd synchronization, an observation that was unexplained in previous models.

- Our model accounts for the observed linearity between pedestrian forcing and bridge vibration amplitude, and predicts the constant of proportionality within a factor of 3. Furthermore, we predict that the linearity only holds near the critical crowd size N_c, otherwise we expect the observed slope to be higher than predicted.

- We can predict time scales for onset of bridge motion, in good agreement with observations and experiment.

All of these results were obtained with a very simple, analytically tractable model, and should be applicable to any bridge where a similar phenomena is observed.

Limitations

Because our model is very simplified, our predictions may be off from experiment by a factor of 2–3 or more. Some of the simplifications that we made included:

- We assume sinusoidal pedestrian forcing when higher harmonics are clearly present.

- We ignore the observed and documented effect of the change in gait of the walkers on a moving bridge (this can lead to almost an order of magnitude change in the amplitude pedestrian forcing, although it shouldn't affect N_c).

- We do not account for subharmonic or superharmonic resonances in our theory.

To make numerical predictions, we had to select a value for the unknown parameter C. We chose it so as to make our prediction for N_c coincide with the results of experiments on the Millennium Bridge. However, the subsequent predictions for the proportionality constant k and the time scales for onset of bridge motion provided some validation of our model. We welcome an experiment to independently establish the value of C for an average pedestrian.

CHAPTER 5

STABILITY AND NOISE

Until now, we have dealt exclusively with the existence of various states in our model (4.6). In this chapter we will examine the stability of the incoherent and in-phase states, which we fully evaluate under the simplifying assumption of identical walkers. We also look at the behavior of our model and the persistence of the steady states when random noise is present.

5.1   Stability of the Incoherent State

To evaluate the stability of the incoherent state, we will start by extending our system to a continuum limit, as done in Section 4.9.3. Thus the slow-time system from (4.37) becomes

$$
\begin{aligned}
a\dot{\psi} &= -\frac{1}{2} \int_{-\infty}^{\infty} \left[\oint \cos(\theta - \psi)\rho(\theta,\omega)d\theta \right] g(\omega)d\omega, \\
\dot{a} &= \frac{1}{2} \int_{-\infty}^{\infty} \left[\oint \sin(\theta - \psi)\rho(\theta,\omega)d\theta \right] g(\omega)d\omega - ba, \\
\dot{\theta} &= \omega + a\sin(\psi - \theta + \alpha) \ .
\end{aligned}
\tag{5.1}
$$

To simplify the following work, we reuse the angle-bracket notation $\langle \cdot \rangle$ to indicate the mean value over the population. It will be the continuum analogue of the previously used definition (4.10):

$$
\langle Y(\theta;\omega) \rangle = \int_{-\infty}^{\infty} \oint Y(\theta;\omega)\rho(\theta,\omega)d\theta g(\omega)d\omega \ ,
\tag{5.2}
$$

where Y is any function of θ and ω.

The continuum system (5.1) can be rewritten as

$$a\dot{\psi} = -\frac{1}{2}\langle\cos(\theta - \psi)\rangle,$$

$$\dot{a} = \frac{1}{2}\langle\sin(\theta - \psi)\rangle - ba,$$

$$\dot{\theta} = \omega + a\sin(\psi - \theta + \alpha) . \tag{5.3}$$

The incoherent state has zero amplitude for the bridge motion, $\dot{a} = 0$, and uniformly distributed oscillators, $\rho(\theta) = 1/(2\pi)$, with ψ undefined.

To avoid having problems with ψ being undefined, we change to a coordinate system

$$u = a\cos(\psi),$$

$$w = a\sin(\psi) . \tag{5.4}$$

In that coordinate system, we can rewrite the governing equations as follows:

$$\begin{aligned}
\dot{u} &= \dot{a}\cos(\psi) - a\dot{\psi}\sin(\psi),\\
&= \left[\frac{1}{2}\langle\sin(\theta - \psi)\rangle - ba\right]\cos(\psi) - \left[-\frac{1}{2}\langle\cos(\theta - \psi)\rangle\right]\sin(\psi),\\
&= \left[\frac{1}{2}\langle\sin\theta\cos\psi - \sin\psi\cos\theta\rangle - ba\right]\cos(\psi)\\
&\quad + \frac{1}{2}\langle\cos\theta\cos\psi + \sin\theta\sin\psi\rangle\sin(\psi),\\
&= \frac{1}{2}\cos^2\psi\langle\sin\theta\rangle - \frac{1}{2}\cos\psi\sin\psi\langle\cos\theta\rangle - ba\cos\psi + \frac{1}{2}\sin\psi\cos\psi\langle\cos\theta\rangle\\
&\quad + \frac{1}{2}\sin^2\psi\langle\sin\theta\rangle,\\
&= \frac{1}{2}\langle\sin\theta\rangle - ba\cos\psi,\\
&= \frac{1}{2}\langle\sin\theta\rangle - bu , \tag{5.5}
\end{aligned}$$

where we've used (5.3) and the definitions (5.4).

Similarly,

$$
\begin{aligned}
\dot{w} &= \dot{a}\sin(\psi) + a\dot{\psi}\cos(\psi), \\
&= \left[\frac{1}{2}\langle\sin(\theta-\psi)\rangle - ba\right]\sin(\psi) + \left[-\frac{1}{2}\langle\cos(\theta-\psi)\rangle\right]\cos(\psi), \\
&= \left[\frac{1}{2}\langle\sin\theta\cos\psi - \sin\psi\cos\theta\rangle - ba\right]\sin(\psi) \\
&\quad -\frac{1}{2}\langle\cos\theta\cos\psi + \sin\theta\sin\psi\rangle\cos(\psi), \\
&= \frac{1}{2}\sin\psi\cos\psi\langle\sin\theta\rangle - \frac{1}{2}\sin^2\psi\langle\cos\theta\rangle - ba\sin\psi - \frac{1}{2}\cos^2\psi\langle\cos\theta\rangle \\
&\quad -\frac{1}{2}\sin\psi\cos\psi\langle\sin\theta\rangle, \\
&= -\frac{1}{2}\langle\cos\theta\rangle - ba\sin\psi, \\
&= -\frac{1}{2}\langle\cos\theta\rangle - bw.
\end{aligned}
\tag{5.6}
$$

Finally, the continuity equation (conservation of oscillators - see Section 4.9.4) tells us that

$$
\dot{\rho} = -\frac{\partial}{\partial\theta}(\rho\dot{\theta}), \tag{5.7}
$$

where $\dot{\theta}$ is given above in (5.3). It can be expressed in terms of u and v by expanding the sine term:

$$
\dot{\rho} = -\frac{\partial}{\partial\theta}\left\{\rho\left[\omega + u\sin(\alpha-\theta) + w\cos(\alpha-\theta)\right]\right\}. \tag{5.8}
$$

So the full system in these variables is

$$
\begin{aligned}
\dot{u} &= \frac{1}{2}\langle\sin\theta\rangle - bu, \\
\dot{w} &= -\frac{1}{2}\langle\cos\theta\rangle - bw, \\
\dot{\rho} &= -\frac{\partial}{\partial\theta}\left\{\rho\left[\omega + u\sin(\alpha-\theta) + w\cos(\alpha-\theta)\right]\right\}.
\end{aligned}
\tag{5.9}
$$

The incoherent fixed point $\dot{\rho} = 0$ occurs when $\rho\dot{\theta} = \rho^*\dot{\theta} = $ constant in Equation (5.7). At steady state $\dot{\theta} = \omega = $ constant, so we must have $\rho^* = $ constant as

well. The normalization condition $\oint \rho d\theta = 1$ determines that constant so that $\rho^* = 1/(2\pi)$.

We perturb off the base state $(u^* = 0, w^* = 0, \rho^* = 1/(2\pi))$ by adding small perturbations of the form

$$
\begin{aligned}
u &= u^* + \delta u = \delta u, \\
w &= w^* + \delta w = \delta w, \\
\rho &= \rho^* + \delta\rho = \frac{1}{2\pi} + \frac{\eta}{2\pi} ,
\end{aligned} \tag{5.10}
$$

where we've defined $\eta = 2\pi\delta\rho$ for notational convenience. Now the system (5.9) becomes

$$
\begin{aligned}
\delta\dot{u} &= -b\delta u + \frac{1}{2}\int_{-\infty}^{\infty}\oint \sin\theta \frac{\eta(\theta,\omega)}{2\pi}d\theta g(\omega)d\omega, \\
\delta\dot{w} &= -b\delta w - \frac{1}{2}\int_{-\infty}^{\infty}\oint \cos\theta \frac{\eta(\theta,\omega)}{2\pi}d\theta g(\omega)d\omega, \\
\frac{1}{2\pi}\dot{\eta} &= -\frac{\partial}{\partial\theta}\left[\frac{1}{2\pi}(1+\eta)\left(\omega + \delta u\sin(\alpha-\theta) + \delta w\cos(\alpha-\theta)\right)\right] .
\end{aligned} \tag{5.11}
$$

The third equation can be simplified if we ignore terms that include products of small quantities, resulting in

$$
\dot{\eta} = -\frac{\partial}{\partial\theta}\left[\omega\eta + \delta u\sin(\alpha-\theta) + \delta w\cos(\alpha-\theta)\right] . \tag{5.12}
$$

Distributing the derivative with respect to θ,

$$
\begin{aligned}
\dot{\eta} &= -\omega\frac{\partial}{\partial\theta}\eta - \delta u\frac{\partial}{\partial\theta}\sin(\alpha-\theta) - \delta w\frac{\partial}{\partial\theta}\cos(\alpha-\theta), \\
&= -\omega\frac{\partial\eta}{\partial\theta} + \delta u\cos(\alpha-\theta) - \delta w\sin(\alpha-\theta) .
\end{aligned} \tag{5.13}
$$

Because this equation is linear in η, with driving terms proportional to $\sin\theta$ and $\cos\theta$ on the right hand side, we assume a solution of the form

$$
\eta(\theta,T) = C(T;\omega)\cos\theta + S(T;\omega)\sin\theta + \eta^\perp(\theta,T) , \tag{5.14}
$$

where $\eta^\perp$ contains all the higher harmonics in θ. Thus

$$\dot{\eta} = \dot{C}\cos\theta + \dot{S}\sin\theta + \dot{\eta}^\perp \ . \tag{5.15}$$

We can expand the trig functions in (5.13) and equate it with (5.15) to get:

$$\dot{C}\ \cos\theta + \dot{S}\sin\theta + \dot{\eta}^\perp$$

$$= -\omega\frac{\partial\eta}{\partial\theta} + \delta u\left(\cos\alpha\cos\theta + \sin\alpha\sin\theta\right) - \delta w\left(\sin\alpha\cos\theta - \sin\theta\cos\alpha\right)$$

$$= -\omega\left(S\cos\theta - C\sin\theta + \eta_\theta^\perp\right) + \cos\theta\left(-\sin\alpha\delta w + \cos\alpha\delta u\right)$$

$$+ \sin\theta\left(\cos\alpha\delta w + \sin\alpha\delta u\right)$$

$$= \cos\theta\left(-\omega S - \sin\alpha\delta w + \cos\alpha\delta u\right) + \sin\theta\left(\omega C + \cos\alpha\delta w + \sin\alpha\delta u\right) + \eta_\theta^\perp \ .$$

Matching coefficients of sine and cosine gives

$$\dot{C} = -\omega S - \sin\alpha\delta w + \cos\alpha\delta u,$$

$$\dot{S} = \omega C + \cos\alpha\delta w + \sin\alpha\delta u \ , \tag{5.16}$$

while equating the higher harmonic terms gives

$$\dot{\eta}^\perp = -\omega\frac{\partial\eta^\perp}{\partial\theta} \ , \tag{5.17}$$

which is the equation for a traveling wave $\eta^\perp(\theta - \omega T)$. Since perturbations like $\eta^\perp$ neither grow nor decay, the incoherent state is neutrally stable with respect to them (to this order).

Going back to the equations (5.11), we can plug in our guess (5.14), which then allows us to evaluate the θ integrals explicitly. They are straightforward to evaluate using the orthogonality of sine and cosine, along with $\oint \sin^2 x\,dx = \pi$.

$$\delta\dot{u} = -b\delta u + \frac{1}{2}\int_{-\infty}^{\infty}\oint\sin\theta\frac{\eta(\theta,\omega)}{2\pi}d\theta g(\omega)d\omega,$$

$$= -b\delta u + \frac{1}{4}\int_{-\infty}^{\infty} S(T;\omega)g(\omega)d\omega \ , \tag{5.18}$$

$$\delta\dot{w} = -b\delta w - \frac{1}{2}\int_{-\infty}^{\infty}\oint\cos\theta\frac{\eta(\theta,\omega)}{2\pi}d\theta g(\omega)d\omega,$$

$$= -b\delta w - \frac{1}{4}\int_{-\infty}^{\infty} C(T;\omega)g(\omega)d\omega \ . \tag{5.19}$$

That's as far as we have gone in the general case. To continue, in the following section we make further assumptions about the distribution $g(\omega)$.

5.2   Stability of the Incoherent State for Identical Walkers

In order to evaluate the ω integrals in (5.18) and (5.19), we now make the simplifying assumption that the distribution of walker frequencies approaches a Dirac delta function. That is, we assume identical walkers, so that $g(\omega) = \delta(\omega - \overline{\omega})$.

For simplicity of notation, we continue to use ω rather than $\overline{\omega}$ as the single shared frequency for all oscillators.

$$\delta\dot{u} = -b\delta u + \frac{1}{2}\int_{-\infty}^{\infty}\oint\sin\theta\frac{\eta(\theta,\omega)}{2\pi}d\theta g(\omega)d\omega,$$

$$= -b\delta u + \frac{1}{4}S,$$

$$\delta\dot{w} = -b\delta w - \frac{1}{2}\int_{-\infty}^{\infty}\oint\cos\theta\frac{\eta(\theta,\omega)}{2\pi}d\theta g(\omega)d\omega,$$

$$= -b\delta w - \frac{1}{4}C \ . \tag{5.20}$$

Summarizing the above—(5.20) and (5.16)—in matrix formulation by writing out the Jacobian matrix of the system:

$$\begin{bmatrix} \delta \dot{u} \\ \delta \dot{w} \\ \dot{C} \\ \dot{S} \end{bmatrix} = \begin{bmatrix} -b & 0 & 0 & \frac{1}{4} \\ 0 & -b & -\frac{1}{4} & 0 \\ \cos \alpha & -\sin \alpha & 0 & -\omega \\ \sin \alpha & \cos \alpha & \omega & 0 \end{bmatrix} \begin{bmatrix} \delta u \\ \delta w \\ C \\ S \end{bmatrix} . \tag{5.21}$$

Note once again that here ω is a constant value for all the identical oscillators, there is no longer a distribution $g(\omega)$.

The system is now in suitable shape to apply the Routh-Hurwitz stability criterion (see page 1076 in [12]). The characteristic equation is

$$\lambda^4 + b_1 \lambda^3 + b_2 \lambda^2 + b_3 \lambda + b_4 = 0 , \tag{5.22}$$

where

$$\begin{aligned} b_1 &= 2b \\ b_2 &= \omega^2 + b^2 - \frac{1}{2} \sin^2 \alpha \\ b_3 &= 2b\omega^2 - \frac{1}{2} b \sin \alpha - \frac{1}{2} \omega \cos \alpha \\ b_4 &= \frac{1}{16} + b^2 \omega^2 - \frac{1}{2} b\omega \cos \alpha . \end{aligned} \tag{5.23}$$

The critical determinants from the Routh-Hurwitz criterion are

$$\Delta_1 = 2b, \tag{5.24}$$

$$\Delta_2 = \frac{1}{2} \left(4b^3 + \omega \cos \alpha - b \sin \alpha \right),$$

$$\Delta_3 = -\frac{1}{4} \left(b^2 + \omega^2 \right) \left(\cos^2 \alpha - 4b\omega \cos \alpha + 4b^2 \sin \alpha \right),$$

$$\Delta_4 = -\frac{1}{64} \left(b^2 + \omega^2 \right) \left(1 - 8b\omega \cos \alpha + 16b^2 \omega^2 \right) \left(\cos^2 \alpha - 4b\omega \cos \alpha + 4b^2 \sin \alpha \right) .$$

The Routh-Hurwitz criterion states that our system will be stable if and only if $\Delta_1 > 0$, $\Delta_2 > 0$, $\Delta_3 > 0$, and $\Delta_4 > 0$.

- $\Delta_1 > 0$ for all positive b, which is an implicit assumption since $b = \epsilon^{-1}\zeta$, and $\zeta > 0$ for any real structure. $\epsilon > 0$ because it is constructed of real parameters all greater than zero.

- The critical condition from $\Delta_2 > 0$ is that $(\omega \cos \alpha - b \sin \alpha) > -4b^3$.

- The critical condition from $\Delta_3 > 0$ is that $(\omega \cos \alpha - b \sin \alpha) > \cos^2 \alpha /(4b)$.

- The unique critical condition (not repeating those already listed) from $\Delta_4 > 0$ is that $(4b\omega \cos \alpha - 1)^2 + (4b\omega \sin \alpha)^2 > 0$.

Special Case $\alpha = \pi/2$

Examining the Routh-Hurwitz determinants (5.24) with $\alpha = \pi/2$, we get:

$$
\begin{aligned}
\Delta_1 &= 2b, & (5.25) \\
\Delta_2 &= \frac{1}{2}(4b^3 - b) = \frac{1}{2}b(4b^2 - 1), \\
\Delta_3 &= -\frac{1}{4}\left(b^2 + \omega^2\right)\left(4b^2\right), \\
\Delta_4 &= -\frac{1}{64}\left(b^2 + \omega^2\right)\left(1 + 16b^2\omega^2\right)\left(4b^2\right) .
\end{aligned}
$$

Again, the Routh-Hurwitz criterion states that our system will be stable if $\Delta_1 > 0$, $\Delta_2 > 0$, $\Delta_3 > 0$, and $\Delta_4 > 0$.

- $\Delta_1 > 0$ for all positive b.

- $\Delta_2 > 0$ if $4b^2 > 1$, that is, if $b > 1/2$.

- $\Delta_3 < 0$ for all positive b!

- $\Delta_4 < 0$ for all positive b!

Because Δ_3 and Δ_4 are negative, the incoherent state is always unstable when $\alpha = \pi/2$. This is plausible, since the walkers are strictly identical in this calculation, although they may be detuned from the bridge's resonant frequency.

Special Case $\alpha = 0$

Examining the Routh-Hurwitz determinants (5.24) with $\alpha = 0$, we get:

$$\begin{aligned}
\Delta_1 &= 2b, & (5.26) \\
\Delta_2 &= \frac{1}{2}\left(4b^3 + \omega\right), \\
\Delta_3 &= -\frac{1}{4}\left(b^2 + \omega^2\right)\left(1 - 4b\omega\right), \\
\Delta_4 &= -\frac{1}{64}\left(b^2 + \omega^2\right)\left(4b\omega - 1\right)^2\left(1 - 4b\omega\right) .
\end{aligned}$$

Again, the Routh-Hurwitz criterion states that our system will be stable if and only if $\Delta_1 > 0$, $\Delta_2 > 0$, $\Delta_3 > 0$, and $\Delta_4 > 0$.

- $\Delta_1 > 0$ for all positive b.

- $\Delta_2 > 0$ for $4b^3 > -\omega$.

- $\Delta_3 > 0$ for $4b\omega > 1$.

- $\Delta_4 > 0$ for $4b\omega > 1$.

The conditions from Δ_3 and Δ_4 turn out to be stronger than the condition from Δ_2. Those stability conditions are:

$$\omega > -4b^3 \qquad (5.27)$$

$$\omega > \frac{1}{4b} \qquad (5.28)$$

Since we require $b > 0$ for a physical system, the second of (5.27) is the stricter condition. Thus the detuning must be positive ($\omega > 0$) for stability of the wobble-free bridge! This asymmetry appears whenever $\alpha = 0$ is chosen, and leads us to believe that $\alpha = 0$ is nonphysical. (It weirdly implies that the bridge is stable when driven at frequencies *above* its natural frequency, but would be unstable for driving below its natural frequency.)

In dimensional variables, the stricter condition is

$$\Omega - \Omega_0 > \frac{NGC}{2B\Omega_0} \ , \tag{5.29}$$

or

$$\Omega - \Omega_0 > \frac{NGC}{4\zeta K} \ . \tag{5.30}$$

5.3   Stability of the In-Phase State for Identical Walkers

To evaluate stability of the in-phase state, we will start with the system (4.45) from Section 4.9.2.

$$
\begin{aligned}
a\dot{\psi} &= -\frac{1}{2}\langle\cos(\phi_i + \alpha)\rangle, \\
\dot{a} &= \frac{1}{2}\langle\sin(\phi_i + \alpha)\rangle - ba, \\
\dot{\phi_i} &= \omega - q - a\sin(\phi_i), \qquad i = 1\ldots N \ .
\end{aligned}
\tag{5.31}
$$

We will take $\omega = \omega_i$ as a constant, rather than a distribution, since the walkers are assumed identical. That means that the entire population must be locked, and there are no drifting oscillators.

Recall that q is defined as the locked system frequency (4.44), so $\dot{a} = \dot{\phi} = 0$ and $\dot{\psi} = q$ in (5.31).

We take the variation about the fully locked state,

$$\dot{\delta\psi} = \frac{1}{2a} \sin(\phi^* + \alpha) \langle \delta\phi_i \rangle + \frac{1}{2a^2} \cos(\phi^* + \alpha)(\delta a),$$

$$\dot{\delta a} = \frac{1}{2} \cos(\phi^* + \alpha) \langle \delta\phi_i \rangle - b(\delta a),$$

$$\dot{\delta\phi_i} = -a \cos\phi^*(\delta\phi_i) - \sin\phi^*(\delta a) . \tag{5.32}$$

But for the fully locked state, we can get the value of the sines and cosines in (5.32) by setting $\dot{a} = 0$ and $\dot{\psi} = q$ in (5.31): $\sin(\phi^* + \alpha) = 2ba$ and $\cos(\phi^* + \alpha) = -2qa$ (in the fully locked state, $\sin(\phi^* + \alpha) = \langle \sin(\phi_i + \alpha) \rangle$, and similarly for cosine). From those, we find $\sin\phi^* = 2ba\cos\alpha + 2qa\sin\alpha$ and $\cos\phi^* = 2ba\sin\alpha - 2qa\cos\alpha$. So (5.32) becomes

$$\dot{\delta\psi} = b \langle \delta\phi_i \rangle - \frac{q}{a}(\delta a),$$

$$\dot{\delta a} = -qa \langle \delta\phi_i \rangle - b(\delta a),$$

$$\dot{\delta\phi_i} = -a \left[2ba\sin\alpha - 2qa\cos\alpha \right] (\delta\phi_i) - \left[2ba\cos\alpha + 2qa\sin\alpha \right] (\delta a) . \tag{5.33}$$

This is an $N + 2$ dimensional linear system, yet we can find its characteristic equation with a straightforward transformation as follows.

To decouple this linear system as much as possible, we change variables, with

$$d_i = \delta\phi_{i+1} - \delta\phi_i , \qquad i = 1, \ldots, N - 1 .$$

Note that there are only $N - 1$ equations here, since one has been lost in the differencing.

Then

$$\dot{d_i} = -2a^2 \left(b\sin\alpha - q\cos\alpha \right) (d_i) . \tag{5.34}$$

Equation (5.34) implies a necessary condition for stability of the fully-locked state. In order to prevent perturbations in d_i from growing, the coefficient on the

right hand side must be negative; hence

$$b \sin \alpha > q \cos \alpha \ . \tag{5.35}$$

This condition is always satisfied when $\alpha = \pi/2$, since the dimensionless damping b must be positive. When $\alpha = 0$, it is satisfied only for negative q.

We can get one more equation from (5.33) by averaging the $\dot{\phi}_i$ equation over all oscillators, thus obtaining a system ready for stability calculations:

$$\delta\dot{\psi} = b \langle\delta\phi\rangle - \frac{q}{a}(\delta a),$$

$$\delta\dot{a} = -qa \langle\delta\phi\rangle - b(\delta a),$$

$$\left\langle\delta\dot{\phi}\right\rangle = -2a^2 \left[b \sin\alpha - q \cos\alpha\right] \langle\delta\phi\rangle - 2a \left[b \cos\alpha + q \sin\alpha\right](\delta a) \ , \tag{5.36}$$

where $\langle\delta\phi\rangle = N^{-1} \sum_{i=1}^{N} \delta\phi_i$. Note that the equation for $\delta\dot{\psi}$ above is driven by the other two variables, but $\delta\psi$ itself does not appear on the right hand side of any equation.

Now we can write down the Jacobian matrix for the system in only two dimensions (corresponding to the perturbations δa and $\langle\delta\phi\rangle$) as:

$$\begin{bmatrix} -b & -qa \\ -2a \left(b \cos\alpha + q \sin\alpha\right) & -2a^2 \left(b \sin\alpha - q \cos\alpha\right) \end{bmatrix} \ . \tag{5.37}$$

The characteristic polynomial is

$$\lambda^2 + \left[b + 2a^2 \left(b \sin\alpha - q \cos\alpha\right)\right] \lambda + 2a^2 \left[(b^2 - q^2) \sin\alpha - 2qb \cos\alpha\right] = 0 \ . \tag{5.38}$$

We can comment on the stability in a few special cases.

Special Case $\alpha = 0$

If $\alpha = 0$, then the characteristic polynomial becomes

$$\lambda^2 + (b - 2qa^2)\lambda - 4qba^2 = 0 \ . \tag{5.39}$$

The roots of this equation are

$$\lambda = (qa^2 - b/2) \pm \sqrt{(qa^2 - b/2)^2 + 4qba^2} \ . \tag{5.40}$$

If $q < 0$, then the quantity under the radical will be smaller in magnitude than the quantity outside it, and the eigenvalues will both be negative (so the in-phase state will be stable).

If $q > 0$, then there are two possibilities. In the first case, the quantity outside the radical $(qa^2 - b/2) > 0$. Then at least one eigenvalue must clearly be positive. In the second case, the quantity $(qa^2 - b/2) < 0$, but even then the magnitude of the radical will be greater than that of the quantity outside of it. One eigenvalue will look like $-|C_1| + \sqrt{|C_1|^2 + |C_2|}$, which must necessarily be positive. So in both cases, there is an eigenvalue in the right half plane, and the in-phase state is unstable.

This agrees with Equation (5.35), from which we can directly get the stability condition

$$q < 0 \ . \tag{5.41}$$

The self-consistency equations with $\alpha = 0$, from (4.59), become

$$2qa = -\langle \cos \phi_j \rangle$$

$$2ba = \langle \sin \phi_j \rangle \ . \tag{5.42}$$

We know that $\langle \cos \phi_j \rangle = \cos \phi^*$ and $\langle \sin \phi_j \rangle = \sin \phi^*$ since we have assumed a fully locked state. From (4.57), we see that $\sin \phi^* = (\omega - q)/a$ and that $\cos \phi^* = (1 - \sin^2 \phi^*)^{1/2}$. Plugging those expressions into the first self-consistency equation,

along with $q_c = 0$, tells us that

$$0 = -\sqrt{1 - \frac{\omega^2}{a^2}},$$

$$\omega_c^2 = a^2,$$

$$|\omega_c| = a ,$$

since we know that $a > 0$. So there exist solutions with $q < 0$ for all $|\omega| < a$.

Applying that critical value to the second equation in (5.42), we get:

$$2ba = \frac{\omega - q}{a},$$

$$2b_c = \frac{\omega}{a^2},$$

$$2b_c = \frac{\omega}{|\omega|^2},$$

$$b_c = \frac{1}{2\omega} . \tag{5.43}$$

Writing this in terms of the inverse (which is proportional to $\sqrt{N}$),

$$b_c^{-1} = 2\omega . \tag{5.44}$$

.

Figure 5.1 plots the regions of stability for the in-phase state with $\alpha = 0$. This state will be stable for all $b^{-1} > b_c^{-1}$, but because $b^{-1} > 0$ for physical reasons, the in-phase state must be stable for all negative ω!

Remember that this odd result only holds when $\alpha = 0$. Again, it seems unlikely that this is physically appropriate because of the strong asymmetry between positive and negative detunings.

Special Case $\alpha = \pi/2$

If $\alpha = \pi/2$, then the characteristic polynomial becomes

$$\lambda^2 + b(1 + 2a^2)\lambda + 2a^2(b^2 - q^2) = 0 . \tag{5.45}$$
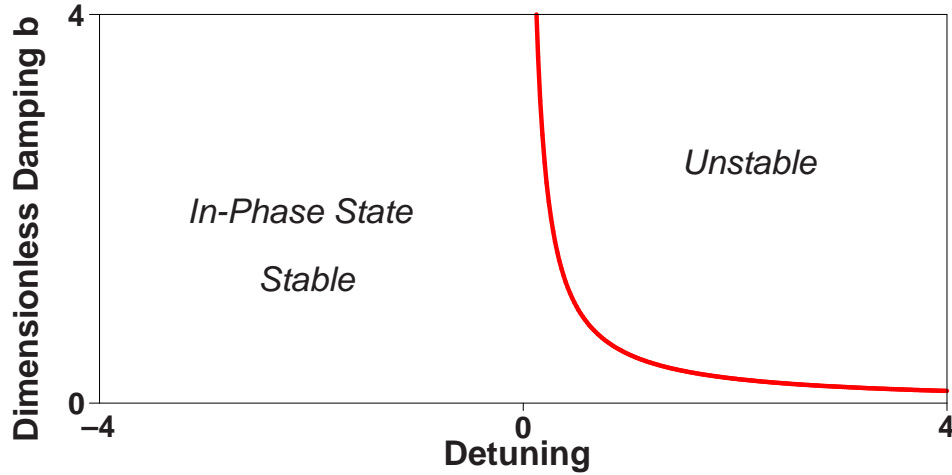
Figure 5.1: The regions in which the in-phase state is stable, for $\alpha = 0$ with identical oscillators $\omega_i = \omega$.

The roots are

$$\lambda = -b(a^2 + \frac{1}{2}) \pm \sqrt{b^2(a^2 + \frac{1}{2})^2 - 2a^2(b^2 - q^2)} \ . \tag{5.46}$$

We observe that the real part of both roots for λ will be negative when the magnitude of the quantity under the radical is less than the magnitude of the quantity outside the radical, since that quantity $-b(a^2 + \frac{1}{2})$ is itself negative. The magnitude within the radical will be determined by the sign of $b^2 - q^2$: when it's positive, the in-phase state must be stable; when it's negative, the in-phase state must be unstable. So the critical condition is

$$|q| < b \ . \tag{5.47}$$

The self-consistency equations with $\alpha = \pi/2$, from (4.59), become

$$2qa = \langle \sin \phi_j \rangle$$

$$2ba = \langle \cos \phi_j \rangle \ . \tag{5.48}$$

We know that $\langle \cos \phi_j \rangle = \cos \phi^*$ and $\langle \sin \phi_j \rangle = \sin \phi^*$ since we have assumed a fully locked state. From (4.57), we see that $\sin \phi^* = (\omega - q)/a$ and that $\cos \phi^* =$

$(1 - \sin^2 \phi^*)^{1/2}$. Plugging those expressions into the first self-consistency equation, along with $q_c = \pm b$, tells us that

$$
\begin{aligned}
2qa &= \frac{\omega - q}{a}, \\
a^2 &= \frac{\omega - q}{2q}, \\
a_c^2 &= \frac{\omega \mp b}{\pm 2b}, \\
&= \frac{\pm \omega - b}{2b} \ .
\end{aligned}
\tag{5.49}
$$

Using this critical value for a in the second self-consistency equation,

$$
\begin{aligned}
2ba &= \left[1 - \frac{(\omega - q)^2}{a^2} \right]^{\frac{1}{2}}, \\
4b^2 a^2 &= 1 - \frac{(\omega - q)^2}{a^2}, \\
4b_c^2 \frac{\pm \omega - b_c}{2b_c} &= 1 - \frac{(\omega - \pm b_c)^2}{\pm \omega - b_c} 2b_c, \\
2b_c(\pm \omega - b_c) &= 1 - 2b_c(\pm \omega - b_c), \\
4b_c(\pm \omega - b_c) &= 1, \\
\pm \omega &= \frac{1}{4b_c} + b_c, \\
\omega &= \pm \left(\frac{1}{4b_c} + b_c \right) \ .
\end{aligned}
\tag{5.50}
$$

This equation is implicit for b_c, although we could easily solve for the explicit branches which are roots of a quadratic equation (they are $2b_c = \pm \omega \pm \sqrt{\omega^2 - 1}$). We plot the function to show the regions in which the in-phase state is stable in Figure 5.2.

We can look at the limiting behavior for large detuning. In that case, the upper branches have formulas

$$
2b_c = |\omega| + \sqrt{\omega^2 - 1} \ ,
\tag{5.51}
$$
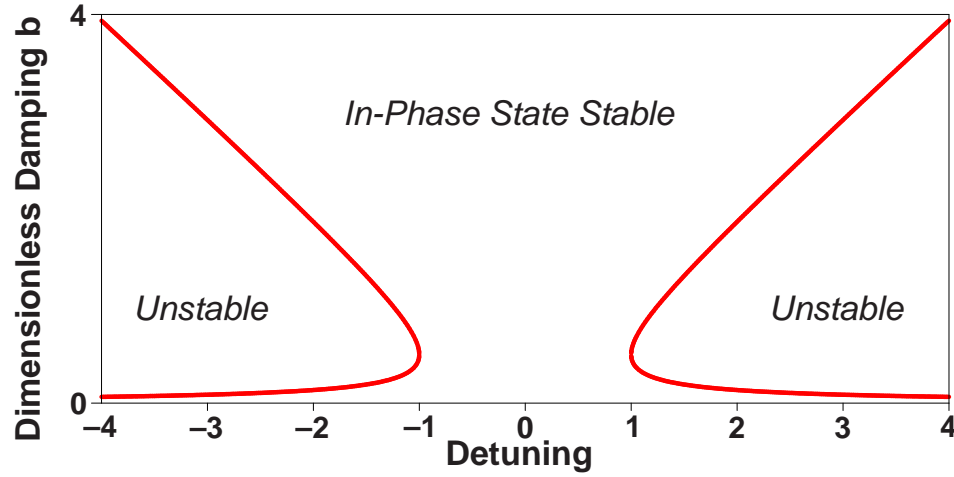
Figure 5.2: The regions in which the in-phase state is stable, for $\alpha = \pi/2$ with identical oscillators $\omega_i = \omega$.

and the lower branches have formulas

$$2b_c = |\omega| - \sqrt{\omega^2 - 1} \ . \tag{5.52}$$

As $|\omega| \to \infty$, the two formulas limit to

$$b_c \sim |\omega| \ , \tag{5.53}$$

and

$$b_c \sim \frac{1}{4|\omega|} \ . \tag{5.54}$$

We hope that these asymptotic formulas will have some applicability even when the distribution $g(\omega)$ has finite width, rather than the Dirac delta function assumed earlier for $g(\omega)$.

5.4 Noisy Identical Walkers

This case will be examined under the following simplifying assumptions:

- $C = $ constant

- $\alpha = \pi/2$

- $\omega_i = \omega = 0$ is a constant, the same for all oscillators, so walkers are identical and there is no detuning (forcing is on resonance).

- White noise in walker angular frequencies with variance $2D$, so $E(\xi_i) = 0$ and $E(\xi_i(T_1)\xi_j(T_2)) = 2D\delta_{ij}\delta(T_1 - T_2)$.

Under these assumptions, the slow-time system (4.37) becomes

$$\begin{aligned}
a\dot{\psi} &= -\frac{1}{2}\langle\cos(\theta_i - \psi)\rangle, \\
\dot{a} &= \frac{1}{2}\langle\sin(\theta_i - \psi)\rangle - ba, \\
\dot{\theta}_i &= \xi_i + a\cos(\psi - \theta_i), \qquad i = 1\ldots N.
\end{aligned}$$

(5.55)

Taking the continuum limit (see Section 4.9.3), the density of oscillators $\rho(\theta, T)$ will now obey a Fokker-Planck equation rather than the simple continuity equation as before in (4.50),

$$\frac{\partial\rho}{\partial T} = -\frac{\partial}{\partial\theta}(\rho v) + D\frac{\partial^2\rho}{\partial\theta^2},$$

(5.56)

where $v(\theta, T) = a\cos(\psi - \theta)$ is given by the continuum limit of the equation for $\dot{\theta}_i$ in (5.55) (leaving out the noise term which is already incorporated into the Fokker-Planck equation).

We will seek stationary solutions with $\dot{a} = 0$, $\dot{\rho} = 0$, and $\dot{\psi} = q$. We'll also change to a rotating frame as done above in Section 4.9.1, choosing $\psi(T = 0) = -\pi/2$. So the change of variables from θ to ϕ is

$$\begin{aligned}
\psi &= qT - \pi/2, \\
\theta &= qT + \phi,
\end{aligned}$$

(5.57)

and $v(\phi, T) = a\cos(-\pi/2 - \phi) = -a\sin\phi$.

Integrating both sides with respect to ϕ in (5.56) gives

$$\text{constant} = -\rho v + D\frac{d\rho}{d\phi} \ , \tag{5.58}$$

where the partial derivative has been replaced by a full derivative since ρ is no longer a function of any variable but ϕ.

We take the constant in (5.58) to be zero, and we will show that the valid solutions which emerge under that assumption have the desired properties. So the simplified Fokker-Planck equation becomes

$$\rho v = D\frac{d\rho}{d\phi} \ , \tag{5.59}$$

and the continuum self-consistency equations are

$$qa = \frac{1}{2}\oint \sin\phi \rho(\phi)d\phi,$$
$$ba = \frac{1}{2}\oint \cos\phi \rho(\phi)d\phi \ . \tag{5.60}$$

Equation (5.59) is separable, as

$$D\frac{d\rho}{\rho} = v(\phi)d\phi,$$
$$= -a\sin(\phi)d\phi \ , \tag{5.61}$$

and we integrate both sides to get

$$D\ln\rho + \text{constant} = a\cos\phi,$$
$$\ln\rho = \frac{a}{D}\cos\phi + \text{constant},$$
$$\rho = [\text{constant}]e^{a\cos\phi/D} \ . \tag{5.62}$$

The constant can be determined from the normalization condition $\oint \rho d\phi = 1$ to get

$$\rho(\phi) = \frac{\exp\left(\frac{a}{D}\cos\phi\right)}{\oint \exp\left(\frac{a}{D}\cos\phi\right)d\phi} \ . \tag{5.63}$$

Dimensionless Amplitude a Versus Slow-Time Noise Variance D
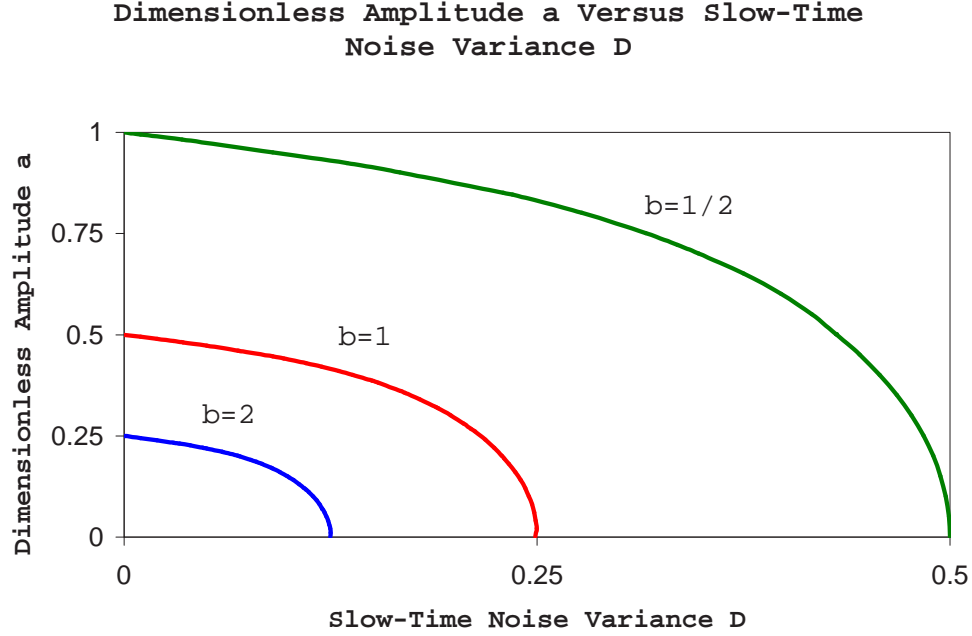
Figure 5.3: Dimensionless amplitude a versus slow-time noise variance D for three different values of dimensionless damping b. See Equation (5.65).

The denominator is a multiple of the 0th order modified Bessel function of the first kind $I_0(a/D)$, so ρ becomes

$$\rho(\phi) = \frac{\exp\left(\frac{a}{D}\cos\phi\right)}{2\pi I_0(a/D)} \ . \tag{5.64}$$

Since $\rho(\phi)$ is an even function in ϕ, the integral in the first equation of (5.60) must be zero, leading to the condition that $q = 0$.

Looking at the second equation of (5.60), we get

$$
\begin{aligned}
ba &= \frac{1}{2} \oint \cos\phi \frac{\exp\left(\frac{a}{D}\cos\phi\right)}{2\pi I_0(a/D)} d\phi, \\
b &= \frac{1}{4\pi a I_0(a/D)} \oint \cos\phi \exp\left(\frac{a}{D}\cos\phi\right) d\phi \ .
\end{aligned}
\tag{5.65}
$$

Figures 5.3, 5.4, and 5.5 show several aspects of the behavior of this equation.
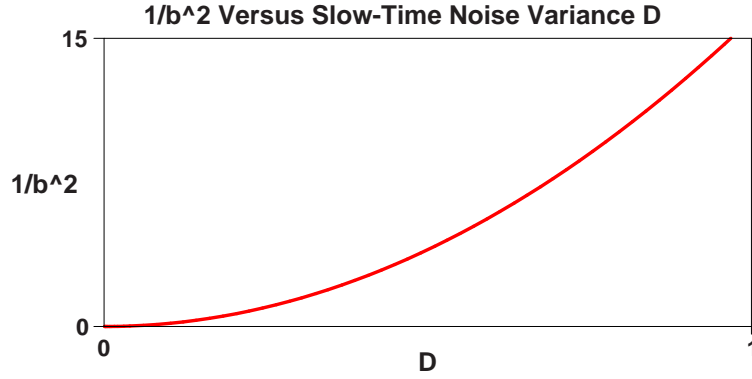
Figure 5.4: The quantity b^{-2} (proportional to N_c) is plotted as a function of the slow-time noise variance D in the small a limit. Taylor expansion in Equation (5.65) can be used to show that $b^{-2} \approx 16D^2$ for $a \ll D$.
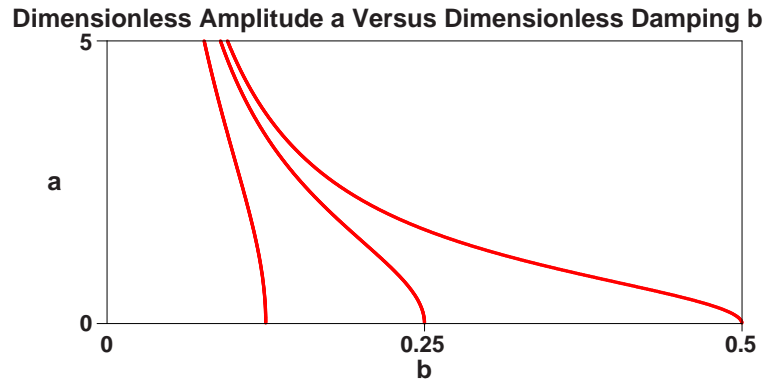
Figure 5.5: Dimensionless amplitude a is plotted as a function of dimensionless damping b for $D = \frac{1}{2}$ (rightmost), $D = 1$ (center), and $D = 2$ (leftmost). See Equation (5.65).

Small a

Now we're ready to look at the behavior of the solutions to the self-consistency equation (5.65) as $a \to 0^+$, with the hope of finding the critical value b_c at which the wobbling state is born in the presence of noise.

We expand $I_0(a/D)$ in a Taylor series for small a, and also expand the integrand to get

$$b \approx \frac{1}{4\pi a \left(1 + (a/D)^2 + \mathcal{O}\left(a^4\right)\right)} \oint \left[\cos \phi + \frac{a}{D} \cos^2 \phi + \mathcal{O}\left(a^2\right)\right] d\phi . \qquad (5.66)$$

So to first order,

$$b_c = \frac{1}{4D}. \tag{5.67}$$

We can also express this as a critical level of noise above which it is not possible to have synchronous excitation of the bridge. In that case,

$$D_c = \frac{1}{4b}. \tag{5.68}$$

Converting back to Dimensional Variables

It is straightforward to convert b back to dimensional variables with the use of the definitions (4.12) and (4.8). However, we must also convert the white noise variance $2D$ to dimensional variables, since this variance is based on the slow-time system.

To do so, we examine the equation for $\dot{\theta}_i$ in (5.55) above. Recall from Section 4.7.2 that an overdot indicates derivative with respect to slow time T. So, using (4.17) and (4.8), we can write

$$\begin{aligned}
\frac{d\theta_i}{dt} &= \frac{d\theta_i}{dT}\frac{dT}{dt} \\
&= \epsilon\Omega_0\left[\xi_i + a\cos(\psi - \theta_i)\right] . \tag{5.69}
\end{aligned}$$

The dimensional quantity corresponding to the variance of the noise would be the variance in the autocorrelation of the walker angular velocities $\frac{d\theta_i}{dt}$. That autocorrelation is

$$\begin{aligned}
E\left(\frac{d\theta_i}{dt}(t_1)\frac{d\theta_i}{dt}(t_2)\right) &= \epsilon^2\Omega_0^2 E(\xi_i(t_1)\xi_i(t_2)), \\
&= 2\epsilon^2\Omega_0^2 D\delta(t_1 - t_2) . \tag{5.70}
\end{aligned}$$

The amplitude of the quantity is measurable, and we'll call it σ_n^2 (short for σ_{noise}), with the definition

$$\sigma_n^2 = 2\epsilon^2\Omega_0^2 D . \tag{5.71}$$

So now we can insert all the dimensional quantities into Equation (5.67) to obtain a formula for the critical number of walkers N_c in the presence of white noise with variance σ_n^2 in the walker angular frequencies:

$$
\begin{aligned}
b_c &= \frac{1}{4D} \\
\zeta/\epsilon &= \frac{2\epsilon^2 \Omega_0^2}{4\sigma_n^2} \\
\epsilon^3 &= \frac{2\sigma_n^2 \zeta}{\Omega_0^2} \\
\epsilon^3 &= \frac{\sigma_n^2 B}{K\Omega_0} \\
\left(\frac{N_c GC}{K\Omega_0}\right)^{3/2} &= \frac{\sigma_n^2 B}{K\Omega_0} \\
N_c &= \sigma_n^{4/3} B^{2/3} K^{1/3} \Omega_0^{1/3} G^{-1} C^{-1} .
\end{aligned}
\tag{5.72}
$$

This can also be expressed in terms of ζ as $N_c = 2^{2/3} K \sigma_n^{4/3} \zeta^{2/3} \Omega_0^{-1/3} G^{-1} C^{-1}$.

The main conclusion is that when noise is present, even a bridge driven exactly on resonance by identical walkers will have a nonzero value for N_c.

CHAPTER 6

NUMERICAL SIMULATIONS OF MILLENNIUM BRIDGE

MODELS

During the course of research on this topic, we wrote two separate programs to numerically simulate the behavior of our various models of the Millennium Bridge. The first program was used to simulate the full set of equations presented in Sections 4.1 and 4.2 of Chapter 4. Relevant information is presented in Section 6.1. The second program simulates only the system of slow-time equations (4.37) obtained via perturbation theory in Section 4.7.2. Details of that code are presented in Section 6.2 below.

6.1   Simulation of the Full Model

The code to simulate the full model of the Millennium Bridge was written in C/C++, that language being chosen mainly to maximize speed of computation.

It evolved through nine separate versions, from March of 2005 through February of 2006. The final version was a fairly flexible program capable of simulating a variety of different aspects of the problem, controlled mainly through a set of predefined constants in the program header.

A plot of typical program output (filtered through Matlab's graphical routines) is show in Figure 6.1.

Program execution begins with initialization of parameters.

1. Choose the maximum number of walkers on the bridge, and set the function determining the number of walkers versus time, $N(t)$.

2. Initialize seed for pseudo-random number generator to user-selected constant RANDSEED.
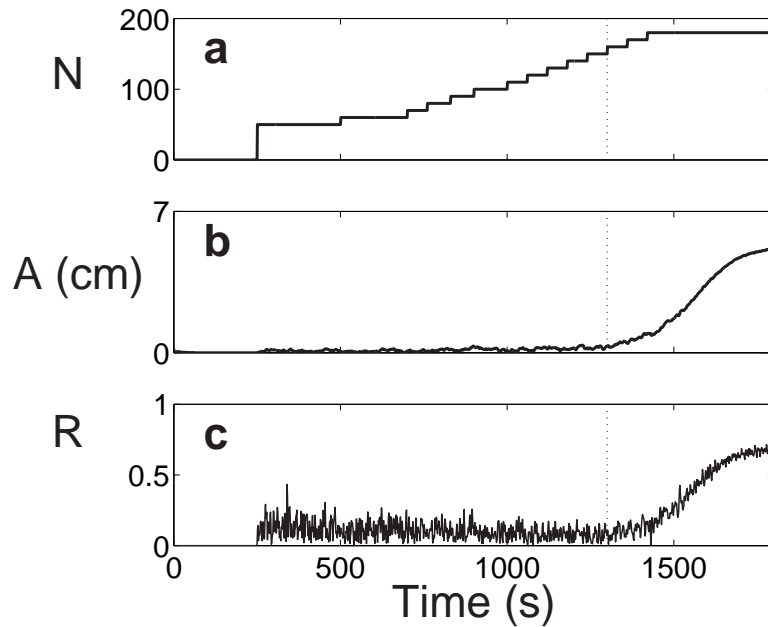
Figure 6.1: A typical plot of the output from a simulation of the full model (4.6) with varying N. The top panel shows the number of walkers on the bridge as a function of time, the middle panel shows the amplitude of vibration in centimeters versus time, and the bottom panel shows the degree of of phase-synchronization among the population (the order parameter magnitude) as a function of time. In this case G was taken to be a constant independent of A, $C = 16$, $\alpha = \pi/2$ and all of the constants relevant to the north span of the bridge were used. $P(\Omega)$ was taken to be Gaussian with mean $\overline{\Omega} = 1.03Hz$ and standard deviation $\sigma_\Omega = 0.1Hz$. Compare this graph to Arup's published data in Figure 2.9.

3. Set values for α, G^1, M, ζ, and Ω_0.

4. Calculate implied values of B and K.

5. Choose the distribution of pedestrian frequencies from several implemented candidates: constant, uniform, randomly sampled Lorentzian, uniformly sampled Lorentzian, randomly sampled Gaussian, uniformly sampled Gaussian. See Section 6.1.2 for more about this.

6. Specify the distribution mean $\overline{\Omega}$ and the width for the given distribution.

---

[1]See section 6.1.1.

The width is interpreted as half the FWHM[2] for a Lorentzian, the standard deviation for a Gaussian, the full width for uniform, and is ignored for a constant Ω distribution.

7. Set the initial condition of the bridge, specifying both position X and velocity $\frac{dX}{dt}$.

8. Specify the sensitivities C_i for each pedestrian. In practice, these were almost always set to a single constant value.

9. Choose the type of initial condition for the walkers, from a choice of uniform, in-phase, or random. See Section 6.1.3 for more about this.

10. Specify the total integration time, and the interval at which data should be printed to the output files.

11. Prepare output files.

After this initialization is complete, the complete set of chosen parameters are written to the header of the output data file. A timer is started, and numerical integration of the system begins.

Equations to Integrate

The system to be integrated is defined by two functions of the current state, namely $\frac{d^2X}{dt^2}$, and $\frac{d\Theta_i}{dt}$. We used formulas in accordance with our system as described in 4.1 and 4.2. However, the intuitive variables A and Ψ are not well-defined outside of

---

[2]Full Width at Half Maximum

steady-state behavior, so we define them as described in [23]:

$$
\begin{aligned}
X &= A \sin \Psi, \\
\frac{dX}{dt} &= \Omega_0 A \cos \Psi \ .
\end{aligned}
\tag{6.1}
$$

We converted our formulas to a system of first order equations by introducing the dummy variable dXdT. Thus our formulas for numerical integration became

$$
\frac{dX}{dt} = \text{dXdT},
\tag{6.2}
$$

$$
\frac{d(\text{dXdT})}{dt} = \frac{1}{M} \sum_{i=1}^{N} G(A) \sin \Theta_i - \frac{B}{M} \text{dXdT} - \frac{K}{M} X,
\tag{6.3}
$$

$$
\frac{d\Theta_i}{dt} = \Omega_i + C_i A \sin(\Psi - \Theta_i + \alpha) \ ,
\tag{6.4}
$$

but we want to replace the explicit appearance of A and Ψ using the definitions (6.1). So we plug in for A in the second equation, and we expand the sine function in the third equation to get:

$$
\frac{dX}{dt} = \text{dXdT},
\tag{6.5}
$$

$$
\frac{d(\text{dXdT})}{dt} = \frac{1}{M} \sum_{i=1}^{N} G\left(X^2 + \frac{\text{dXdT}^2}{\Omega_0^2}\right) \sin \Theta_i - \frac{B}{M} \text{dXdT} - \frac{K}{M} X,
\tag{6.6}
$$

$$
\frac{d\Theta_i}{dt} = \Omega_i + C_i \left[X \cos(\Theta_i - \alpha) - \frac{\text{dXdT}}{\Omega_0} \sin(\Theta_i - \alpha)\right] \ .
\tag{6.7}
$$

These are the equations that were actually integrated, although the function $G(A)$ was often replaced by a value G to speed up program execution when the effects of changing gait were not being considered.

Numerical Integration Procedure

During numerical integration, state variables are written to the output data file and the terminal screen at each "print-interval" specified by the user. However, other activity takes place even during the intervals between file output.

- A mean value of the order parameter R is updated after each full integration step (this is the mean for the current print-interval only).

- A mean value of the bridge amplitude A is updated after each full integration step (this is the mean for the current print-interval only).

- A routine is called to check for a peak in either the total pedestrian force F_{ped} or the current bridge velocity $\frac{dX}{dt}$. If a peak is detected, the value is written to the relevant data file buffer[3] (data files of peak pedestrian force versus peak bridge velocity were used to test Arup's observations of linearity in those variables - see Section 3.2).

After the specified ending time for numerical integration is reached, the program calculates total run-time and terminates.

Numerical Method

The numerical integration at the heart of this simulation is a straightforward fixed time step implementation of the well-known Runge-Kutta routine. It was implemented to fourth order, and accuracy was verified by two methods:

- The first verification method was simply a test that code was correctly written. I integrated an ODE with a known solution (a simple harmonic oscillator) in order to make sure that the correct result was produced.

- In the second verification method, I repeatedly integrated the full system with an increasing time step until numerical errors became detectable. I then returned the time step to half that critical value for all subsequent

---

[3]To increase program execution speed, buffers are not flushed until the end of the current print-interval.
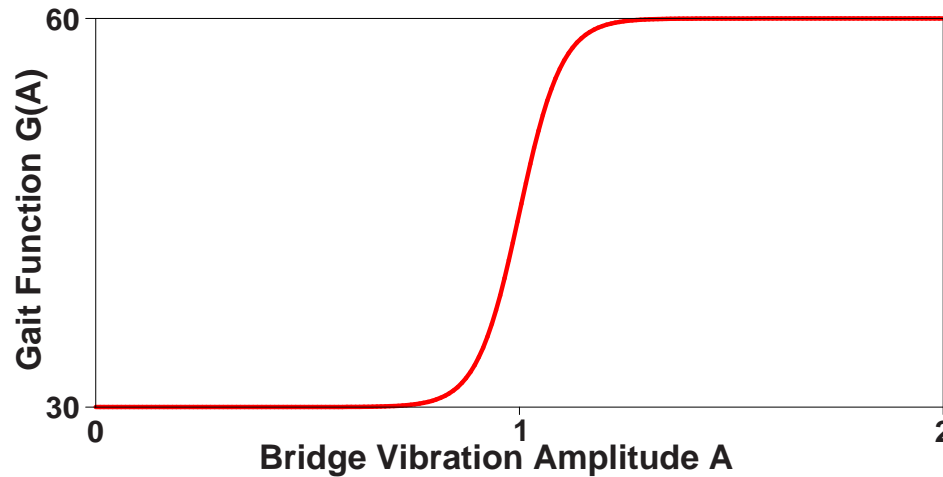
Figure 6.2: A typical plot showing the shape of a curve defined by Equation (6.8). Here $G_{low} = 30$, $G_{high} = 60$, $C_1 = 1$, and $C_2 = 10$.

calculations. This process was repeated whenever significant changes to the code were introduced.

6.1.1   Pedestrian Forcing

Although not used for most simulations, the program allows for the pedestrian forcing amplitude to vary with amplitude of bridge motion A. The specific formula implemented for this purpose is

$$G(A) = \frac{1}{2}(G_{low} + G_{high}) + \frac{1}{2}(G_{high} - G_{low}) \tanh\left(C_2(A - C_1)\right) , \qquad (6.8)$$

where G_{low}, G_{high}, C_1 and C_2 are constants provided by the user. They determine, respectively, the minimum and maximum forcing amplitude (in Newtons), the amplitude at which forcing increases, and the rate at which forcing increases with oscillation amplitude. The general shape of this curve is shown in Figure 6.2.

This model of pedestrian forcing was motivated by experiments conducted by Allan McRobie [16], as well as comments by pedestrians that had been on the bridge during opening day (some of which have been presented in an episode of

the BBC's "Science Shack"). Both observed that the amplitude of lateral forcing by pedestrians can increase dramatically when they change their gait on a moving platform—hence the use of G for "gait function".

Nevertheless, we did not use this effect in most simulations because it proved to be of secondary importance. It will affect the steady-state amplitude of the bridge motion and the speed at which oscillation builds up, but it should not affect the critical number of pedestrians for onset of motion, or the qualitative behavior of the bridge-crowd system.

6.1.2   Distributions for Ω_i

We implemented six different distributions for Ω_i, although in practice we rarely used four of these. For each distribution, I'll give the probability distribution function $P(\Omega)$ and the corresponding formula used to calculate Ω_i. In the actual C code, arrays were indexed from $0 \ldots N - 1$, but to avoid confusion I will present them here as $1 \ldots N$.

- **Constant:**

$$
\begin{aligned}
P(\Omega) &= \delta(\Omega - \overline{\Omega}), \\
\Omega_i &= \overline{\Omega} \, .
\end{aligned}
$$

- **Uniform:**

$$
\begin{aligned}
P(\Omega) &= W^{-1}\mathrm{Hat}(\overline{\Omega} - W/2, \overline{\Omega} + W/2), \\
\Omega_i &= \overline{\Omega} + \left(\frac{i - 1}{N - 1} - \frac{1}{2} \right) W \, .
\end{aligned}
$$

- **Randomly Sampled Lorentzian:**

$$P(\Omega) = \frac{1}{\pi}\frac{W}{(\Omega - \overline{\Omega})^2 + W^2},$$
$$\Omega_i = \overline{\Omega} + W\tan(\pi\xi_i)\;.$$

- **Uniformly Sampled Lorentzian:**

$$P(\Omega) = \frac{1}{\pi}\frac{W}{(\Omega - \overline{\Omega})^2 + W^2},$$
$$\Omega_i = \overline{\Omega} + W\tan\left(\pi\frac{i}{N+1}\right)\;.$$

- **Randomly Sampled Gaussian:**

$$P(\Omega) = \frac{1}{W\sqrt{2\pi}}\exp\left[-(\Omega - \overline{\Omega})^2/2W^2\right],$$
$$\Omega_i = \overline{\Omega} + W\,\mathrm{BoxMuller}(\xi_i, \chi_i)\;.$$

- **Uniformly Sampled Gaussian:**

$$P(\Omega) = \frac{1}{W\sqrt{2\pi}}\exp\left[-(\Omega - \overline{\Omega})^2/2W^2\right],$$
$$\Omega_i = \overline{\Omega} + W\,\mathrm{NumiCDF}(i/(N+1))\;.$$

In the above, ξ_i and χ_i represent uniform random variable on $[0, 1)$. Note that there is a finite but nonzero probability of numerical error if $\xi_i = 0.5$ in the tangent function for the Lorentzian.

After the assignment of all Ω_i values, a randomization (by repeated binary swaps) of the indices was done to prevent bias when the order of walkers entering the bridge was important.

Lorentzian Formulas

For a Lorentzian,

$$P(\Omega) = \frac{1}{\pi}\frac{W}{(\Omega - \overline{\Omega})^2 + W^2}\;,$$

where W is the half of the full-width at half maximum. So the CDF is the integral

$$CDF(\Omega) = \frac{1}{2} + \frac{1}{\pi} \arctan\left(\frac{\Omega - \overline{\Omega}}{WS}\right) \ ,$$

and the inverse CDF is

$$iCDF(y) = \overline{\Omega} + W \tan\left[\pi(y - 1/2)\right] \ .$$

For the purposes of random or uniform sampling of the CDF values $y \in (0, 1)$, it makes no difference if we shift the argument of the tangent function by $\pi/2$, as done to obtain the formula used,

$$\Omega_i = \overline{\Omega} + W \tan(\pi\xi_i) \ .$$

Gaussian Formulas

To convert the uniform random variables provided by the C language to Gaussian, I adapted code provided by Dr. Everett Carter, Jr., available at `http://www.taygeta.com/random/gaussian.html` as of July 13, 2006. His code is an efficient implementation of the Box-Muller transformation

$$\begin{aligned} y_1 &= \sqrt{-2\ln(\xi_1)}\cos(2\pi\xi_2), \\ y_2 &= \sqrt{-2\ln(\xi_1)}\sin(2\pi\xi_2) \ , \end{aligned}$$

where ξ_1 and ξ_2 are uniform random variables on $[0, 1)$, and the resulting y_1 and y_2 are Gaussian random variables with zero mean and unit standard deviation.

For the uniform sampling of the inverse CDF of a Gaussian, there is no closed-from solution to work from. Instead, I used a purely numerical implementation of the inverse CDF function originally written in Perl by Peter J. Acklam (see `http://home.online.no/~pjacklam/notes/invnorm/`). The code that I used
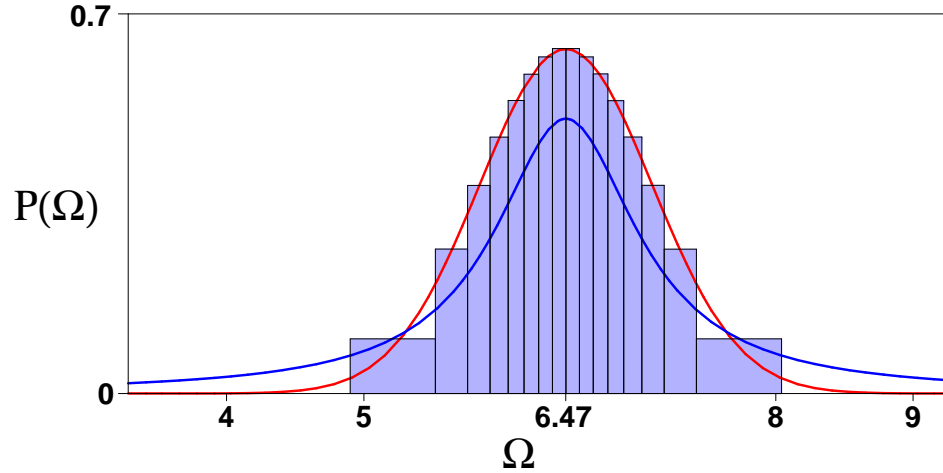
Figure 6.3: A histogram of a Gaussian distribution $P(\Omega)$ with $N = 160$ walkers, $\overline{\Omega} = 6.47\text{rad/s} = 1.03\text{Hz}$, and standard deviation $\sigma_\Omega = 0.1\text{Hz}$. The data comes from a uniformly sampled initial condition for Ω in the Millennium Bridge simulation code. Overlaid are the corresponding Gaussian probability distribution function (blue upper curve), and the PDF for a Lorentzian distribution with half width $\Gamma/2 = \sigma_\Omega = 0.1\text{Hz}$ (red lower curve).

was adapted for C by Chad Sprouse of John Hopkins Applied Physics Lab, and claims a relative error of less than 1.15×10^{-9}. I tested it and found that it produced extremely good agreement with theoretical values.

While I feel a bit guilty about not writing these two sections of code myself, these implementation ran far faster than the code I would have written. I have since written my own versions of these functions for another project, and although my code is much more straightforward, it's perhaps an order of magnitude slower.

Figure 6.3 shows a histogram for a typical Gaussian distribution of Ω values generated by the program.

6.1.3   Initial Distributions for Θ_i

The initial condition for the pedestrians may be set to one of three possibilities: uniform, in-phase, or random. These correspond respectively to a bridge with

maximally asynchronous pedestrians; with maximally synchronous pedestrians, and with a randomly walking crowd. As done in 6.1.2 for distributions of Ω_i values, I'll give the relevant probability distribution function and the implementation for each distribution here.

- **Uniform:**

$$
\begin{aligned}
P(\Theta) &= (2\pi)^{-1}\mathrm{Hat}(0, 2\pi), \\
\Theta_i &= (2\pi)\frac{i-1}{N} + (\xi_i - 1/2)\mathcal{R} .
\end{aligned}
$$

Here $\mathcal{R}$ is a user-defined choice for the level of additive randomness in a uniform initial condition. With no randomness, this forms an exact splay state that may have peculiar properties.

- **In-phase:**

$$
\begin{aligned}
P(\Theta) &= \delta(\Theta - \overline{\Theta}), \\
\Theta_i &= 0.1 + (\xi_i - 1/2)\mathcal{R} .
\end{aligned}
$$

Again $\mathcal{R}$ represents a user-defined choice for the level of additive randomness, this time used to deviate slightly from a perfectly synchronized state. The choice of 0.1 for the phase of the synchronized oscillators was arbitrary.

- **Random:**

$$
\begin{aligned}
P(\Theta) &= (2\pi)^{-1}\mathrm{Hat}(0, 2\pi), \\
\Theta_i &= 2\pi\xi_i .
\end{aligned}
$$

Recall that ξ_i is a uniform random number $\xi \in [0, 1)$.

6.1.4   Noise

As mentioned above in the descriptions of the various distributions, additive noise could be used to start the system in a state very close to fully synchronized or fully incoherent (splay).

We were also able to include any specified noise model in the numerical function for $\frac{d\Theta}{dt}$, although the effect of noise was never thoroughly investigated numerically.

6.2   Simulation of the Slow-Time Equations

The code to simulate the slow-time equations for the Millennium Bridge was written in C/C++, that language being chosen mainly to maximize speed of computation.

By coincidence, it evolved through nine separate versions, the same number as the program for the numerical integration of the full model. Development occurred over a span of time from April through December 2005. Like the full model code, this was intended to be a flexible program for simulation of many aspects of the problem, controlled through a set of predefined constants in the program header.

Program execution begins with initialization of parameters.

1. Initialize seed for pseudo-random number generator to user-selected constant *rseed*.

2. Choose the type of initial condition for the walkers, from a choice of uniform, in-phase, or random. See Section 6.1.3 for more about this.

3. Choose the distribution of pedestrian detunings from several implemented candidates: constant, uniform, randomly sampled Lorentzian, symmetric
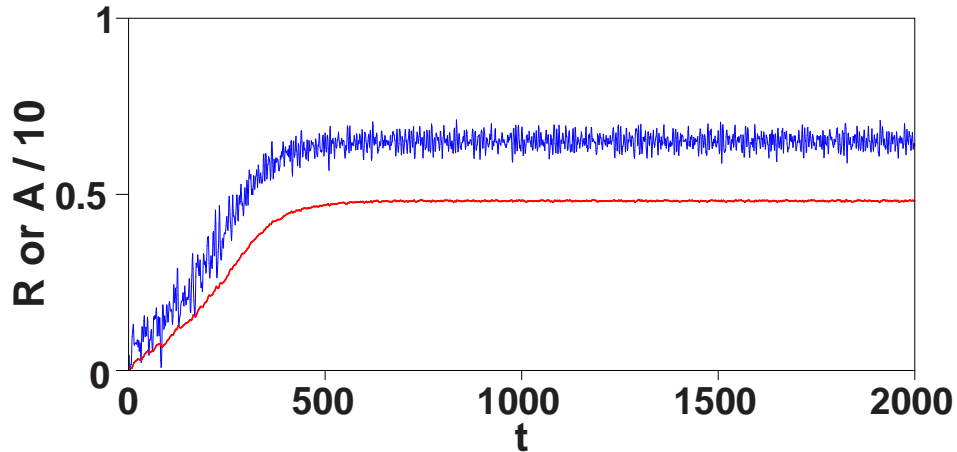
Figure 6.4: A typical plot of the output from a simulation of the full model (4.6). The top trace (blue) shows the amplitude of vibration of the bridge divided by 10 for convenience of display. The lower trace (red) shows the magnitude of the order parameter, a measure of the degree of phase coherence or synchronization among the pedestrians. In this case, $P(\Omega)$ was a Gaussian distribution, $\overline{\Omega} = \Omega_0 = 1.03Hz$, $\sigma_\Omega = 0.1Hz$, $\alpha = \pi/2$, and the rest of the parameters were chosen to match the north span of the Millennium Bridge. There were 175 walkers (the critical number was 160). The integration started from a uniform random incoherent initial condition

randomly sampled Lorentzian, uniformly sampled Lorentzian, randomly sampled Gaussian, uniformly sampled Gaussian. See Section 6.1.2 for the analogous distributions in the full model.

4. Set values for b, and α.

5. Specify the distribution mean $\overline{\omega}$ and the width for the given distribution. The width is interpreted as half the FWHM[4] for a Lorentzian, the standard deviation for a Gaussian, the full width for uniform, and is ignored for a constant ω distribution.

6. Specify the total number of oscillators N_{osc} to use in the simulation. Note that the number of oscillators used is not related to the number of walkers

[4]Full Width at Half Maximum

on the bridge (a function of the choice of b and the bridge parameters). The more oscillators used, the more accurate the program output, and the closer it will be to the continuum limit.

7. Set the initial condition of the bridge by specifying initial dimensionless amplitude and initial phase ψ.

8. Initialize running averages for R and a.

9. Specify the total integration time, and the interval at which data should be printed to the output files.

10. Prepare output files.

After this initialization is complete, the complete set of chosen parameters are written to the header of the output data file. A timer is started, and numerical integration of the system begins.

Equations to Integrate

The system to be integrated is defined by a vector holding the current values of a, ψ, and θ_j, $j = 1 \ldots N_{osc}$. The equations integrated are:

$$\dot{a} = -ba - \frac{1}{2}R\sin(\psi - \Phi),$$

$$\dot{\psi} = -\frac{1}{2}\frac{R}{a}\cos(\psi - \Phi),$$

$$\dot{\theta}_j = \omega_j + a\sin(\psi - \theta_j + \alpha) ,$$

where $R\exp(i\Phi)$ is the complex order parameter in the system, defined as

$$Re^{i\Phi} = \left\langle e^{i\theta_j} \right\rangle_j = N_{osc}^{-1} \sum_{j=1}^{N_{osc}} e^{i\theta_j} . \tag{6.9}$$

This is equivalent to the slow-time system (4.42) written in terms of R and Φ.

Numerical Integration Procedure

During numerical integration, state variables (T,a,R,mean a, mean R, $\dot{\psi}$, $\sin(\Phi - \psi)$) are written to the output data file and the terminal screen at each "print-interval" specified by the user. After each file output, the mean values for R and a are reset, and they are then updated after each full integration step until the next file output.

After the specified ending time for numerical integration is reached, the program calculates total run-time and terminates.

Numerical Method

The numerical integration at the heart of this simulation is a straightforward fixed time step implementation of the well-known Runge-Kutta routine. It was implemented to fourth order, and accuracy was verified by two methods:

- The first verification method was simply a test that code was correctly written. I integrated an ODE with a known solution (a simple harmonic oscillator) in order to make sure that the correct result was produced.

- In the second verification method, I repeatedly integrated the full system with an increasing time step until numerical errors became detectable. I then returned the time step to half that critical value for all subsequent calculations. This process was repeated whenever significant changes to the code were introduced.

6.2.1 Sweeping Parameters

In order to confirm predictions for the dependence of the critical threshold b_c on parameters such as detuning ($\overline{\omega}$), width of $g(\omega)$, and lag α, I created routines that would automatically vary these parameters while looking for a transition in the steady state system behavior. Altogether, six similar routines were created:

- SweepDetuningDown

- SweepDetuningUp

- SweepWidthDown

- SweepWidthUp

- SweepLagDown

- SweepLagUp

The "Up" or "Down" tag attached to the end of the routine name indicates the direction of variation for the variable $binv$, b^{-1}, which is proportional to $\sqrt{N}$.

Each of the routines functions in a similar manner. As an example, I'll describe *SweepDetuningDown* in detail.

Initially, the range over which detuning is to be varied is hard-coded into the procedure. $\overline{\omega}$ is set to the maximum value in that range, and *binv* is started at a value much bigger than the suspected threshold. The system is then initialized using either the in-phase or incoherent state, as specified, and numerically integrated until a steady state is detected (see below). It was necessary to include a maximum integration time due to the extremely long transients in some cases (see Section 4.11).

After a steady state was detected, it was compared with the expected steady state for large $binv$, i.e. the in-phase state. If the system did not detect a change to the incoherent state, then $binv$ was decreased by a constant step size $binvstep$, the numerics were reset, and the process began anew.

When a transition to the incoherent state was finally detected, the detuning value $\overline{\omega}$ was decreased by a constant step size $\overline{\omega}step$ and $binv$ was reset.

To decrease the run-time of the sweep, assumptions were usually made about the general shape of the threshold curve. In the case of detuning, it was assumed that $binv_{crit}$ was an increasing function of the detuning $\overline{\omega}$. Thus, rather than reset $binv$ to a constant maximum, it was reset to the threshold value just discovered, with a small margin added for numerical stability. To put it another way, the expected threshold for the new, smaller detuning was smaller than the threshold $binv$ just discovered, so why not start from the current threshold value and step downward from there?

The sweep ended when detuning reached its minimum specified value, in this case 0.0. During the course of the sweep, state information was written to an output data file each time a steady-state was detected.

Downward sweeps such as that described always started from the in-phase state, since it was expected to be stable for large $binv$. Thus, they detected the value $binv_{crit1}$ at which the in-phase state lost stability. Conversely, upward sweeps started from the incoherent state since it should have been stable for small $binv$. Thus they detected the value $binv_{crit2}$ at which the incoherent state lost stability. Note that these two values were not necessarily the same!

This observation makes the need for both upward and downward sweeps clear. A system with hysteresis would show $binv_{crit1} \neq binv_{crit2}$.[5]

Numerical Detection of Steady State

In order to automate the detection of steady-state during the sweeping of parameters, I had to design a routine that was fast enough to be called frequently, but still would have an acceptably low enough rate of false-positives. The routine was to be called after each time interval *printinterval* during numerical integration. It could return one of three values: "FAIL," "STATE_INC" (for the incoherent state), or "STATE_SYNC" (for the partially locked state).

To accomplish this, I wrote a routine that maintained running averages of the values of R and a at each function call. If the change in either running average during two successive calls or was above a specified detection sensitivity, it would automatically return the "FAIL" condition, and numerical integration would continue. That is, either $\Delta R_{avg} > s$ or $\Delta a_{avg} > s$ (where S is some specified sensitivity) would trigger "FAIL," indicating failure to achieve steady-state.

Once both the R and a running averages settled down to relatively constant values, the values ΔR_{avg} and Δa_{avg} would both drop below the detection sensitivity. At that point, a steady state had been reached, and it only remained to decide if it was the incoherent or the partially synchronized state.[6]

The test for a partially synchronized state was if the running average for

---

[5]A further complication was also possible. The system could be initialized to the state expected to be unstable, so that the globally (rather than locally) attracting characteristics of the opposite state were investigated.

[6]I avoided the problem of spurious detection for a small number of points by initializing R_{avg} to $R_{avg0} = 1.1$, a value outside its allowed range. Only after enough points had accumulated in the running average could the mean be pulled down below 1 and R reach a steady state.

R was greater than the expected level due to random fluctuations, i.e. $R_{avg} > 1/\sqrt{N_{osc}}$. For numerical stability an extra factor of 1.5 was included, so that $R_{avg} > 1.5/\sqrt{N_{osc}}$ triggered "STATE_SYNC," otherwise "STATE_INC" was signaled.

With this detection accomplished, the running average variables were reset, and the sweeping routines would shift to a new set of parameters.

6.2.2 Noise and other Variations

The specification of the equation for $\dot{\theta}$ was implemented generically as

$$\dot{\theta}_j = \omega_j + aH(\psi - \theta_j + \alpha) \ , \tag{6.10}$$

where $H(x) = \sin(x)$ was usually used. However, we could add phase noise by change the function $H(x)$ to be $H(x) = \sin(x) + \xi$, where ξ was a random variable with specified characteristics. At one point, we also investigated the affect of higher order harmonics by setting $H(x) = \sin(x) + \sin^2(x)/3$.

CHAPTER 7

THE CHIMERA STATE

7.1 Introduction [*]

7.1.1 The chimera state

A fascinating spatiotemporal pattern was reported recently by Kuramoto, Battogtokh and Shima [Kuramoto & Battogtokh, 2002; Kuramoto, 2003; Shima & Kuramoto, 2004]. While studying arrays of identical limit-cycle oscillators that are coupled nonlocally, they found that for certain choices of parameters and initial conditions, the array would split into two domains: one composed of coherent, phase-locked oscillators, coexisting with another composed of incoherent, drifting oscillators. The coexistence of locking and drift was robust. It occurred in both one and two spatial dimensions, and for various kinds of oscillators, including the Fitzhugh-Nagumo model, complex Ginzburg-Landau equations, phase oscillators, and an idealized model of biochemical oscillators.

It's important to appreciate how unexpected this coexistence state was. Nothing like it had ever been seen before, at least not in an array of identical oscillators. Normally, identical oscillators settle into one of a few basic patterns [Winfree, 1980; Kuramoto, 1984; Cross & Hohenberg, 1993]. The simplest is synchrony, with all oscillators moving in unison, executing identical motions at all times. Another common pattern is wave propagation, typically in the form of solitary waves in one dimension, spiral waves in two dimensions, and scroll waves in three dimensions. The common feature in these cases is that all the oscillators are locked in

---

frequency, with a fixed phase difference between them. At the opposite end of the spectrum is incoherence, where the phases of all the oscillators drift quasi-periodically with respect to each other, and the system shows no spatial structure whatsoever. And finally, one sometimes sees more complex patterns, including modulated structures, spatiotemporal chaos, intermittency and so on.

What was so odd about the coexistence state is that two of these patterns (locking and incoherence) were present in the same system, simultaneously. This combination of states couldn't be ascribed to the simplest mechanism of pattern formation—a supercritical instability of the spatially uniform oscillation—because it can occur even if the uniform state is linearly stable, as indeed it was for the parameter values used by Kuramoto and his colleagues. Furthermore, it has nothing to do with the classic partially locked/partially incoherent states that occur in populations of non-identical oscillators with distributed natural frequencies [Winfree, 1967; Kuramoto, 1984]. There, the splitting of the population stems from the inhomogeneity of the oscillators themselves; the desynchronized oscillators are the intrinsically fastest and slowest ones in the tails of the distribution. In contrast, for the system studied by Kuramoto et al., there is no distribution of frequencies. All the oscillators are the same, and yet they still break apart into two groups of utterly different character.

Because the coexistence state involves two seemingly incompatible forms of dynamical behavior, we will henceforth refer to it as "the chimera state," inspired by the mythological creature composed of a lion's head, a goat's body, and a serpent's tail. Today the word chimera is used more generally to indicate something made up of incongruous parts, or something that seems wildly improbable or fantastical.

Figure 7.1 shows a realization of the chimera state in the simplest setting, a one-
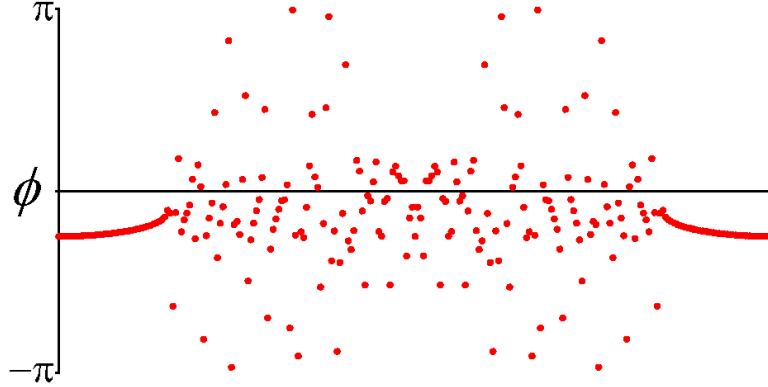
Figure 7.1: Phase pattern for a typical chimera state. Here $\kappa = 4.0$, $\alpha = 1.45$, $N = 256$ oscillators. Equation (7.1) was integrated with fixed time step $dt = 0.025$ for 8,000 iterations, starting from $\phi(x) = 6\exp\left[-30(x - \frac{1}{2})^2\right] r(x)$, where r is a uniform random variable on $\left[-\frac{1}{2}, \frac{1}{2}\right]$.

dimensional ring of phase oscillators [Kuramoto & Battogtokh, 2002; Kuramoto, 2003]. The governing equation is

$$\frac{\partial \phi}{\partial t} = \omega - \int_0^1 G\left(x - x'\right) \sin\left[\phi(x, t) - \phi(x', t) + \alpha\right] dx' \tag{7.1}$$

where $\phi(x, t)$ is the phase of the oscillator at position x at time t. The space variable x runs from 0 to 1 with periodic boundary conditions, and should be regarded as an angle on a circle (mod 1). The frequency ω plays no role in the dynamics, in the sense that one can set $\omega = 0$ without loss of generality by redefining $\phi \to \phi + \omega t$, without otherwise changing the form of equation (7.1). The kernel $G(x - x')$ provides nonlocal coupling between the oscillators. It is assumed to be even, non-negative, decreasing with the separation $|x - x'|$ along the ring, and normalized to have unit integral. Specifically, Kuramoto and Battogtokh [2002; Kuramoto, 2003] used an exponential kernel $G(x - x') \propto \exp\left(-\kappa|x - x'|\right)$. Then, for parameter values $\alpha = 1.457$ and $\kappa = 4$ and suitable initial conditions (to be discussed in detail in Section 7.3), the system evolves to the chimera state shown in Fig. 7.1.

In this snapshot of the instantaneous phases, two distinct regions are conspic-
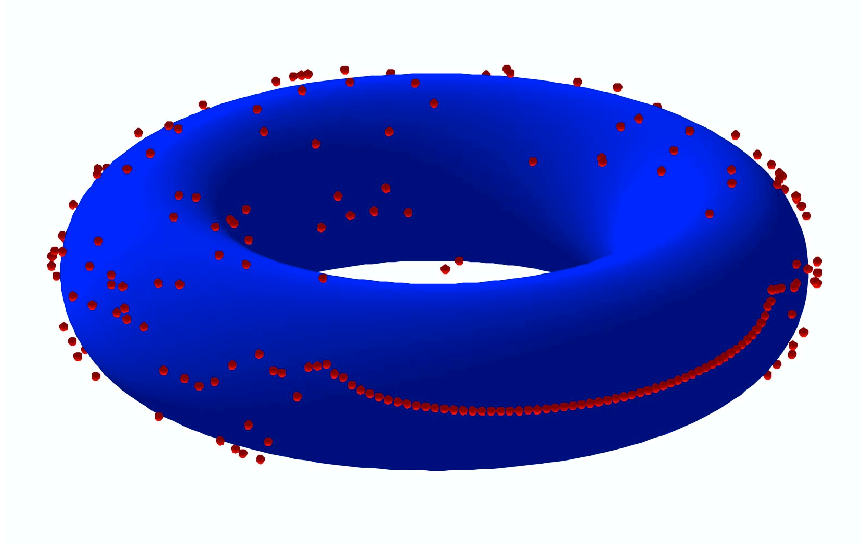
Figure 7.2: Phase pattern for a typical chimera state shown on the torus. Azimuthal angle indicates spatial position x. Phase ϕ is constant along lines of latitude; the outer equator of the torus corresponds to $\phi = 0$.

uous. The oscillators near $x = 0$ (and equivalently, $x = 1$) are phase-locked. All of them move with the same constant frequency; in a frame rotating at this frequency, they would all look frozen. The smoothness and flatness of the graph of $\phi(x)$ in this region indicates that these oscillators are coherent as well, i.e., they are nearly in phase.

Meanwhile, the scattered oscillators in the middle of Fig. 7.1 are drifting, both with respect to each other and with respect to the locked oscillators. Their motion is strongly nonuniform. They slow down when they pass near the locked pack—which is why the dots appear more densely clumped at this phase—and then speed up as they lap it.

7.1.2 Puzzles

When we first learned about the chimera state by reading [Kuramoto, 2003], we were amazed by it. How could such a thing even be possible?

In fact, a little thought showed that it was provably *impossible* in two special cases that had been studied previously:

- Global coupling: Chimera states can't occur for Eq. (7.1) with $G(x) \equiv 1$ and any choice of $0 \leq \alpha < \pi/2$, because a Lyapunov function exists for this case, demonstrating that almost all solutions are attracted to the in-phase oscillation [Watanabe & Strogatz, 1993; Watanabe & Strogatz, 1994].

- Sine coupling: If $\alpha = 0$, corresponding to a pure sine coupling in Eq. (7.1), chimera states are impossible for any even kernel G of any range. This follows because Eq. (7.1) becomes a gradient system in the frame rotating at frequency ω. Hence all attractors must be fixed points, corresponding to phase-locked solutions in the original frame, thus ruling out the possibility of coexisting drift.

So the coexistence phenomenon must somehow rely on a conspiracy between $\alpha \neq 0$ and the non-global nature of the coupling. But how, exactly?

And for that matter, is the chimera state born as soon as $\alpha \neq 0$, or at some value of α bounded away from zero? In dynamical simulations like that shown in Fig. 7.1, stable chimera states are observed only when α is close to, but slightly less than, $\pi/2$. Does that mean that these states don't exist for smaller α, or is just that their basins of attraction shrink as α decreases?

Furthermore, what is the genealogy of the chimera state, in the sense of bifurcation theory? Is it born out of the vacuum, as a pair of stable and unstable versions of itself? Or does it emerge when some more familiar attractor loses stability? For instance, does it bifurcate off the fully incoherent state, in which oscillators are uniformly scattered and drifting around the circle at every x? That seems unlikely,

since the phase pattern shown in Fig. 7.3 looks pretty far from total incoherence; even its drifting oscillators show some clumping in phase. So maybe the chimera state branches off the uniform in-phase state? But how can it, given that the in-phase state is linearly stable for all $|\alpha| < \frac{\pi}{2}$?

Motivated by these puzzles, we have tried to understand where the chimera state comes from and to pinpoint the conditions that allow it to exist. A brief report of our findings appeared in [Abrams & Strogatz, 2004].

7.1.3 Broader significance

Aside from the questions it raises, we believe the chimera state is also more broadly significant for nonlinear science, for two reasons.

First, it exemplifies the surprises that lurk in nonlocally coupled systems. As Kuramoto and his colleagues have pointed out [Kuramoto, 1995; Kuramoto & Nakao, 1996; Battogtokh & Kuramoto, 2000; Kuramoto & Battogtokh, 2002; Kuramoto, 2003; Tanaka & Kuramoto, 2003; Shima & Kuramoto, 2004], nonlocal coupling is a relatively dark corner of nonlinear science in general, and nonlinear oscillator theory in particular. Most previous work on coupled oscillators has focused on local coupling, where the interactions are assumed to be solely between nearest neighbors, or global coupling, where each oscillator interacts equally strongly with all the others. The intermediate case of nonlocal coupling is natural to explore next, and has already revealed some interesting new forms of dynamical behavior [Kuramoto, 1995; Kuramoto & Nakao, 1996].

From a more applied perspective, nonlocal coupling is important to investigate because it arises in diverse systems throughout physics, chemistry, and biology. Examples include Josephson junction arrays [Phillips *et al.*, 1993], chemical os-

cillators [Kuramoto, 1984], epidemiological models of disease spread [Medlock & Kot, 2003], the neural networks underlying the patterns on mollusc shells [Ermentrout *et al.*, 1986; Murray, 1989], localized neural "bump" states [Ben Yishai *et al.*, 1997; Gutkin *et al.*, 2001; Laing & Chow, 2001], and ocular dominance stripes in the visual cortex [Swindale, 1980; Murray, 1989].

Second, the chimera state is by no means an oddity restricted to Eq. (7.1). On the contrary, it was first seen in simulations of the complex Ginzburg-Landau equation with nonlocal coupling [Kuramoto & Battogtokh, 2002; Kuramoto, 2003], a fundamental model in the study of pattern formation. That equation in turn can be systematically derived from a wide class of reaction-diffusion equations, under particular assumptions on the local kinetics and diffusion strength that render the effective coupling nonlocal [Kuramoto & Battogtokh, 2002; Kuramoto, 2003; Tanaka & Kuramoto, 2003; Shima & Kuramoto, 2004]. Under an additional assumption that the coupling is also sufficiently weak (in a precise sense), Shima and Kuramoto [2004] show that the original reaction-diffusion system can be further reduced to a phase equation of the universal form

$$\frac{\partial \phi}{\partial t} = \omega - \int d\boldsymbol{r}' G\left(\boldsymbol{r} - \boldsymbol{r}'\right) \sin\left[\phi(\boldsymbol{r}) - \phi(\boldsymbol{r}') + \alpha\right]$$

where $\boldsymbol{r}$ labels the position of the oscillators and the kernel G decays exponentially with distance: $G(\boldsymbol{r} - \boldsymbol{r}') \propto \exp\left(-\kappa|\boldsymbol{r} - \boldsymbol{r}'|\right)$. But this is just Eq. (7.1), if the space is one-dimensional. So there is good reason to expect that the coexistence phenomenon will have some generality.

For example, in two dimensions, the coexistence of locked and drifting oscillators manifests itself as an unprecedented kind of spiral wave: one without a phase singularity at its center [Kuramoto, 2003; Shima & Kuramoto, 2004]. Instead, the oscillators in the core are found to be completely desynchronized from each

other and from the uniform rotation of the spiral arms. In effect, the core oscillators mimic a phase singularity by being incoherent. A better understanding of the one-dimensional case might shed light on this remarkable new form of pattern formation.

7.2   Summary of prior results

We begin by reviewing the results of Kuramoto and Battogtokh [2002] and Kuramoto [2003]. After uncovering the chimera state in their simulations of Eq. (7.1), they were able to explain much of its structure analytically. Their elegant approach is a generalization of Kuramoto's self-consistency argument for globally coupled oscillators [Kuramoto, 1984; Strogatz, 2000].

In this approach, one first transforms (7.1) by seeking a rotating reference frame in which the dynamics become as simple as possible. Let Ω denote the angular frequency of this rotating frame (to be determined later, in the course of solving the problem), and let

$$\theta = \phi - \Omega t$$

denote the phase of an oscillator relative to this frame. Next, introduce a complex order parameter $Re^{i\Theta}$ that depends on space and time:

$$R(x,t)e^{i\Theta(x,t)} = \int_0^1 G\left(x - x'\right) e^{i\theta(x',t)} dx' \ . \tag{7.2}$$

To see what this order parameter means intuitively, note that the integral on the right hand side of (7.2) performs a running average of $e^{i\theta}$ over a window centered at x, with a width determined by the width of the kernel G. Thus $0 \leq R(x,r) \leq 1$ can be viewed as a measure of the local phase coherence at x, and $\Theta(x,t)$ represents

the local average phase. These two average quantities provide macroscopic proxies for the overall state of the continuum of oscillators.

The real virtue of introducing the order parameter, however, is that we can now rewrite the governing equation (7.1) as

$$\frac{\partial \theta}{\partial t} = \omega - \Omega - R\sin\left[\theta - \Theta + \alpha\right] \ , \tag{7.3}$$

which makes it look as if the oscillators have decoupled, though of course they are still interacting through R and Θ, to which they each contribute through (7.2). This observation suggests that the problem can be attacked by the self-consistency arguments of mean-field theory, even though it is not globally coupled.

Now comes the key step. Suppose we restrict attention to *stationary* solutions, in which R and Θ depend on space but not on time. Now the equations truly do decouple, in the following sense. One can easily solve for the motion of the oscillator at each x, subject to the assumed time-independent values of $R(x)$ and $\Theta(x)$. The oscillators with $R(x) \geq |\omega - \Omega|$ asymptotically approach a stable fixed point θ^*, defined implicitly by

$$\omega - \Omega = R(x)\sin\left[\theta^* - \Theta(x) + \alpha\right] \tag{7.4}$$

The fact that they approach a fixed point in the rotating frame implies that they are phase-locked at frequency Ω in the original frame. On the other hand, the oscillators with $R(x) < |\omega - \Omega|$ drift around the phase circle monotonically. To be consistent with the assumed stationarity of the solution, these oscillators must distribute themselves according to an invariant probability density $\rho(\theta)$. (To ease the notation here and elsewhere, we have suppressed the dependence on x whenever it's clear from context.) And for the density to be invariant, the probability of finding an oscillator near a given value of θ must be inversely proportional to the

velocity there. From (7.3), this condition becomes

$$\rho(\theta) = \frac{\sqrt{(\omega - \Omega)^2 - R^2}}{2\pi|\omega - \Omega - R\sin(\theta - \Theta + \alpha)|} \tag{7.5}$$

where the normalization constant has been chosen such that $\int_{-\pi}^{\pi} \rho(\theta)d\theta = 1$.

The resulting motions of both the locked and drifting oscillators must be consistent with the assumed time-independent values for $R(x)$ and $\Theta(x)$. To calculate the contribution that the locked oscillators make to the order parameter (7.2), observe that

$$\begin{aligned} \sin(\theta^* - \Theta + \alpha) &= \frac{\omega - \Omega}{R} \\ \cos(\theta^* - \Theta + \alpha) &= \pm\frac{\sqrt{R^2 - (\omega - \Omega)^2}}{R} \end{aligned} \tag{7.6}$$

for any fixed point of (7.3). One can check that the *stable* fixed point of (7.3) corresponds to the plus sign in (7.6). Hence

$$\exp\left[i(\theta^* - \Theta + \alpha)\right] = \frac{\sqrt{R^2 - (\omega - \Omega)^2} + i(\omega - \Omega)}{R} \tag{7.7}$$

which implies that the locked oscillators contribute

$$\int dx' G(x - x') \exp\left[i\theta^*(x')\right] =$$

$$e^{-i\alpha} \int dx' G(x - x') \exp\left[i\Theta(x')\right] \frac{\sqrt{R^2 - (\omega - \Omega)^2} + i(\omega - \Omega)}{R} \tag{7.8}$$

to the order parameter (7.2). Here the integral is taken over the portion of the domain where $R(x') \geq |\omega - \Omega|$.

Next, to calculate the contribution from the drifting oscillators, Kuramoto and Battogtokh [2002; Kuramoto, 2003] replace $\exp\left[i\theta(x')\right]$ in (7.2) with its statistical average $\int_{-\pi}^{\pi} \exp(i\theta)\rho(\theta)d\theta$. Using (7.5) and contour integration, they obtain

$$\int_{-\pi}^{\pi} \exp(i\theta)\rho(\theta)d\theta = \frac{i}{R}\left(\omega - \Omega - \sqrt{(\omega - \Omega)^2 - R^2}\right) .$$

Therefore the contribution of the drifting oscillators to the order parameter is

$$\int dx' G(x - x') \int\limits_{-\pi}^{\pi} \exp(i\theta)\rho(\theta)d\theta =$$

$$ie^{-i\alpha} \int dx' G(x - x') \exp\left[i\Theta(x')\right] \frac{\omega - \Omega - \sqrt{(\omega - \Omega)^2 - R^2(x')}}{R(x')}$$

where now the integral is over the complementary portion of the domain where $R(x') < |\omega - \Omega|$.

Notice something curious: the integrand on the right hand side of the drifting contribution is exactly the same as that found earlier in (7.8) for the locked contribution; only their domains differ. (This coincidence is not mentioned in [Kuramoto & Battogtokh, 2002; Kuramoto, 2003].) To see that the two expressions agree, note that

$$\sqrt{R^2 - (\omega - \Omega)^2} + i(\omega - \Omega) = i\left(\omega - \Omega - \sqrt{(\omega - \Omega)^2 - R^2}\right)$$

as long as we choose the branch corresponding to the "$+i$" square root of a negative number.

Hence the two contributions can be combined into a single integral, yielding a slightly more compact version of the self-consistency equation derived in [Kuramoto & Battogtokh, 2002]:

$$R(x) \exp\left[i\Theta(x)\right] = ie^{-i\alpha} \int\limits_{0}^{1} G(x - x') \exp\left[i\Theta(x)\right] \frac{\omega - \Omega - \sqrt{(\omega - \Omega)^2 - R^2(x')}}{R(x')} dx' .$$

To ease the notation a bit more, let

$$\beta = \frac{\pi}{2} - \alpha$$

$$\Delta = \omega - \Omega . \tag{7.9}$$

Then the self-consistency equation becomes

$$R(x)e^{i\Theta(x)} = e^{i\beta} \int\limits_0^1 G(x-x')e^{i\Theta(x')}\frac{\Delta - \sqrt{\Delta^2 - R^2(x')}}{R(x')}dx' \; . \qquad (7.10)$$

Equation (7.10) is to be solved for three unknowns—the real-valued functions $R(x)$ and $\Theta(x)$ and the real number Δ—in terms of the assumed choices of β and the kernel $G(x)$. Notice that although ω itself is arbitrary up to a constant, and hence so is Ω, their difference $\omega - \Omega$ is physically meaningful; it is determined by the condition that the long-term dynamics become stationary in the frame rotating at frequency Ω.

Initially, we couldn't see how to solve the self-consistency equation (7.10) numerically. We wrote to Kuramoto for advice, and he described an iterative scheme to determine the functions $R(x)$ and $\Theta(x)$, based on initial guesses obtained from the dynamical simulations. The idea behind the scheme is that the current estimates of $R(x)$ and $\Theta(x)$ can be entered into the right hand side of (7.10), and used to generate the new estimates appearing on the left hand side.

Still, that leaves open the question of how to determine Δ. We seem to have only two equations (given by the real and imaginary parts of Eq. (7.10)) for three unknowns. Fortunately, a third equation can be imposed to close the system. Because (7.10) is left unchanged by any rigid rotation $\Theta(x) \to \Theta(x) + \Theta_0$, we can specify the value of $\Theta(x)$ at any point x we like; this freedom is tantamount to choosing an origin in the rotating frame. A natural choice would be to demand $\Theta(0) = 0$, but as we'll see in Section 7.4, another choice turns out to be more convenient.

Kuramoto and Battogtokh [2002; Kuramoto, 2003] confirm that the self consistency approach works: their results from numerical integration of the dynamical
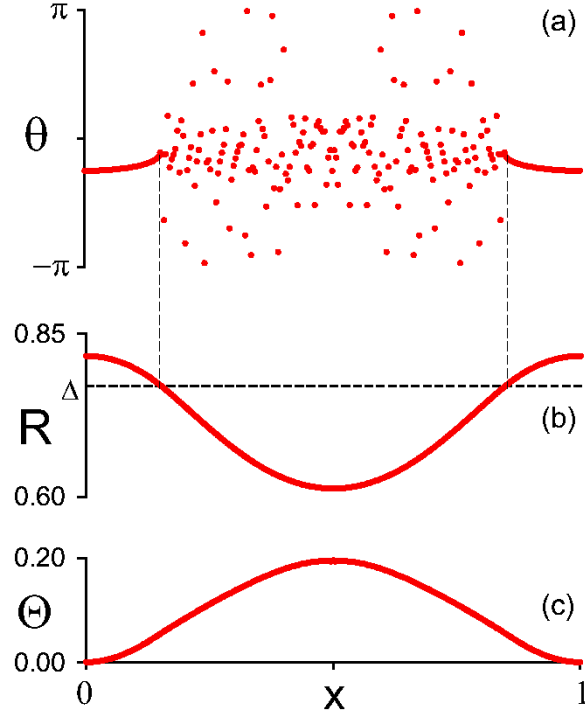
Figure 7.3: Chimera state and order parameter curves for the exponential kernel $G(x) \propto \exp\left(-\kappa|x|\right)$, as used by Kuramoto and Battogtokh [2002; Kuramoto, 2003]. Parameters are the same as those in Fig. 7.1. (a) Phase pattern for chimera state. (b) Local phase coherence $R(x)$, computed from (7.2). Locked oscillators satisfy $R(x) \geq \Delta$. (c) Local average phase $\Theta(x)$, computed from (7.2).

equations (7.1) match those obtained by solving the self-consistency equation (7.10) iteratively.

Figure 7.3 shows the chimera state along with the graphs of $R(x)$ and $\Theta(x)$ for the parameters used in Fig. 7.1. The curves in Fig. 7.3(b) and 7.3(c) are periodic and reflection-symmetric. In fact, they resemble cosine waves, which made us wonder whether (7.10) might have a simple closed-form solution, perhaps in some perturbative limit as a parameter tends to zero. To see where such a limit might come into play, we hoped to first replicate the simulations of Kuramoto and Battogtokh [2002; Kuramoto, 2003] and then to explore parameter space more widely.

7.3 A first round of simulations

Unfortunately, we couldn't find the chimera state in our early simulations of Eq. (7.1). No matter how we started the system, it always converged to the in-phase state. In the report that announced the chimera state, Kuramoto [2003] does not give precise details of the initial condition he used. He describes it as a "suitable single-humped initial phase pattern" [Kuramoto, 2003, p. 219] which we incorrectly took to mean something like $\phi(x,0) = a + b\cos x$ or $e^{-a\cos x}$.

Eventually, we asked Kuramoto for help (again!), and he kindly explained what he meant. (He also sent us his paper with Battogtokh [Kuramoto & Battogtokh, 2002], where the description of the initial condition is more explicit.) At each x, a uniform random number $\phi(x,0)$ is chosen within some interval whose width varies with x in a single-humped fashion. Specifically, the width is narrowest near $x = 0$ (mod 1), meaning that the oscillators are most nearly in phase there, initially. As x increases toward the diametrically opposite point of the domain at $x = \frac{1}{2}$, the phases are scattered progressively over larger and larger regions on the phase circle (meaning the oscillators are placed more and more incoherently there, initially). The effect of this procedure is to give the system a jump-start, by placing it in a partially coherent/partially incoherent state to begin with.

To be more precise, Kuramoto used a random distribution with a Gaussian envelope: $\phi(x,0) = 6\exp\left[-30\left(x - \frac{1}{2}\right)^2\right] r(x)$, where $r(x)$ is a uniform random number on the interval $-\frac{1}{2} \leq r \leq \frac{1}{2}$. For the parameters used in Fig. 7.3, this initial condition indeed evolves to the chimera state reported in [Kuramoto & Battogtokh, 2002; Kuramoto, 2003].

Then we ran simulations to see how far this state could be continued by decreasing α, knowing that it would have to disappear or lose stability somewhere

before $\alpha = 0$. To track its fate along the way, we also computed several statistics:

1. the spatial average of $R(x)$, given by $\langle R \rangle = \int_0^1 R(x)dx$;

2. the amplitude of $R(x)$, defined as $R_{amp} = R_{max} - R_{min}$;

3. f_{drift}, the fraction of the spatial domain occupied by drifting oscillators;

4. the difference $\Delta = \omega - \Omega$ between the nominal frequency of individual oscillators and their collective frequency when locked; and

5. $\overline{\Delta}_{\text{max}}$, the largest value of the time-averaged drift velocity relative to the rotating frame. This quantity measures the average speed of the fastest drifting oscillator. From (7.3), it can be calculated as

$$\max_{x} \left| \overline{\Delta}(x) \right| = \max_{x} \left| \sqrt{\Delta^2 - R^2(x)} \right| ,$$

where the maximum is taken only over the drifting oscillators.

Figure 7.4 shows how f_{drift} varies when κ is held constant but α is changed smoothly. We generated similar graphs for each of the statistics mentioned above, and all showed a jump to the uniform synchronized state as α decreased below some critical value α_c. From these results it appeared that when $\kappa = 4.0$, the chimera state ceased to exist somewhere around $\alpha_c \approx 1.37$. The transition seemed to be discontinuous, which suggested that α_c couldn't be calculated by a naive perturbation expansion. If it was to be calculable at all, something more subtle would be required.

The next step was to investigate how these results vary with κ. Recall that the kernel in (7.1) is $G(x) = C \exp(-\kappa |x|)$, so $1/\kappa$ sets a characteristic length scale. Roughly speaking, it is the distance over which the nonlocal coupling is substantial.
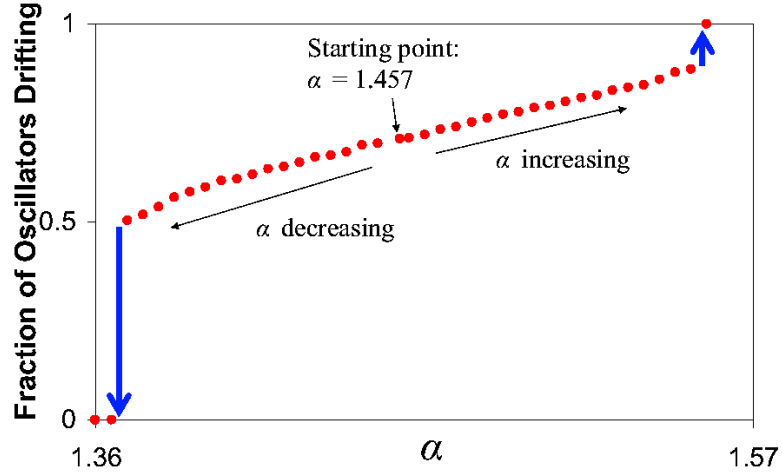
Figure 7.4: The fraction of oscillators drifting as the coupling parameter α varies. Here $\kappa = 4.0$, $N = 256$ oscillators, $dt = 0.025$ for 100,000 iterations.

So the limit $\kappa \to 0^+$ corresponds to global coupling $G(x) \equiv 1$. This can also be checked directly, noting that the normalization constant for the exponential kernel on the circle is given by $C = \frac{\kappa}{2}(1 - e^{-\kappa/2})^{-1}$.

Figure 7.5 shows a rough contour plot of R_{amp} in the (α, κ) parameter plane. Crude as this plot is, its message is still clear. The stable chimera state evidently lives in a wedge in parameter space, bounded on one side by the line $\alpha = \frac{\pi}{2}$ and on the other by a curve $\alpha = \alpha_c(\kappa)$ that is nearly a straight line. By its very shape, the picture directs our attention to the corner of the wedge, to the simultaneous limit as $\alpha \to \frac{\pi}{2}$ from below and $\kappa \to 0$ from above. Apparently something crucial happens in that corner—the chimera state is born there. And so this is where perturbation theory should be conducted.

To check that the wedge of Fig. 7.5 was not an artifact of the exponential kernel assumed above, we also calculated the corresponding contour plots for the cosine kernel

$$G(x) = \frac{1}{2\pi}(1 + A \cos x) , \tag{7.11}$$

where $0 \leq A \leq 1$. Here the spatial domain has been redefined to $-\pi \leq x \leq \pi$ for
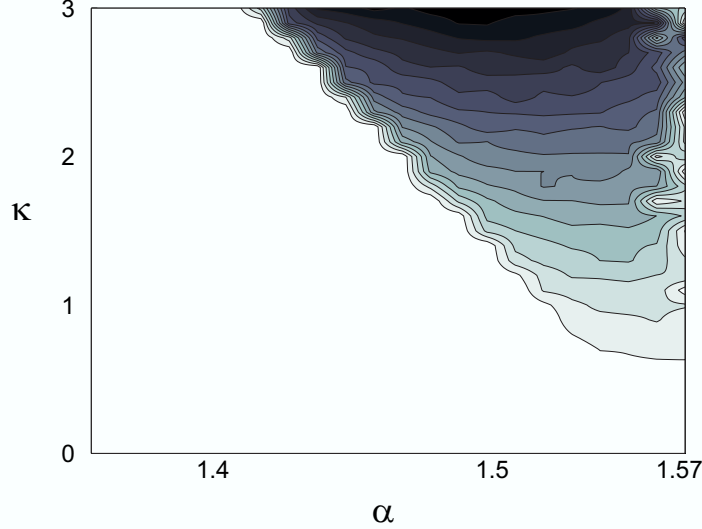
Figure 7.5: Amplitude of the curve $R(x)$, depicted as a contour plot in parameter space, and calculated by averaging over the instantaneous R curves during numerical integration. Here $G(x) \propto \exp(-\kappa|x|)$, $N = 80$ oscillators, the integration time step is $dt = 0.025$, and integration continued for 20,000 iterations. Lighter colors indicate smaller amplitude; lightest is $R_{amp} = 0.0$ and darkest is $R_{amp} = 0.13$.

convenience, and to bring out its ring geometry and the reflection symmetry of the chimera state. Figure 7.6 confirms that the cosine kernel gives a similar chimera state to that for the exponential kernel used above, while Fig. 7.7 demonstrates that the wedge in parameter space is preserved as well. All that is reassuring, because as it happens, the cosine kernel also has the pleasant property that it allows the self-consistency equation to be solved analytically.

7.4 An exactly solvable case

From now on, let $G(x)$ be given by the cosine kernel (7.11), and let the spatial domain be $-\pi \leq x \leq \pi$ with periodic boundary conditions. For this case, we'll show that the functional form of the order parameter can be obtained exactly, which in turn yields the explicit x-dependence of $R(x)$ and $\Theta(x)$. All the resulting
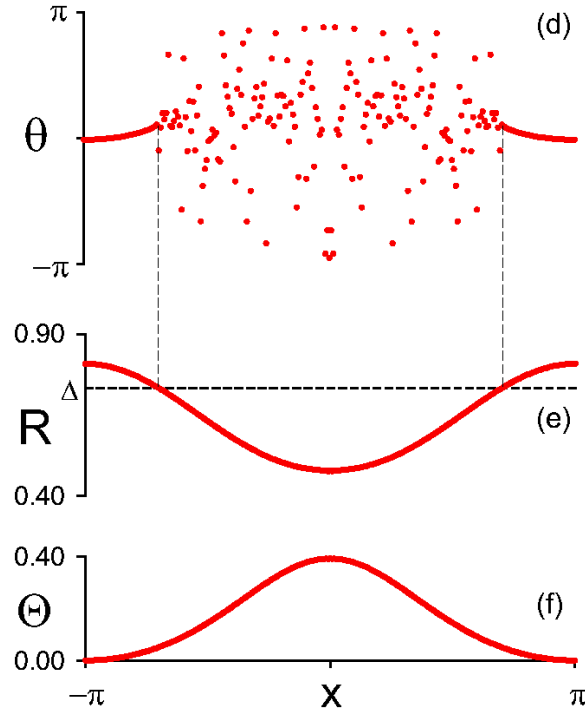
Figure 7.6: Chimera state and corresponding order parameter curves for the cosine kernel, shown in the same format as Fig. 7.3, and qualitatively similar to it. Parameters are $A = 0.995$, $\beta = 0.18$, $N = 256$ oscillators; equation (7.1) was integrated with fixed time step $dt = 0.025$ for 200,000 iterations, starting from $\phi(x) = 6r \exp(-0.76x^2)$, where r is a uniform random variable on $\left[-\frac{1}{2}, \frac{1}{2}\right]$.

expressions, however, still contain two unknown coefficients, one real and the other complex, which need to be determined self-consistently. In this way, the two unknown functions in the self-consistency equation are exchanged for two unknown numbers—a drastic reduction in the difficulty of the problem.

The self-consistency equation (7.10) is

$$R(x)e^{i\Theta(x)} = e^{i\beta} \int_{-\pi}^{\pi} G(x - x')e^{i\Theta(x')}h(x')dx' \tag{7.12}$$

where we've introduced the notation

$$h(x') = \frac{\Delta - \sqrt{\Delta^2 - R^2(x')}}{R(x')} \ . \tag{7.13}$$
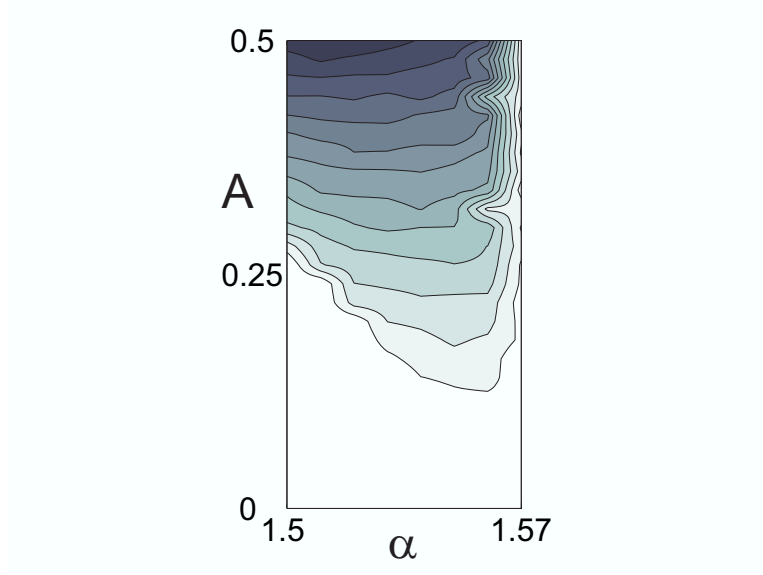
Figure 7.7: Contour plot of R_{amp} for the chimera state with cosine kernel. Note the similarity to Fig. 7.5 for the exponential kernel. Here $G(x) = \frac{1}{2\pi}(1 + A\cos x)$, $N = 80$ oscillators, the integration time step was $dt = 0.025$, and integration continued for 30,000 iterations. Same color scale as Fig. 7.5.

Let angular brackets denote a spatial average:

$$\langle f \rangle = \frac{1}{2\pi} \int_{-\pi}^{\pi} f(x')dx'.$$

Then, substituting the cosine kernel (7.11) into (7.12) and expanding $G(x - x')$ by a trigonometric identity, we find

$$
\begin{aligned}
Re^{i\Theta} &= \frac{e^{i\beta}}{2\pi} \int_{-\pi}^{\pi} [1 + A\cos x \cos x' + A\sin x \sin x']h(x')e^{i\Theta(x')}dx' \\
&= e^{i\beta}\left\langle he^{i\Theta}\right\rangle + e^{i\beta}A\left\langle he^{i\Theta}\cos x'\right\rangle \cos x + e^{i\beta}A\left\langle he^{i\Theta}\sin x'\right\rangle \sin x \\
&= c + a\cos x \quad\quad\quad (7.14)
\end{aligned}
$$

where the coefficients c and a must satisfy their own version of the self-consistency equations, now given by

$$c = e^{i\beta}\left\langle he^{i\Theta}\right\rangle \quad\quad\quad (7.15)$$

and

$$a = Ae^{i\beta} \left\langle he^{i\Theta} \cos x' \right\rangle . \tag{7.16}$$

Note that the coefficient of $\sin x$ vanishes in (7.14). This follows from the assumption that $R(x') = R(-x')$ and $\Theta(x') = \Theta(-x')$, as suggested by the simulations; then $h(x')$ in (7.13) is also even, and so the integral $\left\langle he^{i\Theta} \sin x' \right\rangle$ in (7.14) vanishes by oddness. As we'll show next, this assumption of reflection symmetry is self-consistent, in the sense that it implies formulas for $R(x)$ and $\Theta(x)$ that indeed possess this symmetry.

For example, to calculate $R(x)$ in terms of the unknown coefficients a and c, observe that

$$\begin{aligned} R^2 &= (Re^{i\Theta})(Re^{-i\Theta}) \\ &= (c + a \cos x)(c^* + a^* \cos x) \\ &= |c^2| + 2\mathrm{Re}\,(ca^*) \cos x + |a|^2 \cos^2 x \end{aligned} \tag{7.17}$$

which is an even function, and which also helps to explain why the graph of $R(x)$ in Fig. 7.3 resembled a cosine wave.

Likewise, $\Theta(x)$ is an even function reminiscent of a cosine because

$$\begin{aligned} \tan \Theta(x) &= \frac{R(x) \sin \Theta(x)}{R(x) \cos \Theta(x)} \\ &= \frac{\mathrm{Im}\,(c) + \mathrm{Im}\,(a) \cos x}{\mathrm{Re}\,(c) + \mathrm{Re}\,(a) \cos x} . \end{aligned} \tag{7.18}$$

Another simplification is that c can be taken to be purely real and non-negative, without loss of generality. This follows from the rotational symmetry of the governing equations. In particular, the self-consistency equation (7.12) is left unchanged by any rigid rotation $\Theta(x) \to \Theta(x) + \Theta_0$. Thus we are free to specify any value of

$\Theta(x)$ at whatever point we like. The most convenient choice is to set

$$\Theta\left(\frac{\pi}{2}\right) = 0 \ .$$

Then at that value of x the equation $Re^{i\Theta} = c + a\cos x$ reduces to

$$R\left(\frac{\pi}{2}\right) = c \ .$$

Since R is real and non-negative, so is c. Hence, we take

$$\mathrm{Im}\,(c) = 0 \tag{7.19}$$

from now on.

The final step in closing the equations for a and c is to rewrite the averages in (7.15) and (7.16) in terms of those variables. To do so, we express $he^{i\Theta}$ as

$$
\begin{aligned}
he^{i\Theta} &= \left(Re^{i\Theta}\right)\frac{h}{R} \\
&= (c + a\cos x)\frac{\Delta - \sqrt{\Delta^2 - R^2(x)}}{R^2(x)} \\
&= \frac{\Delta - \sqrt{\Delta^2 - R^2(x)}}{c + a^*\cos x} \tag{7.20}
\end{aligned}
$$

where we have used (7.17) and the real-valuedness of c to simplify the second line above. Inserting (7.17) and (7.20) into (7.15) and (7.16), we obtain the desired self-consistency equations for a and c:

$$c = e^{i\beta}\left\langle \frac{\Delta - (\Delta^2 - c^2 - 2\mathrm{Re}\,(a)\,c\cos x - |a|^2\cos^2 x)^{\frac{1}{2}}}{c + a^*\cos x} \right\rangle \tag{7.21}$$

$$a = Ae^{i\beta}\left\langle \frac{\Delta - (\Delta^2 - c^2 - 2\mathrm{Re}\,(a)\,c\cos x - |a|^2\cos^2 x)^{\frac{1}{2}}}{c + a^*\cos x}\cos x \right\rangle \ . \tag{7.22}$$

This pair of complex equations is equivalent to four real equations for the four real unknowns c, $\mathrm{Re}\,(a)$, $\mathrm{Im}\,(a)$, and Δ. The solutions, if they exist, are to be expressed as functions of the parameters β and A.

7.5   Clues based on numerics

Before we plunge into the details of solving equations (7.21) and (7.22) simultane-
ously, let's pause to remember what we're trying to do.

We want to understand where the chimera state lives in parameter space and
how it bifurcates. Guided by the simulations of Section 7.3, we expect that (7.21),
(7.22) should have chimera solutions throughout the wedge-shaped region of para-
meter space shown in Fig. 7.7. Assuming that's true, we hope that these solutions
will continue all the way down to the corner $(\alpha, A) = (\frac{\pi}{2}, 0)$, corresponding to
$(\beta, A) = (0, 0)$, where might be able to analyze them with perturbation theory.

Our strategy, then, is to start by finding one solution to (7.21), (7.22), by any
means possible, for parameter values anywhere in the wedge. Having found this
solution, we can use it as a base point for a numerical continuation method. Then
we proceed to dive into the corner, following a straight line through parameter
space between the base point and the corner. In this way we convert the problem
to a one-parameter study of the solutions of (7.21), (7.22). Sufficiently close to
the corner, we expect that the solutions will display some sort of scaling behavior
with respect to the parameter. That scaling will then suggest clues about the right
ansatz for a subsequent perturbation calculation.

So first we have to come up with a chimera solution to (7.21), (7.22). It's not
just a matter of plugging the equations into a standard root-finding package. The
trouble is that these equations also have *other* solutions that we're less interested
in, and we don't want the numerical root-finding scheme to converge to them
instead.

In particular, the in-phase solution, where all the oscillators are locked at the
same phase and none of them are drifting, has a large basin of attraction that

competes with that of the chimera state. To see what values of a, c, and Δ correspond to the in-phase state, note that when $\phi(x,t) = \phi(x',t)$ for all x and x', Eq. (7.1) implies $\phi(x,t) = \phi_0 + (\omega - \sin\alpha)t$. Hence $R = 1$ and therefore $c = 1$ and $a = 0$. And because $\Omega = \omega - \sin\alpha = \omega - \cos\beta$, we have $\Delta = \omega - \Omega = \cos\beta$. Thus

$$(a, c, \Delta)_{\text{in-phase}} = (0, 1, \cos\beta) \ . \tag{7.23}$$

It's easy to check that this satisfies (7.21), (7.22) for all values of A and β.

To reduce the chance that the root-finder will converge onto this in-phase state, we need to concoct an initial guess that's very close to a genuine chimera state. To find one, we numerically integrated Eq. (7.1) using the cosine kernel, and fit the resulting graphs of $R(x)$ and $\Theta(x)$ to the exact formulas (7.17) and (7.18), to estimate the values of a and c. The frequency difference Δ was obtained directly from the simulation, by setting $\omega = 0$ and then computing $\Delta = \omega - \Omega = -\Omega$, where Ω is observable as the collective frequency of the locked oscillators.

In this way we estimated $a = 0.156 - 0.072i$, $c = 0.591$, $\Delta = 0.720$ for the stable chimera state at parameter values $A = 0.99$, $\beta = 0.081$. We fed this starting guess into the Matlab root-finding and numerical continuation program MatCont [Dhooge *et al.*, 2003] and found rapid convergence to $a = 0.162 - 0.051i$, $c = 0.588$, $\Delta = 0.723$. From there, we could continue the solution in either A or β or some combination, as we saw fit.

This approach enabled us to track the chimera state throughout parameter space, until it disappeared along a critical curve corresponding to the boundary of the wedge shown earlier. The results of this calculation are shown in Fig. 7.8. As expected, the boundary of the region is nearly a straight line, and it extends down to the origin.
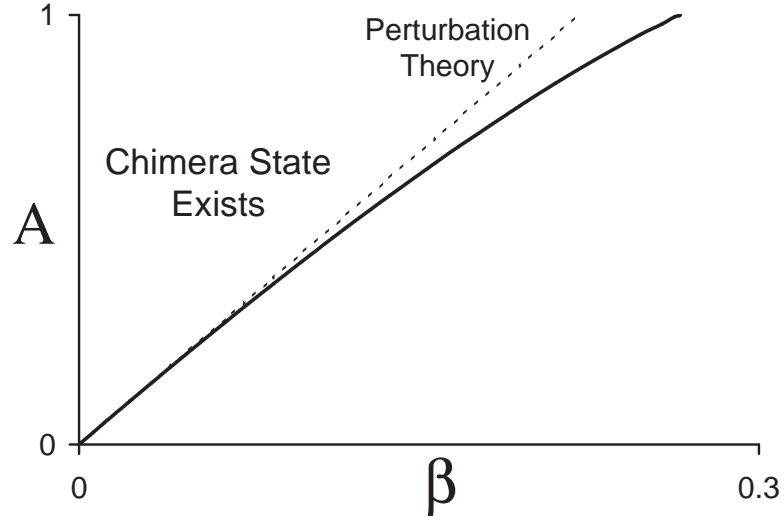
Figure 7.8: The region of parameter space in which the chimera state exists. Solid line, exact boundary determined by numerical solution of (7.21) and (7.22); dashed line, leading order approximation to this boundary obtained by perturbation theory (see text).

7.6 Perturbation theory

The next step is to look for scaling laws to guide our perturbation calculations. Figure 7.9 shows the results of numerical continuation starting from $(\beta, A) = (0.08, 0.99)$ and moving along the line $A = 12.375\beta$ towards the origin, all the while remaining within the wedge shown in Fig. 7.8. The observed behavior of the variables along that line suggests the following ansatz near the origin:

$$\Delta \sim 1 + \Delta_1 \epsilon + \Delta_2 \epsilon^2$$

$$c \sim 1 + c_1 \epsilon + c_2 \epsilon^2$$

$$\mathrm{Re}\,(a) \sim u\epsilon^2$$

$$\mathrm{Im}\,(a) \sim v\epsilon^2 \tag{7.24}$$

where we have introduced $\epsilon = A$ as the small parameter.

Next, we assume that this ansatz continues to hold along other lines through
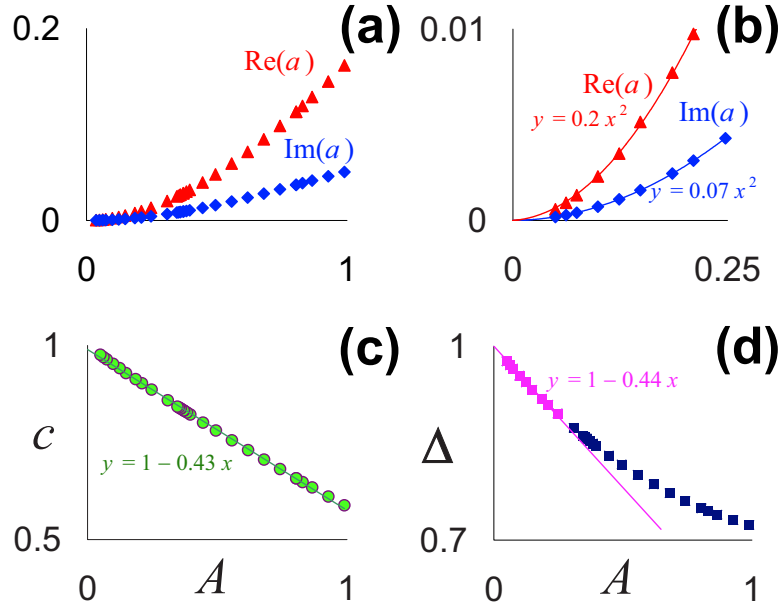
Figure 7.9: Scaling laws near the origin in parameter space, along the line $A = 12.375\beta$. Data were collected from numerical continuation of a known chimera state, for an ensemble of parameter values. Approximate fits were then determined by least-square regression. (a) Scaling of real and imaginary parts of a; (b) Zoom of panel (a) near origin in parameter space. Note that curves are quadratic; (c) Linear scaling of real-valued variable c; (d) Scaling of Δ. Note that Δ scales linearly for small values of A (purple).

the origin. Such lines can be parametrized as

$$A = \epsilon,$$

$$\beta = \beta_1 \epsilon \,,$$

where A and β tend to zero simultaneously as $\epsilon \to 0$. Here β_1 is a free parameter inversely related to the slope of the lines. Thus the asymptotic shape of the wedge in Fig. 7.8, sufficiently close to the origin, will be determined from the maximum and minimum values of β_1 for which a perturbative solution exists.

Substituting the ansatz (7.24) into the self-consistency equation (7.21) for c,

and retaining only terms up to $\mathcal{O}\left(\sqrt{\epsilon}\right)$ gives

$$
\begin{aligned}
1 + \mathcal{O}\left(\epsilon\right) &= (1 + i\beta_1\epsilon) \left\langle \frac{1 + \Delta_1\epsilon - (1 + 2\Delta_1\epsilon - 1 - 2c_1\epsilon)^{\frac{1}{2}}}{1 + c_1\epsilon} \right\rangle \\
&= 1 - \sqrt{2}\sqrt{\Delta_1 - c_1}\sqrt{\epsilon} + \mathcal{O}\left(\epsilon\right) ,
\end{aligned}
$$

implying that

$$
\Delta_1 = c_1 . \tag{7.25}
$$

Now we retain terms up to $\mathcal{O}\left(\epsilon\right)$ on both sides, and apply Eq. (7.25) whenever necessary to cancel terms. At this order, Eq. (7.21) becomes

$$
1 + c_1\epsilon = 1 + i\beta_1\epsilon - \epsilon\sqrt{2}\left\langle \sqrt{(\Delta_2 - c_2) - u\cos x} \right\rangle . \tag{7.26}
$$

To simplify notation, let

$$
\delta = \Delta_2 - c_2 . \tag{7.27}
$$

After breaking up the previous expression (7.26) into two equations for the real and imaginary parts, and equating terms of $\mathcal{O}\left(\epsilon\right)$, we get

$$
c_1 = -\mathrm{Re}\left[\sqrt{2}\left\langle \sqrt{\delta - u\cos x} \right\rangle\right] \tag{7.28}
$$

$$
\beta_1 = \mathrm{Im}\left[\sqrt{2}\left\langle \sqrt{\delta - u\cos x} \right\rangle\right] . \tag{7.29}
$$

Repeating the same expansion to $\mathcal{O}\left(\epsilon\right)$ in the self-consistency equation (7.22) for a yields two analogous equations:

$$
u = -\mathrm{Re}\left[\sqrt{2}\left\langle \cos x\sqrt{\delta - u\cos x} \right\rangle\right] \tag{7.30}
$$

$$
v = -\mathrm{Im}\left[\sqrt{2}\left\langle \cos x\sqrt{\delta - u\cos x} \right\rangle\right] . \tag{7.31}
$$

The equations (7.28)–(7.31) form a closed system for the variables (c_1, u, v, δ), given the parameter β_1. But to solve these equations, it proves more convenient to regard β_1 as a variable, and δ as a parameter; we adopt this point of view in what follows.
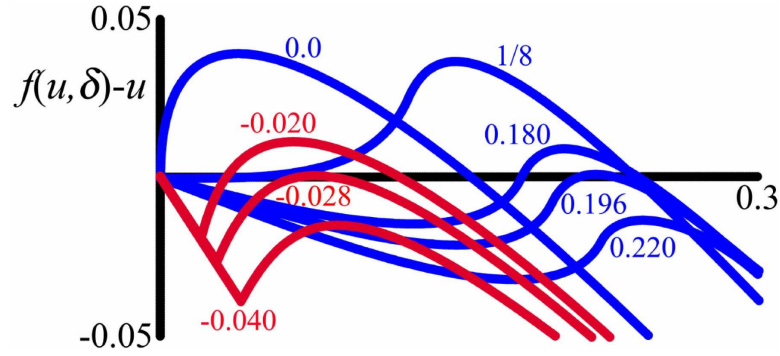
Figure 7.10: Roots of Eq. (7.30) for various values of δ. Red indicates negative δ and blue positive δ. For $\delta < -0.028$ there are no roots; for $-0.028 < \delta < 0$, two roots; for $0 < \delta < \frac{1}{8}$, one root; for $\frac{1}{8} < \delta < 0.196$, two roots; and for $\delta > 0.196$, no roots .

There's another important structural aspect of equations (7.28)–(7.31), namely, that (7.30) is distinguished in that it involves only two unknown quantities. It has the form $u = f(u, \delta)$ and can be solved numerically for a given δ. When a solution exists, all other variables (c_1, β_1, v) can be generated parametrically from the (u, δ) pair. Thus, the problem of solving equations (7.28)–(7.31) reduces to a root-finding exercise in one dimension instead of four.

Figure 7.10 plots the graph of the difference $f(u, \delta) - u$ for several values of δ. The zeros of this graph correspond to the solutions of (7.30), and yield the desired $(u(\delta), \delta)$ pairs. These are then substituted into the remaining equations to obtain $c_1(\delta)$, $\beta_1(\delta)$, and $v(\delta)$, from which various quantities of physical interest can be derived.

7.6.1 Calculation of f_{drift}

For example, we can use the perturbative solution to find f_{drift}, the fraction of the system that is drifting. It is most convenient to calculate this quantity first in terms of δ, and then later re-express it in terms of the more natural control

parameter β_1.

To find the drifting oscillators, recall from Fig. 7.6 that the cutoff between the locked portion and the drifting portion occurs at the crossover value $x = x_c$ where $R(x_c) = |\Delta|$. Substituting (7.17) for R^2 and equating this to Δ^2, we obtain

$$|c|^2 + 2\mathrm{Re}\,(ca^*)\cos x_c + |a|^2 \cos^2 x_c = \Delta^2 \ . \tag{7.32}$$

Plugging in the ansatz (7.24) and keeping terms up to order ϵ^2, we find

$$1 + 2c_1\epsilon + (c_1^2 + 2c_2)\epsilon^2 + 2u\epsilon^2 \cos x_c = 1 + 2\Delta_1\epsilon + (\Delta_1^2 + 2\Delta_2)\epsilon^2 \ . \tag{7.33}$$

Finally, because of (7.25), this simplifies to

$$\cos x_c = \frac{\Delta_2 - c_2}{u} = \frac{\delta}{u} \ . \tag{7.34}$$

Since the spatial domain of the ring has length 2π and $2x_c$ is the length of the region occupied by drifting oscillators, the fraction of the chimera state corresponding to drifting oscillators is $f_{\mathrm{drift}} = x_c/\pi$, and hence

$$f_{\mathrm{drift}} = \frac{1}{\pi} \left| \cos^{-1}\left(\frac{\delta}{u(\delta)}\right) \right| \ . \tag{7.35}$$

Figure 7.11 plots the numerically computed $f_{\mathrm{drift}}(\delta)$ against $\beta_1(\delta)$. The curve has a turning point at $\beta_1 \approx 0.22$, when about 44% of the system is drifting. Presumably, this turning point stems from a saddle-node bifurcation in the underlying dynamics. In our simulations, we only see the upper branch of this curve, suggesting that this corresponds to the *stable* version of the chimera state. The reciprocal of the critical β_1 is about 4.5, which is the slope of the dashed line shown in Fig. 7.8, in excellent agreement with the boundary of the wedge found numerically.
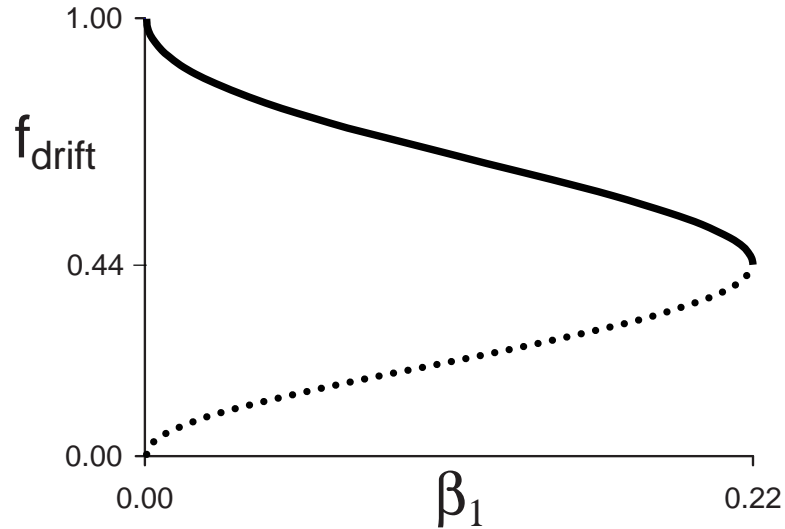
Figure 7.11: Fraction of chimera state consisting of drifting oscillators as a function of β_1. Solid line indicates stable chimera, dotted line indicates unstable. The maximum β_1 determines the line bounding the wedge-shaped existence region in Fig. 7.8.

7.6.2 Birth and Death of the Chimera State

Although the parametric dependence of f_{drift} seems to be conveniently expressed with respect to β_1, that representation conceals a lot. Several dynamically distinct states of the system are invisible because they are all squeezed onto a single point $(\beta_1, f_{\mathrm{drift}}) = (0, 1)$, as we'll see below. It's much more revealing to use δ instead of β_1.

Therefore, we now examine the system in the set of coordinates shown in Fig. 7.12, with u plotted vertically and δ horizontally. This picture is a compendium of *all* the stationary states of the system—the stable and unstable chimera, along with other states that we haven't mentioned yet, which we call uniform drift, modulated drift, and homoclinic locked states. The virtue of this representation is that it allows us to see each bifurcation that occurs as the chimera state comes into existence and later disappears. Beginning at the origin and moving counterclockwise around the kidney-bean shaped cycle, we have:
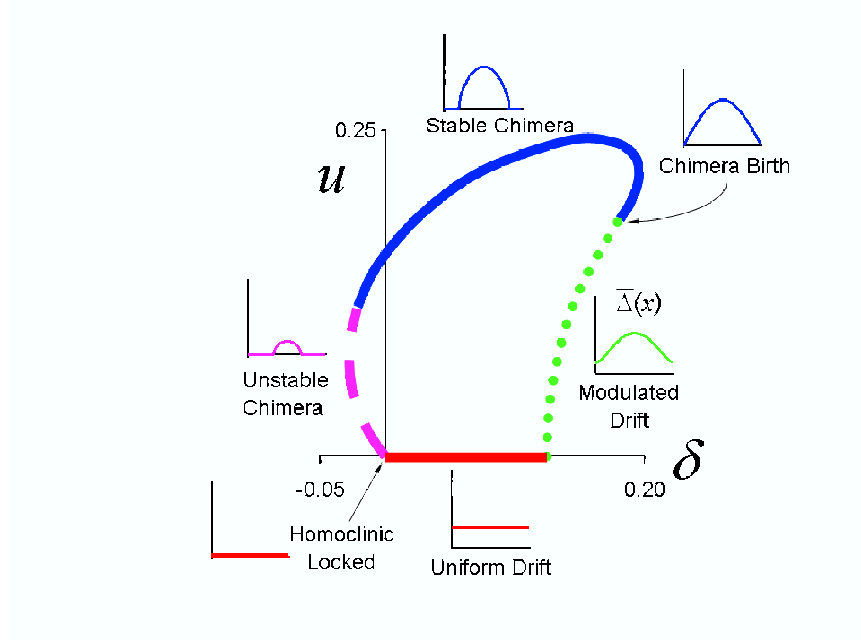
Figure 7.12: Diagram of bifurcations giving rise to the chimera state in $u-\delta$ plane. Insets show average frequency $\overline{\Delta}$ versus x. Please see text for definitions of the perturbative variables δ and u, and for a detailed explanation of this figure.

1. *Homoclinic locked state:* $u = \delta = 0$. Here, all the oscillators are locked in phase, and hence frozen in the rotating frame. Accordingly, the average frequency $\overline{\Delta}(x)$ of the oscillators vanishes for all x, as shown in the inset. But one can show that this state is not linearly stable. In fact, the exact, non-perturbative counterpart of this state is the in-phase locked state (7.23) at the critical parameter value $\beta = 0$, where this state undergoes a homoclinic saddle-node bifurcation.

2. *Spatially uniform drift:* For $u = 0$ and small $\delta > 0$, the system has a stationary state in which all the oscillators drift in a way that varies strongly in time but remains uniform in x. The order parameter $R(x)$ is independent of x and close to 1, meaning that the oscillators are nearly in phase for nearly all of the time. An individual oscillator executes a jerky motion around its

phase circle, lingering near $\theta = 0$ and then whipping around the rest of the phase circle back to this point. The associated plot of $\overline{\Delta}(x)$ is flat because of the uniformity in x.

In terms of the perturbative variables used in Fig. 7.12, this state appears on the line $u = 0$ with $\delta > 0$. Then (7.31) shows that $v = 0$ as well; hence $a = 0$, to $\mathcal{O}(\epsilon^2)$. So (7.17) implies that $R(x)$ must be real and constant and (7.18) implies that $\Theta(x) = 0$. Equation (7.29) tells us that such a state is possible only if $\beta_1 = 0$, which suggests that one can find an exact, non-perturbative version of the uniform drift state when $\beta = 0$. Indeed, seeking a solution of the self-consistency equation (7.12) with $\beta = 0, \Theta(x) = 0$, and constant $R(x)$, one finds $R^2 = \Delta - \sqrt{\Delta^2 - R^2}$ since the kernel G is normalized. Hence, along this line $\beta = 0$, $\Theta(x) = 0$, and $R(x) = R = \sqrt{2\Delta - 1}$.

3. *Onset of spatial structure:* At the lower right corner of the kidney bean, the function $f(u, \delta) - u$ (Fig. 7.10) becomes tangent at the origin, introducing a new branch of solutions with $\Theta = 0$ and $\beta = 0$ but with the coherence R varying spatially. This is the birth of spatial structure in the system. It happens for $\delta = \frac{1}{8}$. The non-perturbative generalization of this result is $\Delta = 2/(2 + A)$. (See Appendix 7.8.)

4. *Modulated drift:* Along the first curved branch, all oscillators continue to drift, but now there is spatial structure in the $R(x)$ curve, leading to a modulated pattern of average velocities (see inset). However, the average angle $\Theta(x)$ is still identically 0.

5. *Chimera birth:* At the point where $u = \delta$, the first locked oscillators are born. For the first time, v and β_1 become nonzero (see Eq. (7.29),(7.31)).

Until this point, all of the states have been confined to the vertical axis of Fig. 7.8; now we finally we move off the wall. The curve of average velocities $\overline{\Delta}(x)$ touches the x-axis at a single point. Meanwhile, the system develops spatial structure in its average phase: $\Theta(x)$ is no longer identically zero.

This bifurcation can be shown to occur at $\delta = 16/(9\pi^2)$, by evaluating the integral in (7.30) with $u = \delta$; also, see Appendix 7.9 for an exact calculation of the chimera state at birth.

6. *Stable chimera:* Along the top of the kidney bean, the chimera state is dynamically stable. After its birth from the spatially modulated drift state, it gradually develops an increasing fraction of locked oscillators as we move in the counterclockwise direction. Locked oscillators correspond to the zero part of the $\overline{\Delta}(x)$ curve (they appear motionless because the reference frame was chosen to co-rotate with them).

7. *Saddle-node bifurcation:* As we continue to move counterclockwise, the value of β_1 grows (along with the fraction of locked oscillators), and reaches its maximum at the point where the stable chimera ceases to exist. The disappearance is a result of a saddle-node bifurcation—a collision with an unstable chimera state—and occurs when about 44% of the system is drifting.

8. *Unstable chimera:* Along the unstable dashed branch, the fraction of locked oscillators continues to grow. But the value of β_1 now begins to decrease, indicating a movement back towards the wall in Fig. 7.8. The system returns to its original state when all oscillators become locked, with $\delta = u = \beta_1 = 0$ and $R=1$.

Taking a step back, we can see an interesting message of Fig. 7.12. The stable

and unstable chimera states are continuously connected though the branches of drifting states, shown in solid red and dotted green lines. If we had used the β_1 representation instead (as in Fig. 7.11), both of these connecting branches would have shrivelled down to a point. The two kinds of chimera states would seem disconnected in a way that they really aren't.

7.7 Discussion

Our main result in this paper is an exact solution for the chimera state, for the special case of a cosine kernel. That solution also shed light on the bifurcations which create and destroy the chimera.

In retrospect, it's not surprising that a cosine kernel would make the self-consistency equation (7.10) as tractable as possible, because the right hand side of (7.10) is a convolution integral, and trigonometric functions behave nicely under convolution. For this reason, it should be straightforward to extend the calculations to include more harmonics in G. Using the same argument as in Section 7.4, one can see that the exact solution for the order parameter (7.14) will have the same number of harmonics as G has. This approach would then give a systematic way to solve the self-consistency equation for any kernel representable as a finite Fourier cosine series. By taking more and more terms, this approach also gives a way to approximate results for any even kernel, as long as it is representable by a Fourier series.

Unfortunately, the trick of choosing a special kernel may not work as well in two (or three) spatial dimensions. That could limit the applicability to two-dimensional chimeras, such as the novel spiral waves computed numerically in [Kuramoto, 2003]. Nevertheless, the idea of seeking a tractable kernel that can

simplify the problem may itself be useful.

Another caveat is that, despite its usefulness as a mathematical tool, the perturbative approach adopted here does not give a rigorous understanding of the bifurcations in the original problem. One would like to understand the bifurcation scenarios for *all* values of the coupling parameter A, which essentially measures how far the nonlocal coupling deviates from strictly global coupling. In Appendices 7.8 and 7.9, we show two results along these lines.

One interesting aspect of the perturbative approach is that it draws our attention to the special parameter values $A = 0$, $\beta = 0$ (or equivalently $\alpha = \pi/2$). Here the system has global cosine coupling and is known to be completely integrable [Watanabe & Strogatz, 1993; Watanabe & Strogatz, 1994]. So in a sense, what we have done in this paper is perturb off this extremely degenerate system, which raises the question of whether other, unforeseen attractors might also lurk nearby, for different choices of initial conditions.

The surprising nature of the chimera state makes us wonder if it could be created artificially in a laboratory experiment, or possibly even occur naturally in some system.

As a first attempt to judge whether this might be possible, we tried to integrate the phase equation (7.1) with slightly nonuniform frequencies ω_i, to mimic the inhomogeneities that would occur in any real system, and to test whether the chimera is an artifact of assuming identical oscillators. We added a uniform random variable $r \in [-B, B]$ to the native frequency ω for each oscillator, and we found the chimera state persisted, as long as B was not too large—less than about 4% of Δ (the frequency difference between the locked oscillators' Ω and the mean natural frequency ω). This estimate should be conservative when compared with

a presumably more realistic Gaussian random distribution of ω_i.

There are several possibilities for experimental systems where the distinctive effects of nonlocal coupling, including the chimera state, might be observed. Laser arrays seem to be good candidates. In some cases, such as semiconductor arrays with evanescent coupling [Winful & Wang, 1988; Li & Erneux, 1992], they are governed by equations similar to (7.1), though these are usually approximated as nearest-neighbor. Likewise, phase equations of this form arise in the description of coupled electronic phase-locked loops, and superconducting arrays of Josephson junctions [Swift *et al.*, 1992; Wiesenfeld *et al.*, 1998]. Finally, an idealized model of biochemical oscillators, coupled by a diffusible substance that they all produce, can give rise to an effectively nonlocal coupling and chimera states; indeed, this was the motivating example that led Kuramoto and his colleagues to their discovery.

Whether or not the chimera state turns out to experimentally realizable, it is fascinating in its own right, as a strange new mechanism for pattern formation in spatially extended nonlinear systems. Its existence underscores how much still remains to be discovered, even in what would seem to be the simplest possible model of pattern formation: a one-dimensional collection of identical oscillators.

7.8   Appendix: Onset of Spatial Structure

We now show that the birth of spatial structure can be calculated non-perturbatively. We have already seen in Section 7.6.2 that when $\beta = 0$, the system has an exact state of spatially uniform drift with constant coherence $R(x) \equiv \sqrt{2\Delta - 1}$ and average phase $\Theta(x) \equiv 0$. For this special state, the modulation amplitude $a = 0$ and the mean level of the coherence $c = R = \sqrt{2\Delta - 1}$. At the bifurcation that creates spatial variation in the coherence, the real part of a becomes nonzero; at leading order in perturbation theory, this bifurcation takes place at $\delta = \frac{1}{8}$. Meanwhile, the imaginary part of a remains zero, which means that $\Theta(x) \equiv 0$ still holds.

To generalize this result to the non-perturbative case, we seek conditions for a second branch of solutions to bifurcate off the uniform drift state. Since $\Delta = (1 + c^2)/2$ for the drift state, we consider a slight perturbation

$$\Delta = (1 + c^2)/2 + \eta \ , \tag{7.36}$$

where η is a small deviation. Also, since $a = 0$ for the uniform drift state, we may take a itself as a small deviation. Plugging all this into the self-consistency equation (7.21) gives:

$$c = \left\langle \frac{(1 + c^2)/2 + \eta - [((1 + c^2)/2 + \eta)^2 - c^2 - 2ac\cos x - a^2\cos^2 x]^{\frac{1}{2}}}{c + a\cos x} \right\rangle \ . \tag{7.37}$$

Now expand in a two-variable Taylor series for small η and a, and integrate over x to obtain:

$$0 = \left[\frac{2c}{c^2 - 1}\eta + \mathcal{O}\left(\eta^2\right) \right]$$
$$+ \left[\frac{c(c^2 - 3)(c^2 + 1)}{2(1 - c^2)^3} + \frac{c(c^6 - 5c^4 + 19c^2 + 9)}{(1 - c^2)^5}\eta + \mathcal{O}\left(\eta^2\right) \right] a^2 + \mathcal{O}\left(a^4\right) \ . \tag{7.38}$$

Repeating the approach for the second self-consistency equation (7.22) gives:

$$0 = \left[\frac{2(c^2 - 1) + A(c^2 + 1)}{2(c^2 - 1)} + \frac{A(c^4 - 4c^2 - 1)}{(c^2 - 1)^3}\eta + \mathcal{O}\left(\eta^2\right) \right] a + \mathcal{O}\left(a^3\right) \ . \tag{7.39}$$

To locate where another branch of solutions bifurcates off the uniform drift solution, we inspect the linearization of the algebraic system above, given by the Jacobian matrix

$$
\begin{bmatrix}
\frac{2c}{(c^2-1)^2} & 0 \\
0 & \frac{2(c^2-1)+A(c^2+1)}{2(c^2-1)}
\end{bmatrix}
\tag{7.40}
$$

If the determinant of the Jacobian is nonzero, the implicit function theorem tells us that no other solutions exist nearby. Hence, the existence of a continuously bifurcating branch requires that the determinant vanish. Setting the determinant equal to zero yields $c = 0$ or $2(c^2 - 1) + A(c^2 + 1) = 0$. Plugging in the value of c about which we're linearizing, $c = \sqrt{2\Delta - 1}$, and solving for Δ finally gives the bifurcation condition

$$
\Delta_c = \frac{2}{A + 2} .
\tag{7.41}
$$

To compare this with our earlier result from first-order perturbation theory, we express the perturbative variable δ at this critical point by using its definition from (7.27) above and the property in (7.25). Since $\Delta - c = \delta\epsilon^2 = \delta A^2$ (ignoring higher order terms), we have $\delta = \frac{\Delta - c}{A^2}$. So

$$
\begin{aligned}
\delta_c &= \frac{\Delta_c - c}{A^2} \\
&= \frac{1}{A^2}\left(\frac{2}{A+2} - \sqrt{2\Delta_c - 1}\right) \\
&= \frac{1}{A^2}\left(\frac{2}{A+2} - \sqrt{\frac{2-A}{2+A}}\right) \\
&= \frac{1}{8} - \frac{1}{16}A + \frac{5}{128}A^2 - \frac{5}{256}A^3 + \mathcal{O}\left(A^4\right) ,
\end{aligned}
\tag{7.42}
$$

which agrees with our perturbative prediction that $\delta_c = \frac{1}{8}$ in the limit that $A \to 0$.

7.9 Appendix: Birth of the Chimera State

When $\beta = 0$, it is possible to calculate the chimera state exactly, at the moment of its birth from a spatially modulated drift state. Recall that all states of pure drift satisfy $\Theta(x) \equiv 0$, and equivalently, that a has zero imaginary part. Hence we can seek solutions of the algebraic self-consistency equations with real values of a and c, for $\beta = 0$. At the onset of the chimera, the first locked oscillators are born. As suggested by Fig. 7.6, this occurs when the graph of $R(x)$ intersects the horizontal line $R = \Delta$ tangentially.

Therefore the bifurcation condition is $\Delta = R_{max} = c + a$. Plugging this into (7.15) and (7.16), and using $\Theta(x) \equiv 0$ and $\beta = 0$, we find that the self-consistency equations become

$$c = \left\langle \frac{c + a - \sqrt{(c+a)^2 - (c + a \cos x)^2}}{c + a \cos x} \right\rangle \tag{7.43}$$

and

$$a = A \left\langle \frac{c + a - \sqrt{(c+a)^2 - (c + a \cos x)^2}}{c + a \cos x} \cos x \right\rangle . \tag{7.44}$$

Note that both of these expressions can be rewritten solely in terms of the ratio a/c, which suggests a neat way to solve them parametrically.

Set $s = a/c$ and substitute into (7.43) above, which becomes

$$
\begin{aligned}
c &= \left\langle \frac{1 + s - \sqrt{(1+s)^2 - (1 + s \cos x)^2}}{1 + s \cos x} \right\rangle \\
&= f_1(s) .
\end{aligned}
\tag{7.45}
$$

So we can also write $a = sc = s f_1(s)$.

Similarly, the a equation (7.16) becomes:

$$
\begin{aligned}
a &= A \langle h \cos x \rangle \\
&= A \left\langle \frac{1 + s - \sqrt{(1 + s)^2 - (1 + s \cos x)^2}}{1 + s \cos x} \cos x \right\rangle \\
&= A f_2(s) \; .
\end{aligned}
\tag{7.46}
$$

All other quantities of interest can also be expressed in terms of s. For instance, we can now substitute $a = sc = s f_1(s)$ into (7.46) and solve for $A(s) = a/f_2(s) = s f_1(s)/f_2(s)$. Likewise, $\Delta = c + a = (1 + s)f_1(s)$. In summary, the incipient chimera state can be written exactly in parametric form, as follows:

$$
\begin{aligned}
c &= f_1(s) \\
a &= s f_1(s) \\
A &= s \frac{f_1(s)}{f_2(s)} \\
\Delta &= (1 + s)f_1(s) \; .
\end{aligned}
\tag{7.47}
$$

Since A is a control parameter of the original equations (the only free one after β has been chosen to be zero), it is desirable to reparametrize this solution in term of A. To do that, we invert $A(s)$ in (7.47) to obtain the following series expansion for $s(A)$,

$$
s \sim \frac{16}{9\pi^2}A^2 - \frac{16}{27}\left(\frac{3\pi^2 - 32}{27\pi^4}\right)A^3 + \mathcal{O}\left(A^4\right) \; ,
$$

and use that to rewrite the newborn chimera in terms of A:

$$
\begin{aligned}
c &\sim 1 - \frac{16}{3\pi^2}A + \frac{8}{9}\left(\frac{5\pi^2 - 32}{\pi^4}\right)A^2 + \mathcal{O}\left(A^3\right) \; , \\
a &\sim \frac{16}{9\pi^2}A^2 - \frac{16}{27}\left(\frac{3\pi^2 - 16}{\pi^4}\right)A^3 + \mathcal{O}\left(A^4\right) \; , \\
\Delta &\sim 1 - \frac{16}{3\pi^2}A + \frac{8}{9}\left(\frac{7\pi^2 - 32}{\pi^4}\right)A^2 + \mathcal{O}\left(A^3\right) \; .
\end{aligned}
$$

Notice that this has exactly the form of the ansatz we postulated in (7.24), based on numerical experiments. As expected, it satisfies $\Delta_1 = c_1$ as in (7.25) and gives $\Delta_2 - c_2 = 16/(9\pi^2)$.

BIBLIOGRAPHY

[1] D. M. Abrams and S. H. Strogatz. Chimera states for coupled oscillators. *Phys. Rev. Lett.*, 93(17):174102, 2004.

[2] D. M. Abrams and S. H. Strogatz. Chimera states in a ring of nonlocally coupled oscillators. *Int. J. Bif. Chaos*, 16(1):21–37, 2006.

[3] H. Bachmann and W. Ammann. *Vibrations in Structures Induced by Man and Machines*. IABSE, Zurich, 1987.

[4] D. Battogtokh and Y. Kuramoto. Turbulence of nonlocally coupled oscillators in the benjamin-feir stable regime. *Phys. Rev. E*, 61(3):3227–3229, MAR 2000.

[5] A. Belli, P. Bui, A. Berger, A. Geyssant, and J. R. Lacour. A treadmill ergometer for three-dimensional ground reaction forces. *Journal of Biomechanics*, 34(1):105–112, JAN 2001.

[6] P. Dallard, A. J. Fitzpatrick, A. Flint, S. Le Bourva, A. Low, R. M. R. Smith, and M. Willford. The London Millennium footbridge. *The Structural Engineer*, 79(22):17–33, NOV 2001.

[7] P. Dallard, A. J. Fitzpatrick, A. Flint, A. Low, R. M. R. Smith, M. Willford, and M. Roche. London Millennium Bridge: Pedestrian-induced lateral vibration. *Journal of Bridge Engineering*, 6(6):412–417, NOV/DEC 2001.

[8] B. Ermentrout. An adaptive model for synchrony in the firefly pteroptyx-malaccae. *Journal of Mathematical Biology*, 29(6):571–585, JUN 1991.

[9] G. B. Ermentrout and J. Rinzel. Beyond a pacemaker's entrainment limit: Phase walk-through. *American Journal of Physiology: Regulatory Integrative Comp Physiol*, 246(1):102–106, JAN 1984.

[10] A. J. Fitzpatrick, P. Dallard, S. Le Bourva, A. Low, R. M. R. Smith, and M. Willford. Linking London: The Millennium Bridge. *Royal Academy of Engineering*, pages 1–28, JUN 2001.

[11] Y. Fujino, B. M. Pacheco, S. Nakamura, and P. Warnitchai. Synchronization of human walking observed during lateral vibration of a congested pedestrian bridge. *Earthquake Engineering and Structural Dynamics*, 22:741–758, 1993.

[12] I. S. Gradshteyn and I. M. Ryzhik. *Tables of Integrals, Series, and Products, 6th Edition*. Academic Press, San Diego, 2000.

[13] H. Haken. *Synergetics: Introduction and Advanced Topics*. Springer, Berlin, 2004.

[14] Y. Kuramoto. *Chemical Oscillations, Waves, and Turbulence*. Springer, Berlin, 1984.

[15] Y. Matsumoto, T. Nishioka, H. Shiojiri, and K. Matsuzaki. Dynamic design of footbridges. *IABSE Proceedings*, P-17/78, AUG 1978.

[16] A. McRobie, G. Morgenthal, J. Lasenby, and M. Ringer. Section model tests on human–structure lock-in. *Bridge Engineering*, 156(2):71–79, JUN 2003.

[17] R. E. Mirollo and S. H. Storgatz. Synchronization of pulse-coupled biological oscillators. *SIAM Journal of Applied Math*, 50(6):1645–1662, DEC 1990.

[18] S. Nakamura. Model for lateral excitation of footbridges by synchronous walking. *Journal of Structural Engineering*, 130:32–37, JAN 2004.

[19] D. E. Newland. Pedestrian excitation of bridges—recent results. *Proceedings of the Tenth International Congress on Sound and Vibration*, pages 1–15, JUL 2003.

[20] T. M. Roberts. Synchronised pedestrian excitation of footbridges. *Bridge Engineering*, 156(BE4):155–160, DEC 2003.

[21] S. H. Strogatz. *Nonlinear Dynamics and Chaos: with Applications to Physics, Biology, Chemistry, and Engineering*. Perseus Books LLC, New York, 1994.

[22] S. H. Strogatz. From Kuramoto to Crawford: Exploring the onset of synchronization in populations of coupled oscillators. *Physica D*, 143(1–4):1–20, SEP 2000.

[23] S. H. Strogatz, D. M. Abrams, F. A. McRobie, B. Eckhardt, and E. Ott. Crowd synchrony on the Millennium Bridge. *Nature*, 438(7064):43, 2005.

[24] D. Sudjic. *Blade of Light: The Story of London's Millennium Bridge*. Penguin Books Ltd, London, 2001.